Insights into the Selective Catalytic Reduction of NO_x from Quantum Chemical Calculations and Theoretical X-ray Spectroscopy

Von der Fakultät für Lebenswissenschaften

der Technischen Universität Carolo-Wilhelmina zu Braunschweig

zur Erlangung des Grades

eines Doktors der Naturwissenschaften (Dr.rer.nat.)

genehmigte

D i s s e r t a t i o n

von Julian Rudolph
aus Dannenberg / Elbe

1. Referent: Prof. Dr. Christoph R. Jacob
2. Referent: Prof. Dr. Peter Jomo Walla
eingereicht am: 29.04.2019
mündliche Prüfung (Disputation) am: 12.07.2019
Druckjahr 2019

Vorveröffentlichungen der Dissertation

Teilergebnisse aus dieser Arbeit wurden mit Genehmigung der Fakultät für Lebenswissenschaften, vertreten durch den Mentor der Arbeit, in folgenden Beiträgen vorab veröffentlicht.

Publikationen

- Günter, T., Carvalho, H. W. P., Doronkin, D. E., Sheppard, T., Glatzel, P., Atkins, A. J., **Rudolph, J.**, Jacob, Ch. R., Casapu, M., and Grunwaldt, J.-D., "Structural snapshots of the SCR reaction mechanism on Cu-SSZ-13", *Chem. Commun. 51*, pp. 9227-9230 (2015).
- Oung, S. W., **Rudolph, J.**, and Jacob, Ch. R., "Uncertainty quantification in theoretical spectroscopy: The structural sensitivity of X-ray emission spectra", *Int. J. Quantum Chem. 118*, e25458 (2018).
- **Rudolph, J.**, and Jacob, Ch. R., "Revisiting the Dependence of Cu K-Edge X-ray Absorption Spectra on Oxidation State and Coordination Environment", *Inorg. Chem. 57*, pp. 10591-10607 (2018).
- **Rudolph, J.**, and Jacob, Ch. R., "Computational insights into the mechanism of the selective catalytic reduction of NO_x: Fe- versus Cu-exchanged zeolite catalysts", *ACS Omega 4*, pp. 7987-7993 (2019).

Tagungsbeiträge

- **Rudolph, J.**, "Mechanistic insights into the selective catalytic reduction of NO from X-ray spectroscopy", *IXth Workshop on Modern Methods in Quantum Chemistry* (2016), Mariapfarr, Österreich.
- **Rudolph, J.**, "Selective catalytic reduction of NO_x from X-ray spectroscopy and density-functional theory", *7. Braunschweiger Jungchemiker Tagung* (2016), Braunschweig.

Posterbeiträge

- **Rudolph, J.**, Atkins, A. J. and Jacob, Ch. R., "Quantum-Chemical Methods for the Calculation of Metal K-edge X-Ray Absorption Spectra: A Systematic Benchmark Study", *The 16th International Conference on X-ray Absorption Fine Structure* (2015), Karlsruhe.
- **Rudolph, J.**, Brauer, C.-A. and Jacob, Ch. R., "Mechanistic insights into to selective catalytic reduction of nitrogen oxides", *52nd Symposium on Theoretical Chemistry* (2016), Bochum.

- **Rudolph, J.**, Brauer, C.-A. and Jacob, Ch. R., "Computational study of the reaction mechanism of the SCR of NO_x using copper(II)-zeolite catalyst SSZ-13", *11th Triennial Congress of the World Association of Theoretical and Computational Chemists* (2017), München.

- **Rudolph, J.** and Jacob, Ch. R., "Quantenchemische Berechnungen zur Aufklärung des Mechanismus der selektiven katalytischen Reduktion von NO_x", *3. NFF-Doktorandentag* (2017), Braunschweig.

Contents

Chapter 1

Introduction

1.1 Introduction to SCR reaction

The goal of this thesis is to elucidate a consistent reaction mechanism of the selective catalytic reduction (SCR) over copper- and iron-exchanged zeolite catalysts. This reaction type can be used, e.g., for the exhaust gas aftertreatment in Diesel engines. The molecular processes at the transition metal catalysts are still not understood in detail.[1–3] Only when the key steps are unraveled, it is possible to improve these catalytic systems in a targeted way. To reach the stated goal, several computational spectroscopic and thermodynamic studies were performed in this thesis.

In general, there are two classic engines using fossil fuel, the Otto and the Diesel engine. In the case of the Otto engine, to reach the emission limits for carbon monoxide (CO), hydrocarbons (C_mH_n), and nitrogen oxides (NO_x), a three-way-catalyst is used to convert these three undesirable molecule classes in the exhaust gas. In contrast, the Diesel engine works with an air excess and this type of catalyst becomes impractical for the conversion of NO_x. By additionally attaching an SCR catalyst into the exhaust gas aftertreatment system, this problem can be addressed. Here, an urea solution is injected into the hot exhaust gas flow. Subsequently, ammonia is formed, which can react with nitrogen monoxide to form nitrogen and water catalyzed by the transition metal SCR zeolite catalyst. This process is called ammonia selective catalytic reduction (NH_3-SCR).[3–6]

This technique is already well-known and was developed in the 1970s in Japan, but with the restriction to stationary usage (e.g. power and waste incineration plants). The used catalysts were based on a titanium, vanadium, and tungsten oxide compound [V_2O_5-WO_3/TiO_2]. The reaction mechanism for the stationary approach was more or less fully elucidated by Arnarson et al.[7] in 2017. They were able to use density-functional theory (DFT) calculations to develop

a plausible way for the SCR reaction over these oxide catalysts. They considered the complete redox cycle consisting of the metal reduction and the following metal reoxidation.

The first non-stationary application for a Diesel vehicle was suggested in 1990.[8] After several years of development and testing, the first vehicle using an SCR technique was introduced in 2002. The major problems of vanadium catalysts in Diesel vehicles are the high activity for oxidation of SO_2 to SO_3 and the rapid decrease in activity and selectivity at high temperatures. Furthermore, an other problem is the high toxicity of vanadium species, which begin to volatilize at high temperatures.[6,9–11] Compared to the stationary approach, nowadays iron and copper zeolite catalysts are used, but the possible reaction pathways have not been clarified in detail. There were several approaches to gain insight into the mechanism, both experimentally and computationally, but a detailed understanding of the full reaction mechanism is still lacking.

Experimental X-ray spectroscopy combined with density-functional theory (DFT) is one of the most widespread methods in literature to elucidate the SCR mechanism. Spectroscopic experiments are often combined with quantum-chemical calculations in order to connect them to specific features of the underlying molecular structure. Only few spectroscopic techniques, e.g. X-ray absorption fine structure spectroscopy (EXAFS), provide direct access to structural parameters. In contrast, many important spectroscopic techniques such as vibrational spectroscopy or X-ray absorption and emission spectroscopy, only provide indirect access to structural information.

In general, X-ray spectroscopy can be explained very easily. Electrons from core orbitals can be excited to higher unoccupied orbitals or continuum states by incident high energy X-ray photons. This process is called X-ray absorption spectroscopy (XAS). The reverse part, containing the refilling of the incurred core holes, is called X-ray emission spectroscopy (XES). The energies of core electrons, which were excited during the XAS process, are unique to an element. This is one of the major benefits of XAS. Overall, X-ray absorption spectroscopy provides a valuable tool for investigating the geometric and electronic structure of catalytic transition metal centers.[12–14] On the other hand, valence-to-core (VtC) X-ray emission spectroscopy, can be used to obtain partial structural information, in particular in the vicinity of transition metal centers. VtC-XES makes it possible to identify which ligands are coordinated to a transition metal center, for instance in molecular transition metal complexes,[15–18] for metal clusters in enzymes[19–21] and also for catalytic metal centers in SCR zeolite complexes.[22,23]

Such a combination of experiment and theory is presented in the collaboration of our group with the group of Grunwaldt at Karlsruhe Institute of Technology (KIT). Here, Boubnov et al.[22] were able to confirm several reaction steps speculated in literature and propose a new reaction scheme for the SCR reaction based on iron-exchanged zeolite catalysts. They combined complementary XAS and XES techniques under realistic operating conditions with DFT calculations. This approach were repeated with a copper-exchanged zeolite catalyst and afterwards compared with

the previous results.[23] It was possible to obtain important new insights into the structure of copper and its interaction with NH_3 and NO during the SCR reaction. A significant difference in the intermediate species during SCR over copper- and iron-exchanged catalysts was found. The third and lowest-energy Kβ" peak, which was assigned to a positively polarized/triple coordinated oxygen atom at the iron center including a coordinated NO in Ref. [22], could not be observed for copper catalysts during SCR reaction. The DFT calculations confirmed that this peak should also appear in spectra of Cu-exchanged zeolite complexes if the underlying mechanism proceeds via the same mechanistic intermediates. This led to the assumption that the copper mechanism must proceed via other mechanistic steps.[23] Furthermore, despite additional DFT calculations, no further information could be obtained from the XAS and XES spectra.

At this point, three questions arose:

1. How can computational X-ray spectroscopic methods be applied/improved with respect to the elucidation of the SCR mechanism?
2. Why are three peaks observed in the Kβ"-region of XES spectra during iron SCR reaction and not in the case of copper?
3. In general, how does the mechanism of the SCR reaction proceeds?

1.2 The thesis

This thesis is divided into two parts. In the first part, Chap. 2–4, the theoretical fundamentals are introduced. More specifically, the chronological development of the SCR reaction is presented in Chap. 2. Furthermore, this chapter presents the considered SCR catalysts and the previous mechanistic results are discussed in detail. In Chap. 3 the basics of X-ray absorption and emission spectroscopy are explained, and an introduction to density-functional theory is given in Chap. 4, with a special focus on calculating XAS and XES spectra. In the second part, Chap. 5–7, three different applications of using computational tools on transition metal complexes in general and on the SCR mechanism in particular are presented.

Motivated by the previous results of our group, the work on the field of the SCR reaction was further deepened. The first application example, which includes computational XAS studies on several copper complexes, is presented Chap. 5. During the SCR process, iron and copper catalysts typically undergo one-electron oxidation and reduction, and the catalytic properties thus crucially depend on the Fe(II)/Fe(III) and Cu(I)/Cu(II) redox properties. These, in turn, are tuned by the local coordination environment of the metal center. In particular, K-edge X-ray absorption spectroscopy probes transitions from the metal $1s$ core orbital to unoccupied electronic states that depend both on the oxidation state of the metal center and the local coordination environment. In Chap. 5 of the thesis it is shown that computational X-ray absorption

spectroscopy at the Cu K-edge has the ability to reproduce experimental results. Even more, it is possible to explain experimentally observed features in detail and with theoretical molecular orbital (MO) analysis, occurring peaks can be assigned to transitions into specific unoccupied metal and ligand orbitals.

In Chap. 6, the ability of computational VtC-XES spectroscopy to unravel further structural details, such as coordination number or bond angles, as well as insights into the electronic structure has been explored as an second application example. Here, a test set of three closed-shell iron-carbonyl complexes is examined with the focus on structural sensitivity. For that, several bond lengths and angles were elongated to identify which ligand is responsible for which obtained peak.

Finally, Chap. 7 combines computational thermodynamic and X-ray spectroscopic studies to propose a consistent reaction mechanism for the SCR reaction over both Fe- and Cu-exchanged zeolite catalysts to pick up the initial question of this thesis. With this proposal it is possible to describe the significant differences during the SCR reaction and to explain the differences observed in the XES spectra of Ref. [22] and [23]. For computational feasibility, a small catalytic model system is developed, which was previously tested to guarantee reliable results. Afterwards several possible reaction pathways are examined for copper and iron catalysts.

Overall, in Chap. 5 and 6 it is shown that the application of theoretical X-ray spectroscopy on transition metal complex provides important features beyond experimental accessible results. Furthermore, in Chap. 7 a solid basis has been developed to explore the SCR mechanism in more detail. For the first time, considering multiple possible intermediate reaction pathways, a consistent reaction scheme over both iron and copper zeolite catalysts has been developed.

Chapter 2

Selective catalytic reduction (SCR)

In general, there are two classic types of passenger vehicle engines using fossil fuel, the Otto and the Diesel engine. The emissions limits for carbon monoxide and nitrogen monoxide produced by combustion engines have become very strict over the years. To address this problem, the Otto engine uses the well-known three-way-catalyst to covert the three undesirable compounds carbon monoxide, nitrogen monoxide, and hydrocarbons to carbon dioxide, water, and gaseous nitrogen. In contrast, the Diesel engine works with an air excess and this technique becomes impractical. But by implementing a SCR catalyst into the exhaust gas aftertreatment system, this problem can be solved. A detailed overview of the SCR reaction in general, known transition metal SCR catalysts and suggested reaction mechanisms will be given in the following sections.

2.1 SCR process and implementation

A major source of air pollution are nitrogen oxides, which are produced by combusting fossil fuels.[24,25] Thermal NO_x, which is produced in combustion processes in engines, accounts for the largest share.[6] During this process, nitrogen from the atmosphere will be oxidized with oxygen at high temperatures, see 2.1 and 2.2.[24,26,27]

$$N_2 + O_2 \rightarrow 2NO \tag{2.1}$$

$$NO + \frac{1}{2}O_2 \rightarrow NO_2 \tag{2.2}$$

In general, the exhaust gas flow contains three unwanted components, which have to be removed, carbon monoxide (CO), hydrocarbons (C_mH_n), and nitrogen oxides ($NO_x \rightarrow$ NO and NO_2).[4] The emission limits for these three compounds decreased very strictly over the last years, most seriously for nitrogen oxides (see Fig. 2.1 for CO and NO_x emission limits).

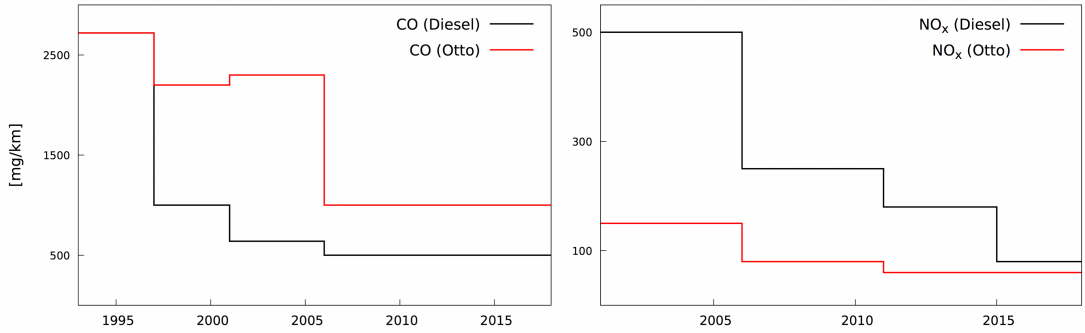

Figure 2.1: Emission limits for carbon monoxide (EU regulation, EURO 1–6, 1993–2018, left panel). Emission limits for nitrogen oxides (EU regulation, EURO 3–6, 2001–2018, right panel). Before 2001, there were no NO_x limits. The emission limits are presented as black (Diesel engine) and red lines (Otto engine).

In vehicles powered by an Otto engine, these limits can be reached by implementing a three-way-catalyst,[4,5] which contains a transition metal in its catalytic center. It is possible to remove all components with high efficiency, especially the NO_x conversion is over 99 %.[7] The three reaction equations for such an exhaust gas aftertreatment are shown in (2.3)-(2.5).

$$2\ CO + O_2 \rightarrow 2\ CO_2 \tag{2.3}$$

$$C_mH_n + \left(m + \frac{n}{4}\right)\ O_2 \rightarrow m\ CO_2 + \frac{n}{2}\ H_2O \tag{2.4}$$

$$2\ NO + 2\ CO \rightarrow N_2 + 2\ CO_2 \tag{2.5}$$

The operating system of a Diesel engine is different compared to the Otto engine, it produces lean exhaust gases.[6] Which means, a lot of oxygen is in the system and with this oxygen nearly the complete amount of CO will be converted (2.3). To remove nitrogen oxides a certain amount of CO is needed (2.5), but it is not available anymore because of reaction (2.3), so this whole three-way-catalytic approach is impractical for Diesel engines. To address this problem, the SCR technique can be used.[9,27–29]

The first SCR technique for exhaust gas aftertreatment has been even developed in the 1970s in Japan, but this application was only available for stationary plants.[27] For several decades such a method has been applied in e.g. power plants, waste incineration plants, and generally stationary combustion engines.[30–32] The first application for a Diesel vehicle was suggested by Held et al.[8] in 1990. A schematic representation of such an implementation is shown in Fig. 2.2.

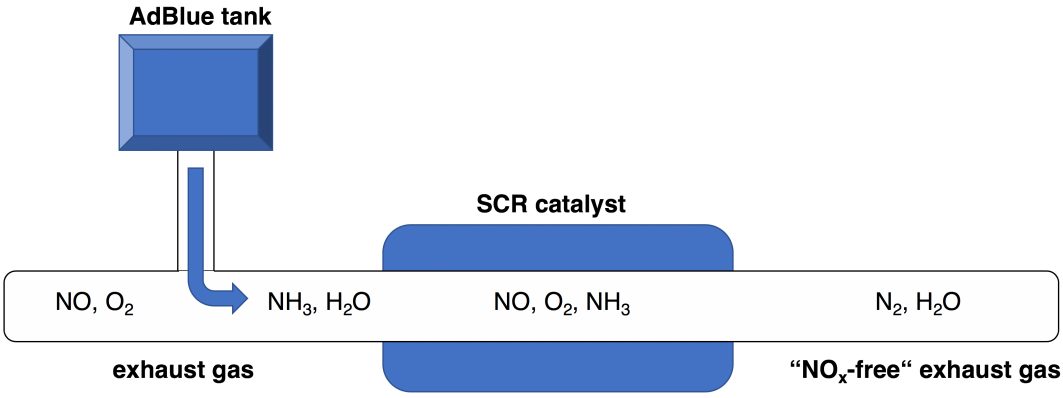

Figure 2.2: Schematic representation of a SCR application in a Diesel engine. Here, ammonia is formed in the hot exhaust gas flow and coordinates afterwards at the SCR catalyst to reduce nitrogen oxides to nitrogen (N_2) and water.

Over the last ten to fifteen years, the selective catalytic reduction of nitrogen oxides became more and more interesting for the automotive industry. The conversion efficiency is high at low costs and the strict emission limits can be reached.[33] One problem is, ammonia must be available in the exhaust gas flow and it can not be added purely. Therefore, a second tank is needed (see Fig. 2.2), which contains a aqueous urea (CH_4N_2O) solution called AdBlue. This solution will be directed into the exhaust gas flow over an injection system.[34–36] The high temperature will decompose urea to ammonia and isocyanic acid. This process is called thermolysis[37] (Eq. 2.6).

$$(NH_2)_2CO \rightarrow NH_3 + HNCO \quad \text{(thermolysis)} \tag{2.6}$$

$$HNCO + H_2O \rightarrow NH_3 + CO_2 \quad \text{(hydrolysis)} \tag{2.7}$$

In a subsequent reaction, the hydrolysis[37](Eq. 2.7), water will react with isocyanic acid to additional ammonia. In general, the amount of urea is about 2% with respect to used Diesel fuel. This amount must be controlled, a too low concentration of ammonia can reduce the reduction efficiency radically. An abundance of NH_3 can be handled by an additional catalyst, which oxidizes ammonia to nitrogen.[38]

Finally, the equations for standard (with nitrogen monoxide) and fast (with nitrogen dioxide) SCR are shown in (2.8)-(2.9).

$$4\ NH_3 + 4\ NO + O_2 \rightarrow 4\ N_2 + 6\ H_2O \text{ (standard SCR)} \tag{2.8}$$

$$2\ NH_3 + NO + NO_2 \rightarrow 2\ N_2 + 3\ H_2O \text{ (fast SCR)} \tag{2.9}$$

This whole process is a redox reaction which can be subdivided into two half-cycles, the reduction half-cycle and the subsequent oxidation half-cycle. In the fast SCR, nitrogen dioxide acts as an oxidant, transforming the transition metal from the oxidation state of X to X+1. The most debated issue for the reduction part is, whether ammonia or nitrogen monoxide reacts first with the catalyst and how the underlying mechanism proceeds. During the oxidation part, both the standard and the fast SCR reaction can take place.

Actually, the reactions discussed above have to be called NH_3-SCR, because the abbreviation "SCR" is also used for the reduction process of NO_x with hydrogen (H_2-SCR)[39] or with hydrocarbons (HC-SCR).[40] However, the use of the term "SCR" can be misleading in these cases, as these reaction types are not "selective" because a high excess of reducing agent is needed.[6]

2.2 Transition metal SCR catalysts

Early SCR catalysts for the stationary approach were based on transition metal oxides complexes.[6,31] These catalysts are mainly titanium dioxide (TiO_2) supported divanadium pentoxide (V_2O_5), promoted with tungsten trioxide (WO_3) [V_2O_5-WO_3/TiO_2].[7,41–46] For the non-stationary approach, these vanadium catalysts are also used since 2005. The major problem of this catalyst type in Diesel vehicles is the high activity for oxidation of SO_2 to SO_3, and the rapid decrease in activity and selectivity at high temperatures. Furthermore, an other problem is the high toxicity of vanadium species, which begin to volatilize at high temperatures.[6,9–11]

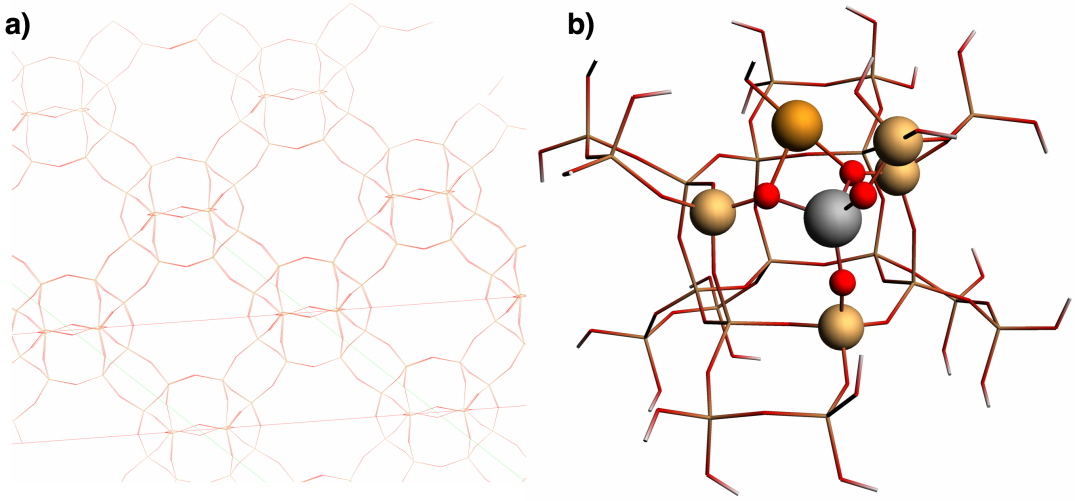

Figure 2.3: (a) Framework of SSZ-13 zeolite. (b) Molecular structure of an optimized copper +II zeolite model complex with Cu (orange), O (red), N (blue), Al (grey), Si (light brown) and H (white). The atoms taken for the small model complexes in Chap. 7 are visualized as "spheres".

Nowadays, transition metal zeolite catalysts are widely used for this type of reactions.[9,27–29] The

transition metals are in general Cu(II) or Fe(III). A copper catalyst model structure is shown in Fig. 2.3b. These zeolites are microporous aluminosilicates with tetrahedral SiO_4 primary unit forming channels and cages (see Fig. 2.3a). At certain locations, silicon atoms are replaced by aluminium atoms. The resulting negative charge on the aluminium is usually compensated by a positively charged sodium cation. These counter ions are located in 'pore holes' and can be selectively replaced by the desired transition metals.[36,47] The most well-known catalyst containing iron as the central atom is the much-studied Fe-ZSM-5 catalyst.[22,48,49] A newer zeolite catalyst in this area is Fe-SSZ-13, which is characterized by its high temperature activity and stability.[50,51] In general, the SSZ-13 and SAPO-34 zeolite compounds are small-pore chabazite (CHA) zeolites, which have a better SCR performance then medium- or large-pore zeolites like ZSM-5.[36] The most important and most studied SCR catalysts for the non-stationary approach have copper as the central atom. These Cu zeolites are known as Cu-SSZ-13[23,52–57] and Cu-SAPO-34.[57–59]

2.3 SCR reaction mechanism

The reduction and oxidation half-cycles are shown schematically in Fig. 2.4. For vanadium catalysts, see Refs. [7, 41–46], many attempts have been made over the years to understand the complex reaction mechanism. Finally in 2017, Arnarson et al. [7] were able to use density-functional theory calculations to develop a plausible reaction mechanism for the SCR reaction based on vanadium catalysts. They considered the complete redox cycle (Fig. 2.4) consisting of the reduction of vanadium and the following oxidation.

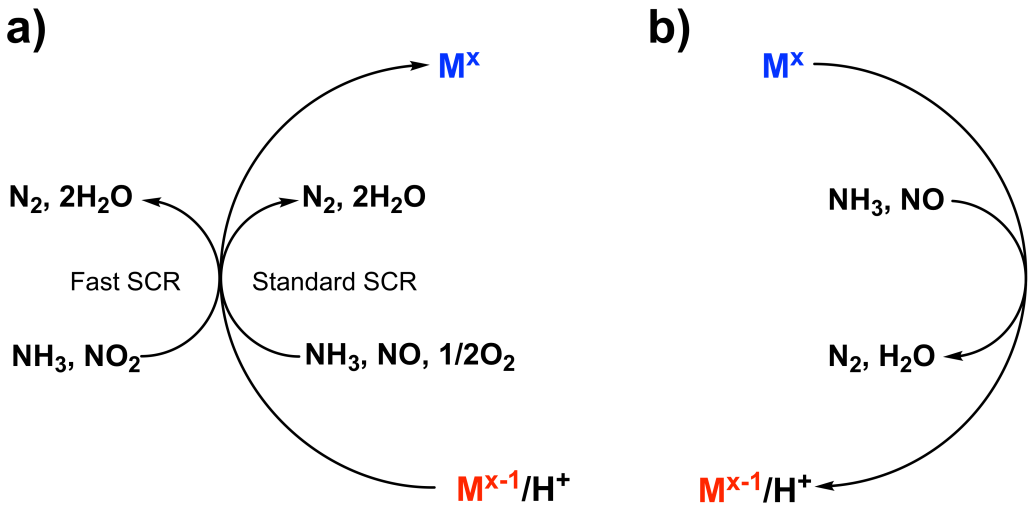

Figure 2.4: Schematic SCR redox cycle. (a) SCR oxidation half-cycle including standard and fast SCR. (b) SCR reduction half-cycle.

Compared to the vanadium catalyst, the possible reaction pathways for iron have not been clarified in detail so far. There were several approaches to gain insight into the mechanism,[22,60,61] but to the best of my knowledge, a detailed reaction path has not been published. The same is true for the copper mechanism. In a number of previous publications[23,53,54,57–59] shortened mechanisms based on spectroscopic and computational studies are proposed for possible copper-catalyzed reaction paths. In contrast to the approach in this thesis, in the cited publications only one or two possible reaction pathways are considered. The suggested mechanisms will be discussed and compared in the following Sec. 2.3.1 and 2.3.2.

2.3.1 Reduction half-cycle

In this thesis, the interest is focussed on the reduction half-cycle. The key question is whether NH_3 or NO interacts first with the catalyst and in what form the reaction proceeds. Especially for this part, a step by step development of the mechanism is not given in literature. There were several suggestions for possible reaction paths, but the whole mechanism is not solved so far. For example, in Refs. [53, 54, 59] the proposed mechanism starts with the reaction of ammonia, followed by the reaction of nitrogen monoxide (see Fig. 2.5a). This leads to a NH_2NO ligand, bound via the NH_2-nitrogen.

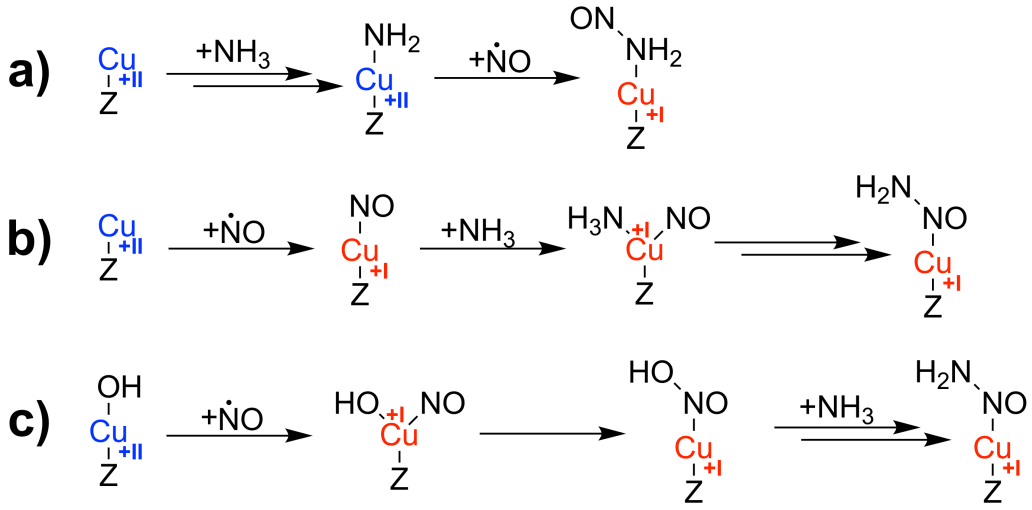

Figure 2.5: Schematic representation of three reaction pathways suggested by previous studies for the mechanism of the reduction half-cycle of the SCR reaction catalyzed by **Cu-exchanged zeolite catalysts**. (a) Proposal in Refs. [53, 54, 59]. (b) Proposal in Ref. [58]. (c) Proposal in Ref. [57].

In the proposals of Mao et al.[58] (Fig. 2.5b) and Janssens et al.[57] (Fig. 2.5c) the nitrogen monoxide reacts first and reduces the copper center. In Ref. [58], NH_2NO is also formed afterwards, but bound via the NO-nitrogen. The decomposition of this leaving group is shown in detail. In

the proposed mechanism in Ref. [57], the first step involves the formation of a HONO group, bound via the nitrogen of NO. Subsequently, ammonia reacts to form the equivalent leaving group NH_2NO, also bound via the NO-nitrogen.

Overall, the suggestions in these previous studies are contradictory and the reaction mechanism needs further investigation. To gain insights into the mechanism of SCR reaction, we developed new approaches based on density functional theory calculations and theoretical spectroscopy. The theoretical background will be given in the Chap. 4.

2.3.2 Oxidation half-cycle

For the oxidation half-cycle, Paolucci et al.[53,54] proposed reoxidation via NO and $\frac{1}{2}$ O_2 (standard SCR, Fig. 2.6a and b). In Ref. [54], nitrogen dioxide is formed from oxygen and nitrogen monoxide and afterwards oxidizes Cu(I) to Cu(II) to form an absorbed nitrite (Fig. 2.6a). During the reduction a hydrogen atom is shifted to the zeolite ring system and afterwards reacting with ammonia to an NH_4^+ species. This species forms an NH_4NO_2 complex with the nitrite ligand, which decomposes to nitrogen and water. This mechanism is equivalent to the one described in Ref. [53]. Here, ammonia is bound twice to the catalyst and two aluminum atoms are included in the zeolite ring, nevertheless the mechanistic steps remain unchanged. Also another suggestion is included in Ref. [53], which is shown in Fig. 2.6b. Starting from a catalyst with two ligands, hydroxyl and ammonia, and a zeolite ring system containing one aluminium, the mechanistic steps are similar but not equivalent. There is no hydrogen transfer between the catalyst and the zeolite cage, instead water will be released during the reduction. This results in a different oxidation mechanism, but the key step of forming an absorbed nitrite is also included here. Most likely, the suggested oxidation half-cycle of Paolucci et al. proceeds via the formation of dimeric Cu species.[53,62] The reaction path of Mao et al.[58] (Fig. 2.6c) is similar to the ones shown in Refs. [53, 54]. The reoxidation proceeds also via forming an absorbed nitrite from O_2 and NO, but bound over the nitrogen to the catalyst. The possibility of a direct reaction with NO_2 (fast-SCR) is mentioned, but not shown in detail. Another proposal in Ref. [59] shows the reoxidation for both standard and fast SCR via a HONO ligand, which interacts with the copper via its OH-oxygen (Fig. 2.6d). Janssens et al.[57] key step for both reoxidation pathways is the formation of a four-membered ring, in which nitrogen and copper are bridged by two oxygen atoms, comparable to [53, 54] (Fig. 2.6e). Overall, it can be seen that the oxidation half-cycle has already been investigated more or less in detail, but the results are contradictory.

In this thesis, the oxidation half-cycle will not be considered and these previous results were only shown for sake of completeness. But for the future, it would be worthwhile to consider all suggested reaction pathways together, using the same density-functional theory method to get comparability.

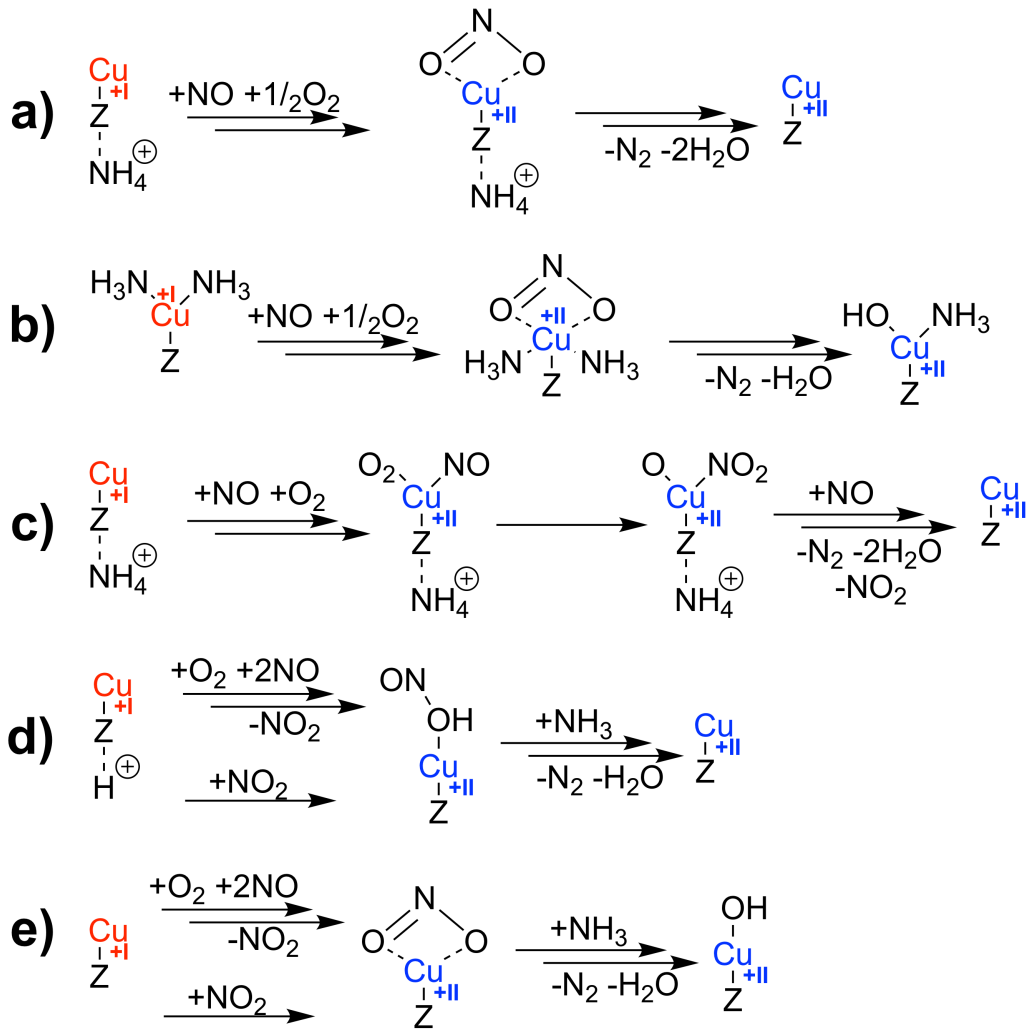

Figure 2.6: Schematic representation of five reaction pathways suggested by previous studies for the mechanism of the oxidation half-cycle of the SCR reaction catalyzed by **Cu-exchanged zeolite catalysts**. (a) Proposal in Refs. [53, 54]. (b) Proposal in Ref. [53]. (c) Proposal in Ref. [58]. (d) Proposal in Ref. [59]. (e) Proposal in Ref. [57].

Chapter 3

X-ray Spectroscopy

In general, spectroscopy is an essential tool for unraveling molecular structure. However, only few spectroscopic techniques, most importantly nuclear magnetic resonance (NMR) spectroscopy or X-ray absorption fine structure spectroscopy (EXAFS), provide direct access to structural parameters such as interatomic distances or coordination numbers and thus allow for the direct determination of molecular structures and/or a direct structural refinement. In contrast, many important spectroscopic techniques such as vibrational spectroscopy, UV/Vis spectroscopy, or X-ray absorption and emission spectroscopy, only provide indirect access to structural information. In this case, spectroscopic experiments are often combined with quantum-chemical calculations in order to connect them to specific features of the underlying molecular structure.[63]

For example, the analysis of calculated vibrational spectra can provide detailed insights into the connection between specific spectral features and the underlying molecular structure.[64–66] For X-ray spectroscopy, quantum-chemical calculations can provide an assignment of the peaks in X-ray absorption and emission spectra to occupied and unoccupied electronic states, and can connect those to the structure of the ligand environment in transition metal complexes (see, e.g., Refs. [16, 67–69]). An unique feature of X-ray spectroscopy is that transition metal centers can be selectively treated, while organic species in the system, which are not directly coordinated to metal center, will be neglected.

3.1 X-ray Absorption Spectroscopy (XAS)

X-ray absorption spectroscopy can be explained in a very simple way. Electrons from core orbitals (e.g. 1*s*- or 2*s*-orbital, see Fig. 3.1a and b) can be excited to unoccupied orbitals or continuum states by incident high energy X-ray photons. If an X-ray photon has a certain energy, it can knock out an electron out of a core orbital. At this energy, the absorption of the

X-ray radiation increases sharply, which is apparent in the measured spectrum. These energies of core electrons are unique to an element, which is one of the major benefits of XAS.[70] Depending on from which core electronic state an electron is excited, different edge nomenclatures are used.[71,72] For example, if an excitation from the 1s level occurs, this process is called K-edge X-ray absorption spectroscopy (see Fig. 3.1b). The L-edge can be divided into three different edges (L_1-L_3), containing excitations from 2s- (L_1) or 2p-orbitals (L_2, L_3). The presence of spin-orbit coupling leads to 2p L-edge splitting, describing transitions from the $2p_{1/2}$ and $2p_{3/2}$ orbitals, respectively.[73]

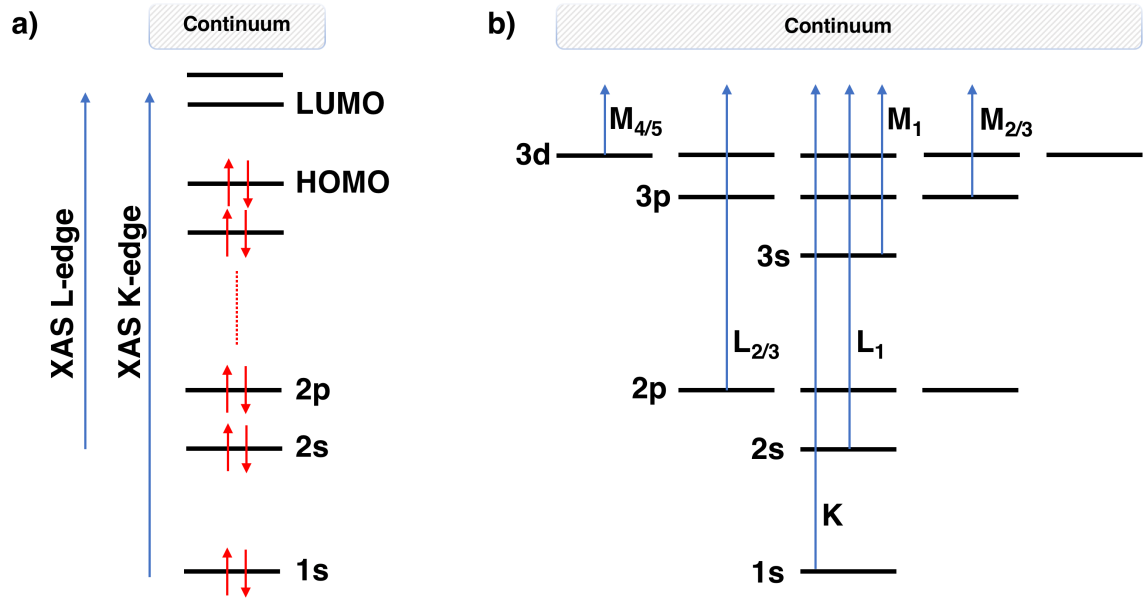

Figure 3.1: Diagrammatic representation of X-ray absorption edges. a) Core excitations from 1s- and 2s-orbital (K- and L-edge). b) Advanced picture of X-ray absorption edges including K-, L- and M-edges.

The interest in Fe- and Cu-based catalysts stems from the need to replace industrial processes requiring rare and expensive precious metals by sustainable alternatives based on earth-abundant base metals such as Fe and Cu (see, e.g., Refs. [74] and [75]). The SCR reaction a prominent example of a technical application.[62,76,77] As already mentioned, Fe and Cu catalysts undergo one-electron oxidation and reduction, and the catalytic properties thus crucially depend on the Fe(II)/Fe(III) and Cu(I)/Cu(II) redox properties. These, in turn, are tuned by the local coordination environment of the metal center.

X-ray absorption spectroscopy provides a valuable tool for investigating the geometric and electronic structure of catalytic transition metal centers.[12–14] In particular, K-edge X-ray absorption spectroscopy probes transitions from the metal 1s core orbital to unoccupied electronic states that depend both on the oxidation state of the metal center and the local coordination environ-

ment.[78,79] In the past years, high-energy resolution fluorescence detection XAS (HERFD-XAS) methods have been established[80–84] that remove the life-time broadening and thus reveal additional spectral features, in particular in the pre-edge region, which is due to transitions into chemically relevant low-lying unoccupied electronic states.[68,69] In combination with other spectroscopic methods as well as quantum-chemical calculations, XAS and HERFD-XAS have been successfully applied for investigating catalytic reaction mechanisms, e.g., of SCR catalysis with Fe- and Cu-exchanged zeolites.[23,85–88]

3.2 X-ray Emission Spectroscopy (XES)

X-ray emission spectroscopy can be considered as the "reverse" process to XAS, which records the X-ray spectrum emitted by the sample/molecule. Here, the core hole created during the absorption process is unstable and decays rapidly. In general, the 1s core hole can be refilled by electrons from all occupied orbitals. In Fig. 3.2a, the valence-to-core XES (VtC-XES) process is shown. By refilling the core hole with an electron from ligand ns or np valence orbital, the so-called Kβ'' or K$\beta_{2,5}$ emission lines would be obtained, respectively (Fig. 3.2b). An other Kβ line arises from the fluorescence that occurs when a 3p electron refills the core hole. This main line can split into Kβ' and K$\beta_{1,3}$, due to 3p-3d exchange interactions. The lowest energy edge is the Kα, which can be obtained after a 2p electron refills the core hole. The presence of spin-orbit coupling leads to a splitting into Kα_1 and Kα_2, as mentioned for XAS.[72,89]

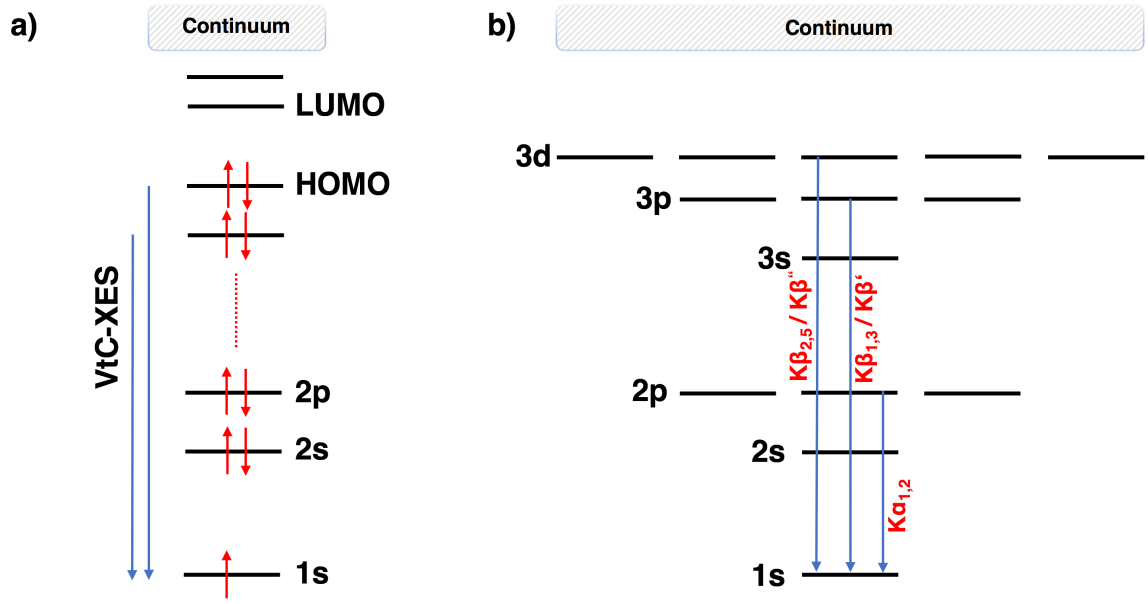

Figure 3.2: Diagrammatic representation of X-ray emission edges. a) valence-to-core transitions to 1s-orbital. b) Advanced picture of X-ray emission edges including Kβ- and Kα-edges.

In this thesis, the focus is on valence-to-core (VtC) X-ray emission spectroscopy.[84,90] In combination with quantum-chemical calculations, VtC-XES can be used to obtain partial structural information, in particular in the vicinity of transition metal centers. VtC-XES makes it possible to identify which ligands are coordinated to a transition metal center, for instance in molecular transition metal complexes,[15–18] for catalytic metal centers in zeolites,[22,23] and for metal clusters in enzymes.[19–21] The ability of VtC-XES spectroscopy to unravel further structural details, such as coordination number or bond angles, as well as insights into the electronic structure has also been explored.[16,18,91,92]

3.3 X-ray Spectroscopy for SCR Catalysis

Experimental and computational X-ray spectroscopy is an established tool to investigate catalytic processes. In many previous publications X-ray spectroscopic methods have been applied to gain insights into catalytic systems, see references in Sec. 3.1 and 3.2.

As already mentioned in the introduction, in our group, X-ray spectroscopic methods were applied to the SCR reaction in previous publications (Boubnov et al.[22] and Günter et al.[23]). In these two works, experimental and computational X-ray spectroscopic methods were combined to describe the molecular processes at the catalytic metal centers. The applied experimental methods were HERFD-XAS and VtC-XES at the iron[22] and copper[23] K-edges under NH_3-SCR operating conditions. The experimental group of Grunwaldt synthesized the iron- and copper-exchanged zeolite SCR catalysts (Fe-ZSM-5 and Cu-SSZ-13) and developed a microreactor cell, in which the gas mixture around the catalyst could be controlled. Here, five different gas components, He, O_2, H_2O, NO, and NH_3, were considered. By systematically changing the amount of these components, the aim was to investigate the influence on the XAS and XES spectra.

In the experimental X-ray absorption spectra, an intense pre-peak was observed, which can be assigned to the electron transition from an $1s$ core orbital to a singly unoccupied $3d$-orbital. Therefore, this transition is only possible for open-shell Fe and Cu compounds. In general, this pre-edge peak is an indicator for the Fe(II)/Fe(III) or Cu(I)/Cu(II) ratio. As expected, under SCR conditions (NH_3 + NO + ...) the open-shell metal center is reduced to a closed-shell electronic configuration in both iron and copper cases, which leads to a strong decrease of the pre-peak.

In addition, VtC-XES spectra were recorded under the same conditions. All spectra show an intense peak at lower energies. The addition of NH_3 results in a second peak in the XES spectra at higher energies. This feature is already known from literature and can be explained by the coordination of a nitrogen atom with a free electron lone-pair (e.g. NH_2) to the metal center. Furthermore, DFT calculations show a hypothetical third peak at lower energies attributed to

the coordination of a nitrogen species to the hydroxyl group for both iron and copper catalysts. In the experimental results such a peak is only obtained for iron catalysts, which leads to the conclusion that the mechanism for copper cannot pass over such a Cu-O^+H-N fragment as suggested for iron.

In summary, the X-ray absorption spectroscopy results demonstrate that the pre-peak is directly related to the Fe(II)/Fe(III) or Cu(I)/Cu(II) ratio. On the other hand, the absence of the third peak in the VtC-XES spectra at lower energies for the copper catalyst suggests a different mechanism as proposed for the iron SCR reaction.

The computational part of publication [23] is based on this section of this thesis.

Chapter 4

Density Functional Theory Calculations

The calculations performed and presented in this work use the density-functional theory (DFT) approach, which will be shortly explained in Sec. 4.1. The basic idea of this method is to describe molecular systems with the electron density instead of wave function. The two different quantum chemical methods TD-DFT and ΔDFT used for calculating the X-ray absorption and emission spectroscopy spectra, respectively, will also be introduced in the following Sec. 4.2 and 4.3.

4.1 Density-Functional Theory (DFT)

By replacing the many-body electronic wave function with the electron density, the DFT approach attempts to circumvent both, the inaccuracy of Hartree-Fock (HF) and the high computational requirements of post-HF methods such as configuration interaction (CI) and coupled cluster (CC). The final goal of DFT methods is to create suitable functionals which connect the electron density with the energy.[93–95]

The wave function of a system consisting of N electrons depends on 3N variables, since each electron is described by three spatial coordinates (x_i, y_i, z_i). The density is a much simpler quantity, since it depends only on three variables, the spatial coordinates x, y, and z, and the electron correlation is included from the beginning indirectly.[95]

Modern DFT is based on the two theorems of Hohenberg and Kohn (HK).[96] The first theorem states that the electronic wave function and thus all ground-state properties of an electronic system can be clearly determined from the electron density of the ground-state. The HK ground-

state energy can be expressed as,

$$E[\rho] = T[\rho] + V_{ee}[\rho] + V_{nuc}[\rho], \tag{4.1}$$

where T[ρ] is the kinetic energy functional, and the potential energy functionals $V_{ee}[\rho]$ and $V_{nuc}[\rho]$ are the electron-electron repulsion and the nuclear-electron attraction, respectively.

The second HK theorem states that this energy functional is for the ground-state density.[95] This determination avoids the problem of solving the many-body Schrödinger equation, and now the goal is to minimize this density functional via variational principle.

$$E_0 = \min_\rho E[\rho] \tag{4.2}$$

The problem remains that the functional $V_{ee}[\rho]$ is not known in an analytically usable form. To address this, the term for $V_{ee}[\rho]$ can be divided into,

$$V_{ee}[\rho] = J[\rho] + V_{ee,nc}[\rho], \tag{4.3}$$

where the first term J[ρ] is the classical Coulomb repulsion of the density with itself, while the second term $V_{ee,nc}[\rho]$ describes the "non-classical" part of the electron-electron repulsion. Now, the distribution for the energy functional can be written as,

$$E[\rho] = T[\rho] + V_{nuc}[\rho] + J[\rho] + V_{ee,nc}[\rho]. \tag{4.4}$$

The Coulomb energy J[ρ] and the electron-nuclear attraction $V_{nuc}[\rho]$ can be calculated directly from electron density. The "non-classical" contribution to the electron-electron repulsion $V_{ee,nc}[\rho]$ is small compared to the other contributions. The problem remains that the kinetic energy functional T[ρ] cannot be calculated directly from the electron density and which represents a major contribution of the total energy. Therefore, Kohn and Sham (KS) proposed a different approach.[97] They consider a reference system of non-interacting electrons with the same electron density as the "real" system of interacting electrons and used its kinetic energy, to approximate T[ρ]. This leads to the so-called Kohn-Sham equations on which all practical DFT calculations are based. Instead of the kinetic energy functional T[ρ], the kinetic energy functional of the non-interacting system $T_s[\rho]$ can be used,

$$E[\rho] = T_s[\rho] + V_{nuc}[\rho] + J[\rho] + V_{ee,nc}[\rho]. \tag{4.5}$$

The difference between T[ρ] and $T_s[\rho]$ is very small and, together with the energy of the non-classical electron-electron repulsion, it can be summarized to the exchange-correlation functional:

$$E_{xc}[\rho] = V_{ee,nc}[\rho] + (T[\rho] - T_s[\rho]). \tag{4.6}$$

Finally, the energy functional can be expressed as,

$$E[\rho] = T_s[\rho] + V_{nuc}[\rho] + J[\rho] + E_{xc}[\rho], \tag{4.7}$$

which is still formally exact, as so far none of the contributions have been neglected or approximated. However, in practical calculations the exchange-correlation energy must be approximated. But usually, this term is small and can be handled using approximations, successfully.

The most fundamental and simplest approximation is the local-density approximation (LDA), which was already proposed in 1965 by Kohn and Sham.[97] The idea of the LDA approach is that the exchange-correlation functional in each point in space depends only on the density in that same point. LDA is established in solid-state physics, but its tendency for overbinding in chemistry led to the development of more accurate methods. In this thesis, the BP86 exchange-correlation functional[98,99] is mainly used, which belongs to the group of so-called generalized gradient approximations (GGA). In addition to the LDA part, the electron density depends also on derivatives of the density, thus it is possible to better describe the inhomogeneous nature of molecular densities.[95]

4.2 X-ray Absorption Spectroscopy - TD-DFT

The XAS spectra in this work were calculated with time-dependent DFT (TD-DFT) following the established methodology[100–102] for selectively targeting excitations from the metal $1s$ orbital(s), implemented in the ADF program package. Such restricted-channel TD-DFT calculations have been applied extensively for K-edge XAS spectra of transition metal complexes.[69,103–110] In general, ordinary DFT cannot treat time-dependent problems nor describe excited electronic states, because DFT is strictly for ground state properties.[111] To address this problem, TD-DFT is an extension of density functional theory, and the computational and conceptual basics are analogous. The theoretical framework of TD-DFT was already introduced in 1984 by Runge and Gross, for details see Ref. [111, 112].

The calculated XAS intensities include second-order contributions due to the magnetic-dipole and electric-quadrupole transition moments, which are calculated using the origin-independent formalism of Ref. [113]. For complexes with more than one metal center, no localization of the core orbitals was performed (see also Ref. [69] for a discussion).

All calculations were performed using non-relativistic DFT because the inclusion of relativistic effects only shifts the spectra to other energies but leaves the overall XAS and also VtC-XES spectra (see Sec. 4.3) spectra unaffected. For including a first approximation of environment effects, the COSMO solvation model[114] with default parameters has been used for both spectroscopic approaches. Furthermore, a constant shift, which depends on the used DFT functional

and basis set, must be applied in order to align calculated and experimental spectra.

4.3 X-ray Emission Spectroscopy - ΔDFT

For most of the calculated X-ray emission spectra included in this work, the simple ΔDFT approach of Lee et al. [115] was used (see also Refs. [116–118]). This method is also implemented in the ADF program package.

In ΔDFT, the transition energies were calculated as occupied orbital energy differences, where ϵ_{core} is the orbital energy of the core orbital (i.e., the copper or iron $1s$ orbital) and the relevant occupied orbital above the electronic core state is defined as ϵ_n (n-th occupied orbital).

$$E_n = (\epsilon_n - \epsilon_{\text{core}}) + \Delta E_{\text{shift}} \tag{4.8}$$

The term ΔE_{shift} stands for a constant shift, which depends on the used functional and basis set, in order to align calculated and experimental spectra. The corresponding dipole intensities will be given as dimensionless oscillator strengths and can be obtained in atomic units as

$$f_n = \frac{2E_n}{3}\langle\phi_{\text{core}}|\hat{\boldsymbol{\mu}}|\phi_n\rangle^2. \tag{4.9}$$

$\phi_{\text{core}}(\boldsymbol{r})$ and $\phi_n(\boldsymbol{r})$ are the relevant core orbital, respectively, the n-th occupied orbital above the core orbital, and the electric dipole operator is given as $\hat{\boldsymbol{\mu}}$. Higher-order intensity contributions were calculated as described in Refs. [91, 113], but can be neglected for the VtC-XES spectra of the iron and copper complexes considered in this work. All orbitals and orbital energies refer to the occupied orbitals as obtained in the ground-state DFT calculation.

Even though this method constitutes the simplest possible approach for the DFT calculation of XES spectra, it has been shown to be reliable for VtC-XES spectra of diverse transition metal complexes,[15–17,21,67,90,106,115,118–120] including the ones considered here.[16] More sophisticated methods for the calculation of XES spectra are, for example, the TD-DFT approach,[121,122] which takes the core-hole relaxation into account and do not (or to a lesser extent) rely on a constant empirical shift of the calculated spectra. However, such approach is computationally more demanding and in general less robust when applied to transition-metal complexes. Moreover, it is also more sensitive to the choice of the exchange-correlation functional while for the simple ΔDFT method the calculated VtC-XES spectra do not depend on the choice of exchange-correlation functional.[91] Finally, for the most of the complexes included in the work, the described simple ΔDFT method provides an excellent agreement with the experimental VtC-XES spectra.

Chapter 5

Application XAS: Cu K-edge X-ray absorption spectra depending on oxidation state and coordination environment

X-ray absorption spectroscopy (XAS) at the Cu K-edge is an important tool for probing the properties of copper centers in transition metal chemistry and catalysis. However, the interpretation of experimental XAS spectra requires a detailed understanding of the dependence of spectroscopic features on the local geometric and electronic structure, which can be established by theoretical X-ray spectroscopy. Here, a systematic computational study of the Cu K-edge XAS spectra of selected Cu complexes based on time-dependent density-functional theory in combination with a molecular orbital analysis of the relevant transitions is presented. For a series of Cu amine model complexes as well as a comprehensive test set of 12 Cu(I) and 5 Cu(II) complexes, the dependence of the pre-edge region in Cu K-edge XAS spectra on oxidation state and coordination geometry is revisited. While the calculations confirm earlier experimental assignments, also additional signatures of the ligand orbitals and identify the underlying orbital interactions can be revealed. The comprehensive picture revealed by this study will provide a reliable basis for the interpretation of *in situ* Cu K-edge XAS spectra of catalytic intermediates.

The publication [123] is based on this chapter of this thesis.

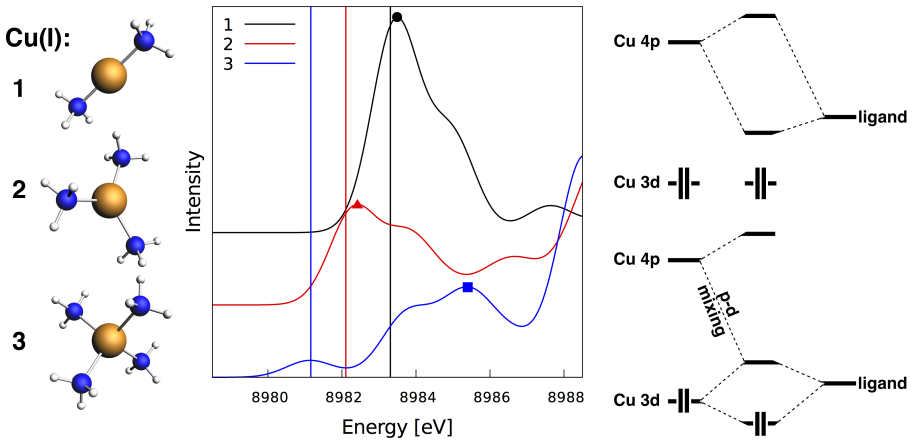

Figure 5.1: Schematic overview, which represents this chapter in one picture. Some examined model copper amine complexes are shown on the right side, which differ in their local ligand environment. In the middle calculated Cu K-edge XAS spectra of these complexes are shown with highlighted pre-peak maxima. To explain these peaks in detail, simple ligand picture will be used as shown in the right panel of this figure.

5.1 Introduction

Copper centers play a crucial role in many catalytic reactions, ranging from biological electron-transfer processes[124,125] to technical applications. As already mentioned in Sec. 3.1, the interest in Cu-based catalysts stems from the need to replace industrial processes requiring rare and expensive precious metals by sustainable alternatives based on earth-abundant base metals such as Fe and Cu (see, e.g., Refs. [74] and [75]). A prominent example of a technical application is the use of Cu-exchanged zeolites for the removal of NO_x from Diesel engine exhaust gases via selective catalytic reduction (SCR) with ammonia.[62,76,77]

In combination with other spectroscopic methods as well as quantum-chemical calculations, XAS and HERFD-XAS (see Sec. 3.1) have been successfully applied for investigating catalytic reaction mechanisms, e.g., of SCR catalysis with Cu-exchanged zeolites.[23,85–88]

The interpretation of the pre-edge in Cu K-edge XAS spectra largely relies on a pioneering study by Solomon and coworkers,[126] who investigated a comprehensive set of Cu(I) and Cu(II) model complexes featuring different coordination numbers and geometries. They identified signatures that can be used to assign the oxidation state, the coordination number and (partly) the coordination geometry and rationalized their results using ligand field theory. Recent spectroscopic studies,[13,127] partly exploiting the possibilities of HERFD methods, have found additional pre-edge features that are not accounted for by the simple ligand-field picture employed in Ref. [126], demonstrating the limitations of such models for the interpretation of XAS spectra.

Despite the importance of XAS of copper species for research in catalysis and the reliance of the interpretation of such XAS spectra on the assignments of Ref. [126], to the best of my knowledge these results have not been substantiated by computations so far. Even though for selected Cu complexes[13,127,128] and models of Cu centers in zeolites,[129,130] XAS spectra have been calculated and compared to experiment, a comprehensive understanding of the dependence of the features observed in Cu K-edge XAS spectra on the oxidation state and coordination geometry is still lacking (for a recent review, see Ref. [131]). To close this gap, a systematic computational study of the Cu K-edge XAS spectra of selected model complexes based on time-dependent density-functional theory (TD-DFT) is performed.

The goal of this study is two-fold: First, by exploiting the additional information on the individual molecular orbital transitions contributing to experimentally observed peaks provided by computations, the aim is to obtain insights into the connection between the XAS spectra and the electronic structure of the model complexes. This can in turn be used to judge the reliability of previously identified signatures and help to clarify the domain of applicability as well as the limitations of a simplified ligand-field picture. Second, the aim is to establish the accuracy of TD-DFT calculations of XAS spectra for copper species with respect to the signatures commonly used in the interpretation of XAS spectra. This will be valuable for future computational studies combining experiment and theory to unravel copper-catalyzed reaction mechanisms.

5.2 Computational Methodology

The molecular structures of all considered copper model complexes have been optimized using density-functional theory (DFT) as implemented in the Amsterdam density functional (ADF) program package,[132,133] employing the BP86 exchange-correlation functional[98,99] and the Slater-type TZ2P basis set.[134] For all Cu(I) complexes, the ground state is a closed-shell singlet spin state. For all Cu(II) complexes, spin-unrestricted calculations were performed for the doublet ground state.

The XAS spectra were calculated with time-dependent density-functional theory (TD-DFT) following the established methodology[100–102] for selectively targeting excitations from the Cu 1s orbital(s). Such restricted-channel TD-DFT calculations have been applied extensively for K-edge XAS spectra of transition metal complexes.[69,103–110] The calculated XAS intensities include second-order contributions due to the magnetic-dipole and electric-quadrupole transition moments, which are calculated using the origin-independent formalism of Ref. [113]. For complexes with more than one copper center, no localization of the core orbitals was performed (see also Ref. [69] for a discussion.

In the calculations of the XAS spectra, the same exchange-correlation functional as in the geometry optimization and the Slater-type QZ4P basis set were employed. To verify the results and

to assess their dependence on the exchange-correlation functional, the complexes were also optimized and afterwards XAS spectra were calculated using the B3LYP hybrid exchange-correlation functional[135] with the same Slater-type basis sets.

All calculations are performed using non-relativistic DFT because the inclusion of relativistic effects only shifts the spectra to other energies but leaves the overall XAS spectra unaffected. For all XAS calculations the COSMO solvation model with default parameters has been used to include a first approximation of environment effects. All XAS spectra calculated with BP86/QZ4P have been shifted by 233.50 eV and all XAS spectra calculated with B3LYP/QZ4P have been shifted by 196.85 eV. These shifts have been chosen such that the maximum of the most intense pre-edge peak of complex **A** is aligned with the peak at 8983.6 eV in the experimental spectrum measured for the complex in Ref. [126]. To plot the XAS spectra, a Gaussian line broadening with a full-width at half maximum (FWHM) of 1.5 eV was applied throughout.

5.3 Results and Discussion

5.3.1 Interpretation of Cu K-edge XAS spectra: Copper amine model complexes as a first test case

XAS probes transitions from core orbitals to unoccupied electronic states. For XAS at the Cu K-edge, an electron is excited from the Cu 1*s* core orbital. In a molecular orbital (MO) picture, the

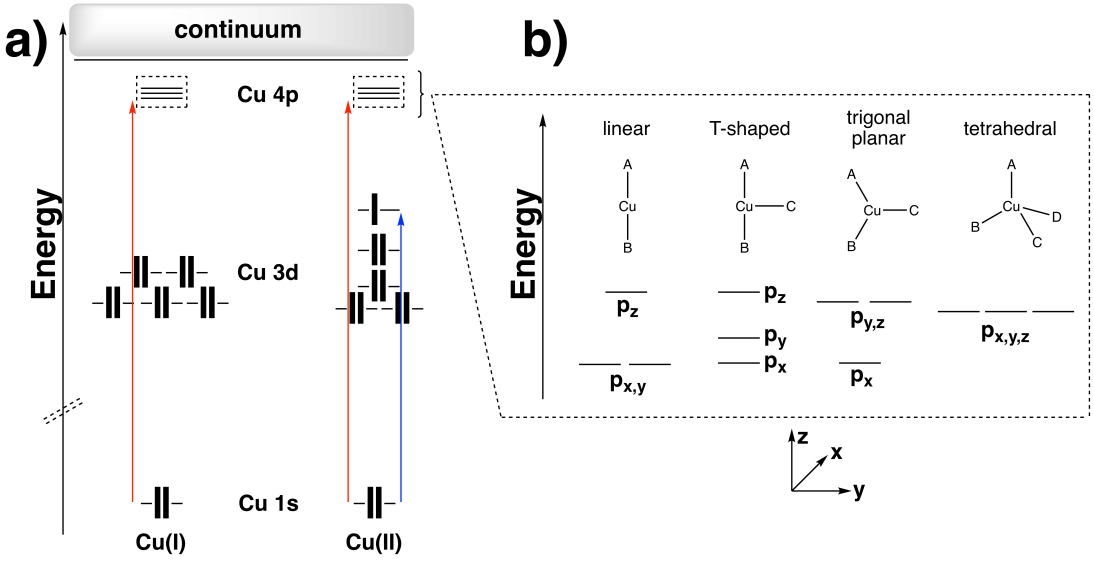

Figure 5.2: (a) Schematic illustration of the relevant orbital transitions in the Cu K-edge XAS spectra for Cu(I) complexes (left) and for Cu(II) complexes (right). (b) Ligand field splitting of the unoccupied copper 4p orbitals in different coordination geometries.

pre-edge region is due to transitions from the core orbital to well-defined unoccupied MOs (see Fig. 5.2a). The ionization edge marks the onset of transitions into unbound continuum states, and the region of XAS spectra past the edge, the extended X-ray absorption fine structure (EXAFS) region, can be interpreted using scattering theory.[136] Here, the focus is on the pre-edge region that provides unique information on the electronic structure by probing the low-lying unoccupied MOs.[68]

For Cu(I) with a d^{10} electron configuration, the lowest lying unoccupied metal orbitals are the $4p$ orbitals. Thus, one expects the pre-edge of the XAS spectra to be mainly determined by these unoccupied $4p$ orbitals. For a first analysis of the dependence of the Cu K-edge XAS spectra on the coordination environment, spectra for a test set of Cu(I) amine model complexes were calculated: linear $[Cu^{I}(NH_3)_2]^+$ (**1**) with a coordination number of two, trigonal planar $[Cu^{I}(NH_3)_3]^+$ (**2**) with a coordination number of three, and tetrahedral $[Cu^{I}(NH_3)_4]^+$ (**3**) with a coordination number of four (see Fig. 5.3a).

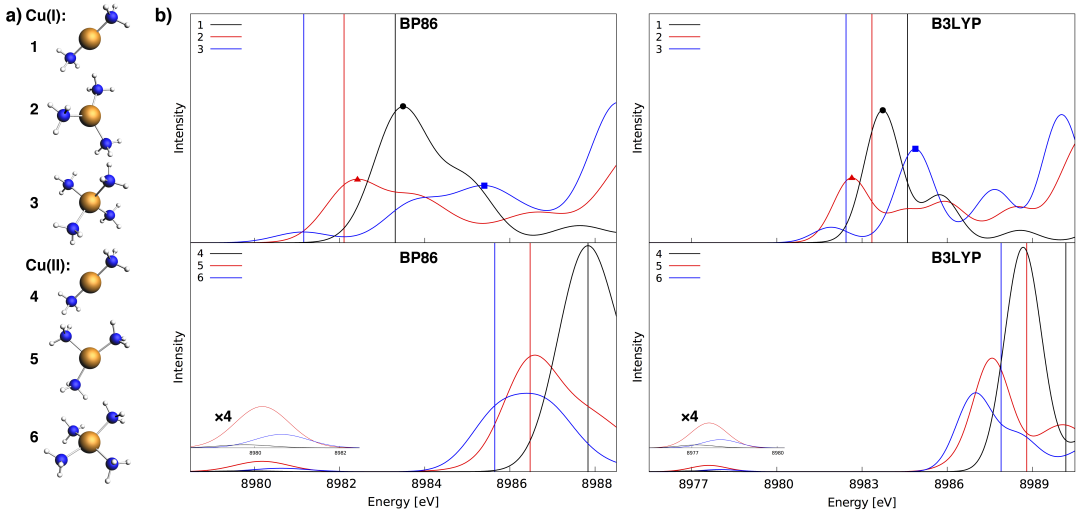

Figure 5.3: (a) Molecular structures of the considered series of copper amine complexes $[Cu^{I}(NH_3)_n]^+$ (**1-3**) and $[Cu^{II}(NH_3)_n]^{2+}$ (**4-6**) ($n = 2, 3, 4$); (b) Cu K-edge XAS spectra of $[Cu^{I}(NH_3)_n]^+$ (top) and $[Cu^{II}(NH_3)_n]^{2+}$ (bottom) calculated with BP86/QZ4P (left) and B3LYP/QZ4P (right). The calculated ionization thresholds are indicated by vertical lines.

The calculated XAS spectra are shown in Fig. 5.3b. Details on the Computational Methodology are given in the corresponding section above. An empirical, method-dependent constant shift has to be applied in order to align the calculated spectra with experiment.[101,137] Here, a consistent shift has been applied to all spectra calculated with the same method, even though different types of complexes (e.g., with different charge states) might require a different shift.[102,137] Therefore, the absolute energies of the peaks in the calculated spectra will not always precisely match the experimental ones. Moreover, it could be obtained that in the region above the calculated ionization threshold (marked by a vertical line in the plots of the spectra) spurious states can

appear that arise from the inability of atom-centered basis functions to describe the quasi-continuum states.[69,138] Thus, the peaks in this region have to be analyzed carefully to ensure that they correspond to chemically meaningful unoccupied states. To judge the sensitivity of the calculated spectra to the choice of the exchange-correlation functional, spectra calculated with both the pure generalized-gradient approximation (GGA) functional BP86 and the hybrid functional B3LYP are shown. For B3LYP functional the ionization threshold is shifted to higher energies, which is due to the wrong asymptotic behavior of the pure GGA exchange-correlation potential[139] that is corrected by the admixture of exact exchange in the hybrid functional. Therefore, peaks that are close to or just behind the calculated ionization threshold for BP86 are in fact pre-edge features, as is shown by the B3LYP calculations.

In the calculated spectra of the Cu(I) model complexes in Fig. 5.3b, the positions of the most intense pre-edge peak have been marked by circle, triangle, and square, respectively. For the linear Cu(I) model complex, $[Cu^{I}(NH_3)_2]^+$ (**1**), the calculated spectra show an intense peak at ca. 8983.5 eV. For the trigonal-planar Cu(I) model complex, $[Cu^{I}(NH_3)_3]^+$ (**2**), the intensity of the most intense peak decreases by about 50 %. This is accompanied by a shift of the peak by ca. 1 eV to lower energies, while a similar shift is found for the ionization threshold. For the tetrahedral Cu(I) model complex, $[Cu^{I}(NH_3)_4]^+$ (**3**), the intensity in the region below 8985 eV decreases further. Here, the highest-intensity peak appears at ca. 8985.7 eV, with a maximum intensity similar to the one found for the trigonal-planar complex. In all three cases, for these main features in the pre-edge region, the BP86 and B3LYP calculations provide an identical qualitative picture.

These main features of the calculated pre-edge spectra qualitatively agree with the previous findings of Solomon and co-workers in Ref. [126]. They assigned an intense pre-edge peak between ca. 8983 eV and 8985 eV to linear Cu(I) complexes. The intensity of this peak was found to decrease for Cu(I) complexes with a coordination number of three and to shift to ca. 8985-8986 eV for Cu(I) complexes with a coordination number of four.

To further analyze the calculated spectra, Fig. 5.4 shows the unoccupied molecular orbitals that are responsible for the most intense transitions and highlights the contributions of these transitions to the overall spectra. These can be compared to the ligand field picture employed in Ref. [126] that is illustrated in Fig. 5.2b. For the linear Cu(I) model complex **1**, the $4p_x$ and $4p_y$ orbitals (perpendicular to the bond axis) contribute equally to the intense pre-edge peak at ca. 8983.5 eV. This is consistent with the ligand field picture, in which the $4p_z$ orbital is shifted to higher energies compared to the degenerate $4p_x$ and $4p_y$ orbitals.

Explaining the intensity differences when comparing the transitions to the $4p_x$ and $4p_y$ orbitals with the transition to the $4p_z$ orbital already requires extending the ligand field picture with molecular orbital considerations. While the unoccupied $4p_x$ and $4p_y$ orbitals correspond to empty lone pair orbitals that are pure Cu $4p$ orbitals, the $4p_z$ orbital will mix with ligand orbitals, i.e.,

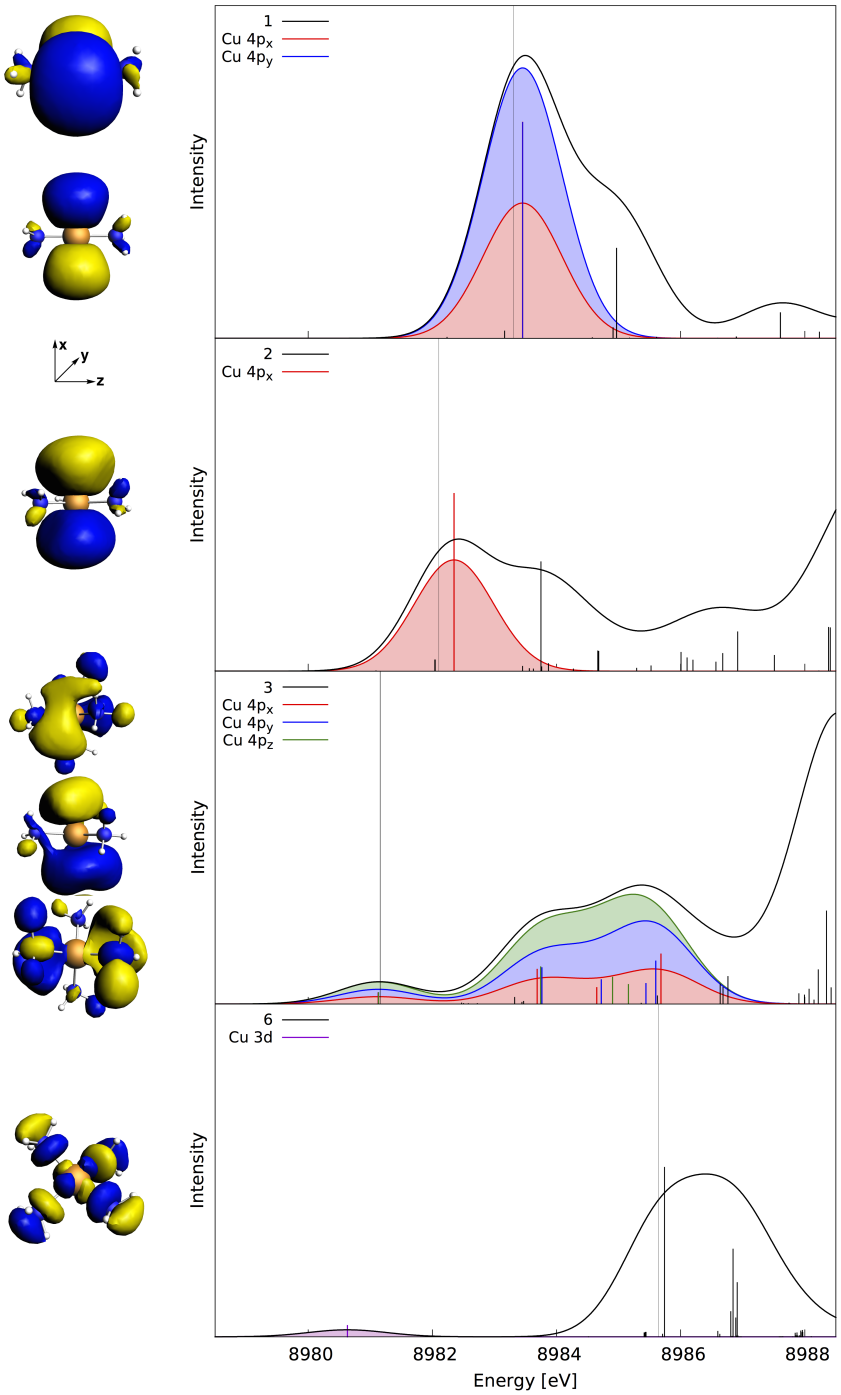

Figure 5.4: Molecular orbital analysis of the main contributions to the pre-edge regions in the calculated Cu K-edge XAS spectra (BP86/QZ4P) of linear $[Cu^{I}(NH_3)_2]^+$ (**1**), trigonal planar $[Cu^{I}(NH_3)_3]^+$ (**2**), tetrahedral $[Cu^{I}(NH_3)_4]^+$ (**3**) and for distorted square-planar $[Cu^{II}(NH_3)_4]^{2+}$ (**6**). Vertical bars indicate the individual transitions contributing to the calculated XAS spectra. The unoccupied orbitals responsible for the most relevant transitions are shown on the left, and the contributions of these transitions are highlighted in the calculated spectra shown on the right.

$|\phi^{\mathrm{MO}}_{4p_z}\rangle = a\,|\chi^{\mathrm{AO}}_{4p_z}\rangle + b\,|\chi^{\mathrm{AO}}_{L}\rangle$, where $|\phi^{\mathrm{MO}}_{4p_z}\rangle$ is the molecular orbital and $|\chi^{\mathrm{AO}}_{4p_z}\rangle$ and $|\chi^{\mathrm{AO}}_{L}\rangle$ are the Cu $4p_z$ atomic orbital and a suitable (linear combination of) ligand orbitals, respectively. Thus, while the intensity for the transition to the lone pair $4p_x$ orbital is

$$I_{1s\rightarrow 4p_x} \propto \left|\langle\phi_{1s}|\hat{\boldsymbol{\mu}}|\chi^{\mathrm{AO}}_{4p_x}\rangle\right|^2, \tag{5.1}$$

the mixing the ligand orbitals will decrease the intensity of the transition to the $4p_z$ orbital,

$$I_{1s\rightarrow 4p_z} \propto \left|\langle\phi_{1s}|\hat{\boldsymbol{\mu}}|\phi^{\mathrm{MO}}_{4p_z}\rangle\right|^2 \approx a^2\left|\langle\phi_{1s}|\hat{\boldsymbol{\mu}}|\chi^{\mathrm{AO}}_{4p_z}\rangle\right|^2. \tag{5.2}$$

That is, the intensity is determined by the Cu p-orbital contribution a^2 to the relevant unoccupied molecular orbitals. Note that other combinations of the p_z orbital with ligand orbitals will also be formed (e.g., the corresponding anti-bonding combination in the simple picture employed above) that will acquire intensity, but these molecular orbitals are shifted to higher energies (cf. the peak at ca. 8987.5 eV for **1**).

For a coordination number of three in a T-shaped geometry, the additional ligand will lift the degeneracy of the $4p_x$ and $4p_y$ orbitals and shift the $4p_y$ orbital to higher energies. For a trigonal-planar complex, the $4p_x$ orbital remains the lowest in energy, while the $4p_y$ and $4p_z$ orbitals become degenerate. For the trigonal-planar model complex $[\mathrm{Cu^I(NH_3)_3}]^+$ (**2**), the highest-intensity peak at ca. 8982.5 eV is now due to a transition to only the $4p_x$ orbital, which explains the decreased intensity compared to the linear case. The transitions to the degenerate $4p_y$ and $4p_z$ orbitals can be found at ca. 8984.8 eV in the calculated spectrum. As discussed above, because of mixing with ligand orbitals these have a decrease intensity compared to the transitions to pure Cu $4p$ orbitals.

Finally, for a tetrahedral ligand field the three $4p$ orbitals become degenerate. In the calculated spectrum of **3**, their largest contribution appears at ca. 8985.5 eV, to which all three $4p$ orbitals contribute equally. As all three Cu $4p$ orbitals now mix with ligand orbitals, the $4p$ contributions are distributed over a number of unoccupied molecular orbitals and the maximum intensity decreases. Therefore, the maximum intensity for **3** comparable to the one found for **2**, even though the $4p_x$ orbital now also contributes.

Thus, the dependence of the pre-edge regions in the calculated XAS spectra of the series of Cu(I) model complexes on the coordination geometry can be qualitatively explained by a simple ligand field picture. However, the calculated spectra show additional features, such as the shoulders at ca. 8985 eV and ca. 8984 eV for coordination number two and three, respectively, and the weak peak at ca. 8981 eV for coordination number four, are not accounted for in this ligand field picture. These will require a more elaborate molecular orbital picture that will be considered below in Sec. 5.3.3.

Next, the Cu K-edge XAS spectra of Cu(II) complexes were considered. Here, the electron

configuration is d^9, i.e., there is an additional singly unuccupied $3d$ orbital below the empty Cu $4p$ orbitals (cf. Fig. 5.2a). Therefore, an additional pre-edge peak at lower energies arising from the $1s \rightarrow 3d$ transition is expected. However, this transition is usually dipole-forbidden and only a very weak quadrupole transition can be observed.[102,113]

For a first assessment of the effect of the Cu oxidation state on the pre-edge XAS spectra, the above series has been extended to Cu(II) model complexes. Specifically, spectra for the Cu(II) amine model complexes $[Cu^{II}(NH_3)_2]^{2+}$ (**4**) with a linear coordination geometry, for $[Cu^{II}(NH_3)_3]^{2+}$ (**5**) with an almost T-shaped coordination geometry, and for $[Cu^{II}(NH_3)_4]^{2+}$ (**6**) with a distorted square-planar coordination geometry were calculated (see Fig. 5.3a). The calculated spectra are included in the lower panels of Fig. 5.3b.

The expected $1s \rightarrow 3d$ pre-edge peak appears at ca. 8980-8981 eV in the BP86/QZ4P calculations and at ca. 8977-8978 eV in the B3LYP/QZ4P calculations. In the experimental spectra of Ref. [126], this pre-edge peak was found at ca. 8979 eV. As discussed above, this slight mismatch is due to the well-known limitations of TD-DFT. The intensity of this additional Cu(II) pre-edge peak is the largest for the T-shaped complex **5**, and is significantly smaller for the four-coordinated complex **6**, while it is hardly visible on the scale of the figure for the linear complex **4**. In the lowest panel of Fig. 5.4, the unoccupied $3d$ orbital responsible for this pre-edge peak is shown and its contribution to the spectrum is highlighted.

In the calculated spectra of the model complexes **4** - **6**, the transitions into the unoccupied Cu $4p$ orbitals appear above ca. 8985 eV. For these transitions, a similar dependence on the coordination geometry as for the Cu(I) model complexes can be observed. The most intense peak in this region is found for the linear Cu(II) model complex $[Cu^{II}(NH_3)_2]^{2+}$ (**4**) and appears at ca. 8988-8989 eV. For the model complex $[Cu^{II}(NH_3)_3]^{2+}$ (**5**) with coordination number three, this peak shifts to lower energies (ca. 8987 eV) and its intensity is significantly reduced. Finally, for the model complex $[Cu^{II}(NH_3)_4]^{2+}$ (**6**) with a coordination number of four, the intensity is further reduced. These observations are consistent with the ligand-field picture employed above for the Cu(I) model complexes.

5.3.2 Calculated XAS spectra for a diverse test set of copper complexes

In the previous section, the dependence of the pre-edge in Cu K-edge XAS spectra on oxidation state and coordination environment for a series of model complexes that is not experimentally accessible were illustrated. As a next step, the study is extended to a diverse test set consisting of different types of Cu complexes, which are shown in Fig. 5.5. For compiling this test set, a selection of the compounds employed in the experimental study of Solomon and co-workers[126] were considered. All these complexes have been synthesized and characterized in the literature and experimental XAS spectra are available (see Ref. [126] and references therein). For each

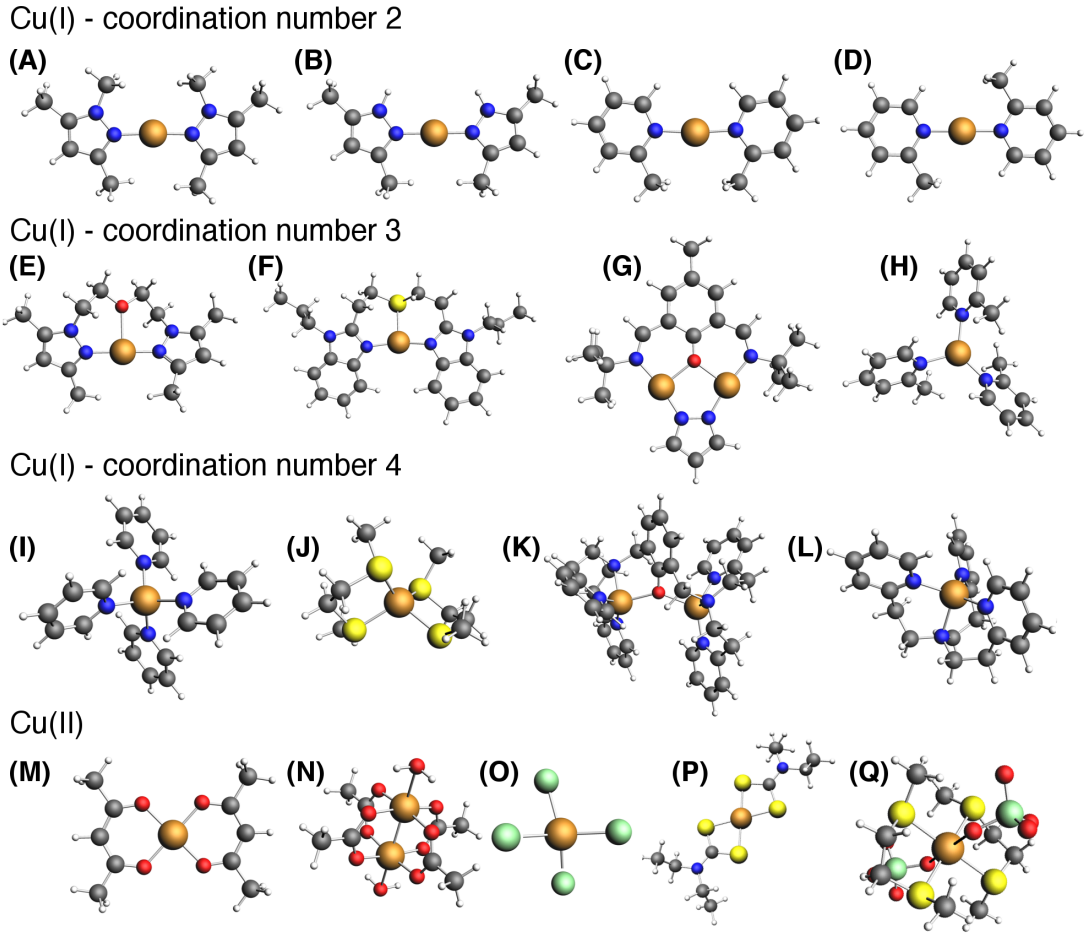

Figure 5.5: Optimized molecular structures of the test set of Cu complexes **A** - **Q**, calculated with the DFT functional BP86 and the TZ2P basis set.

type of coordination environment and oxidation state [Cu(I) with coordination number two, three, and four as well as Cu(II)] the compounds that are computationally most accessible have been selected from Ref. [126]. In particular, compounds that exist as well-defined molecular complexes in the crystal structures and for which the size of the ligands is still computationally tractable were preferably selected. In case that only few suitable complexes were available in Ref. [126] for a certain coordination number, the test set was augmented by additional complexes (namely **C**, **D**, and **H**) in order to be able to compare a variety of different ligand systems. All of these additional complexes are experimentally accessible (see below for literature references), but their Cu K-edge XAS spectra have not been published.

The first group (**A** - **D**) consists of four Cu(I) complexes with a coordination number of two that assume a linear structure. First, two pyrazole complexes, bis(1,3,5-trimethylpyrazole) copper(I) $[Cu^{I}(TMP)_2]^+$ (**A**) and bis(3,5-dimethylpyrazole) copper(I) $[Cu^{I}(DMP)_2]^+$ (**B**) that were taken from Ref. [126] are considered. In addition, *cis*-(di-2-picoline) copper(I) [*cis*-$Cu^{I}(2\text{-pic})_2]^+$ (**C**)

and *trans*-(di-2-picoline) copper(I) [*trans*-$Cu^{I}(2\text{-pic})_2]^+$ (**D**)[140] were included. The picoline ligand in these complexes was chosen because it is similar to the pyrazole-derived ligands in **A** and **B** in terms of the coordination via the nitrogen atom of a heterocycle, but it has different electronic properties, in particular a lower energy of the lowest unoccupied MO (LUMO).

The second group (**E** - **H**) is composed of three Cu(I) complexes with a coordination number of three, which were selected from those considered in Ref. [126]: (bis(2-(3,5-dimethyl-1-pyrazolyl)ethyl)ether) copper(I) $[Cu^{I}(pze)]^+$ (**E**) and (2,2'-bis(2-(N-propylbenzimidazolyl))-diethylsulfide) copper(I) $[Cu^{I}(L_1\text{-pr})]^+$ (**F**) feature a T-shaped geometry around the copper center. (ISOIM(di-*tert*-butyl)(pyrazolate)) di-copper(I) $[Cu^{I}_2(ISOIM)(t\text{-Bu})_2(pz)]$ (**G**) is a dinuclear Cu(I) complex with two copper centers, also with a T-shaped coordination geometry. In addition, (tri-2-picoline) copper(I) $[Cu^{I}(2\text{-pic})_3]^+$ (**H**)[141] is also considered. This fourth complex is included to draw the comparison to the linear complexes **C** and **D** and to also include a complex with a trigonal-planar coordination geometry.

The third group (**I** - **L**) consists of four Cu(I) complexes with a coordination number of four chosen from those employed in Ref. [126]. It contains the tetrahedral compounds, tetrapyridinecopper(I) $[Cu^{I}(py)_4]^+$ (**I**) and bis(2,5-dithiahexane) copper(I) $[Cu^{I}(2,5\text{-DTH})_2]^+$ (**J**) as well as a pyramidal dinuclear Cu(I) species $[Cu^{I}_2(XYL\text{-}O\text{-})]^+$ (**K**) and tris(ethyl-2-pyridyl)aminecopper(I) $[Cu^{I}(tepa)]^+$ (**L**) with a pseudo-tetrahedral geometry, that is distorted toward pyramidal.

Finally, the fourth group (**M** - **Q**) is composed of selected Cu(II) complexes from Ref. [126]. The first three of these, bis(acetylacetonate) copper(II) $[Cu^{II}(acac)_2]$ (**M**), succinate copper(II) dihydrate $[Cu^{II}(succ)(H_2O)_2]$ (**N**), and tetrachlorocuprate(II) $[Cu^{II}(Cl)_4]^{2-}$ (**O**), are classified as ionic complexes in Ref. [126]. Here, in **M** (coordination number 4) the Cu center has a square-planar coordination environment, **N** (coordination number 6) is a dinuclear complex with a distorted octahedral coordination environment for each copper center, and **O** (coordination number 4) has a pseudo-tetrahedral geometry. In the crystal structure of **N**,[142] each succinate ligands bridges two di-copper(II) center, resulting in infinite polymeric chains. To arrive at a computationally feasible molecular model complex, these ligands were cut in the middle and saturated the resulting terminal methyl groups, resulting in the tetrakis(acetate) dicopper(II) dihydrate $[Cu^{II}_2(acetate)_4(H_2O)_2]$ complex shown in Fig. 5.5. The group of Cu(II) complexes is completed by two complexes featuring sulfur ligand systems, bis(N,N-diethyldithiocarbamate) copper(II) $[Cu^{II}(Et_2NCS_2)_2]$ (**P**) and bis(2,5-dithiahexane) bisperchlorate copper(II) $[Cu^{II}(2,5\text{-}DTH)_2(ClO_4)_2]$ (**Q**) with a square-planar and a distorted octahedral ligand environment, respectively. These are classified as covalent complexes in Ref. [126]. For **Q**, the two perchlorate ligands are explicitly included in the computational model, as the Cu-O distance in the crystal structure amounts to only ca. 2.5 Å. For the other complexes, the counterions are not explicitly included in the computations, as they are generally not interacting directly with the copper centers (e.g., in **J** the distance between the Cu atom and the perchlorate counterions amounts to ca. 3.9 Å).

The XAS spectra calculated for these four groups of Cu complexes using BP86/QZ4P are shown in Fig. 5.6, and the spectra calculated with B3LYP/QZ4P are shown in Fig. 5.7 for comparison. The main features of the calculated XAS spectra for the different oxidation states and coordination environments are in agreement with the experimental spectra of Ref. [126] and match those found for the series of model complexes considered in the previous section (see Fig. 5.8). In particular, the linear Cu(I) complexes show an intense peak at ca. 8983.5-8984 eV. For the Cu(I) complexes with coordination number three the most intense peaks appear between ca. 8982 eV and 8984 eV, but the intensity in this region decreases significantly compared to the linear complexes. For the Cu(I) complexes with coordination number four, the intensity in this region decreases further, and the most intense peaks for these complexes appear at ca. 8985-8986.5 eV. For the Cu(II) complexes, a weak pre-edge peak appears below 8982 eV. Overall, the spectra calculated with BP86 and B3LYP provide a consistent picture of these general features.

For a more detailed comparison of calculated and experimental spectra, the main pre-edge peak of the Cu(I) complexes were considered. The position and maximum intensity of this peak in the experimental spectra of different Cu(I) complexes are compared in Fig. 2 of Ref. [126]. This peak was identified with the first intense pre-edge peak in the calculated spectra. In Fig. 5.6 and Fig. 5.7, the maximum of the corresponding peak is indicated with a circle, triangle, and square in the calculated spectra of the Cu(I) complexes with coordination number two, three, and four, respectively. In some ambiguous cases, the assignment of the peak in the calculated spectra that corresponds to the main pre-edge maximum was further guided by the MO analysis of the contributing transitions (see Sec. 5.3.3 below). While in the BP86/QZ4P calculation, this peak appears close to the calculated ionization edge for the complexes with coordination numbers two and three and ca. 2-4 eV behind the calculation edge for the complexes with coordination number four, they appear before or close to the ionization edge in the B3LYP/QZ4P calculations. In combination with the MO analysis (see Sec. 5.3.3 below), it can be confirmed that in both cases these peaks are not due to spurious quasi-continuum states.

The positions and maximum intensities of these main pre-edge calculated with both BP86/QZ4P and B3LYP/QZ4P are summarized in Fig. 5.8a using the same filled symbols as in Figs. 5.6 and 5.7. The results for the three groups of Cu(I) complexes can clearly be distinguished in these plots: For the complexes with coordination number two, the position of the main peak is between 8983.5 eV and 8984.5 eV and the normalized intensity is larger than 0.85, while for a coordination number of three, its position is between ca. 8982 eV and 8984 eV with a normalized intensity below 0.8. For a coordination number of four, the position of the main pre-edge peak is found between ca. 8984.5 and 8987 eV with a normalized intensity between 0.5 and 1.0. This is in agreement with the experimental findings summarized in Fig. 2 of Ref. [126].

For the considered complexes for which the positions and normalized absorption amplitudes are included in Fig. 2 of Ref. [126] (**A**, **B**, **F**, **G**, **I**, **K**, and **L**), these are also plotted in Figs. 5.8a as empty symbols using the same shape and color as for the corresponding calculation. Here, the

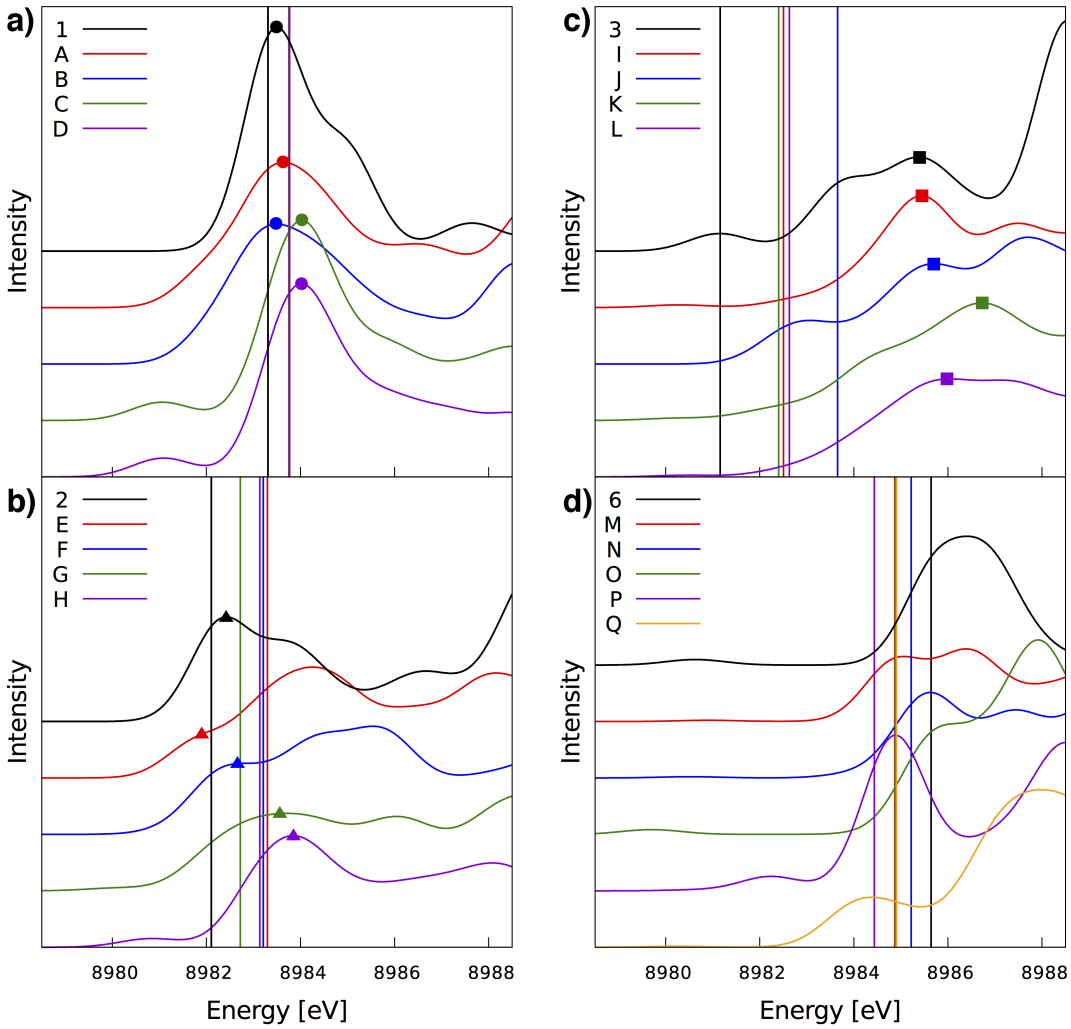

Figure 5.6: Cu K-edge XAS spectra of the Cu complexes **A** - **Q** calculated with **BP86/QZ4P**. The calculated ionization thresholds are indicated by vertical lines. (a) Cu(I) complexes **A** - **D** with coordination number two; (b) Cu(I) complexes **E** - **H** with coordination number three; (c) Cu(I) complexes **I** - **L** with coordination number four; and (d) Cu(II) complexes **M** - **Q**. The calculated spectra of the model complexes **1**, **2**, **3**, and **6** are included for comparison for the respective group of Cu complexes. For the Cu(I) complexes, the maximum of the peak corresponding to the main pre-edge feature are indicated by circles, triangles, and squares, respectively. See text for further details.

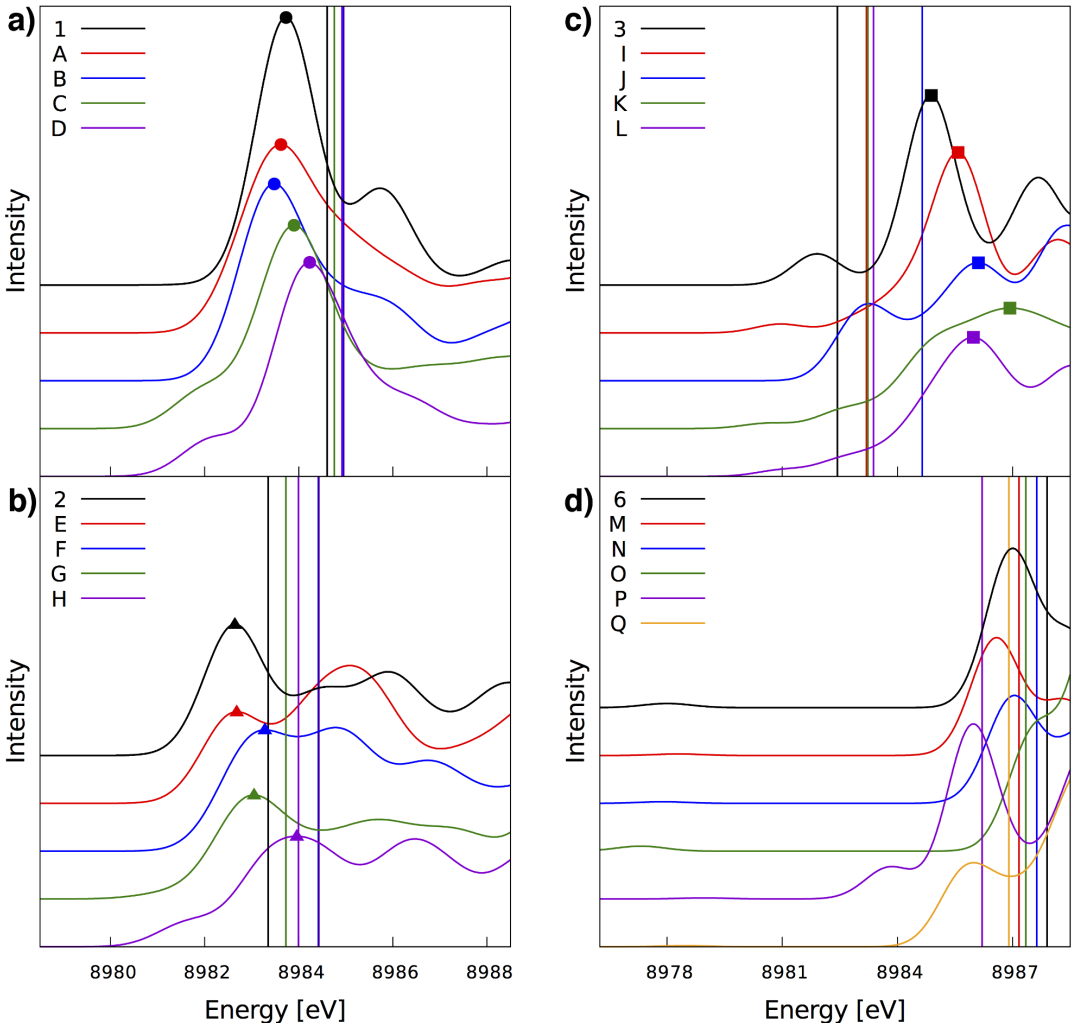

Figure 5.7: Cu K-edge XAS spectra of the Cu complexes **A** - **Q** calculated with **B3LYP/QZ4P**. The calculated ionization thresholds are indicated by vertical lines. (a) Cu(I) complexes **A** - **D** with coordination number two; (b) Cu(I) complexes **E** - **H** with coordination number three; (c) Cu(I) complexes **I** - **L** with coordination number four; and (d) Cu(II) complexes **M** - **Q**. The calculated spectra of the model complexes **1**, **2**, **3**, and **6** are included for comparison for the respective group of Cu complexes. For the Cu(I) complexes, the maximum of the peak corresponding to the main pre-edge feature are indicated by circles, triangles, and squares, respectively. See text for further details.

results for **A** have been used to align the experimental energies (see Computational Methodology) as well as the intensity scales, i.e., the calculated intensities have been normalized such that the normalized intensity at the calculated pre-edge maximum for **A** matches the normalized absorption amplitude of 1.05 at the pre-edge maximum in the experimental spectrum. In all cases, the experimental peak position and intensity fall within the region corresponding to the correct group and they are generally very close to the corresponding calculated ones. A direct comparison of the calculated and experimental peak positions and intensities is shown in Fig. 5.8b for both BP86/QZ4P and B3LYP/QZ4P.

The comparison of the positions and normalized intensities of the pre-edge peak maxima is prone to several inaccuracies both in the extraction of the peak maxima from the calculated spectra and due to the limited availability of the original experimental data of Ref. [126]. The position and height of the calculated peak maxima depends on the amount of empirical peak broadening used when plotting the spectra, especially in cases where several transitions contribute to the main pre-edge peak. Directly comparing calculated and experimental peak intensities generally requires a subtraction of the rising edge as well as a deconvolution for the experimental spectra. In light of these limitations, the agreement between the computations and the available experimental data can be considered satisfactory. The largest deviations of up to ca. 1.5 eV occur for the peak positions of **F** and **K**, where the relevant pre-edge region is rather flat. In all other cases, the differences between experimental and calculated peak positions are below 0.4 eV. For the maximum intensities, the calculations slightly underestimate those of the Cu(I) complexes with coordination number three, while it is slightly overestimated for coordination number four. Overall, the agreement between experiment and computations is similar for BP86 and for B3LYP.

The calculated spectra agree with the experimental spectra with respect to the general features and the positions and intensities of the first pre-edge peak in the calculated Cu(I) spectra are in good agreement with the available experimental data. However, a closer comparison of the calculated XAS spectra within the different groups of complexes shows some changes between complexes with the same oxidation state and coordination environment. The positions of the intense peaks vary among similar complexes and for some complexes, additional shoulders or weak peaks appear in the low-energy region of the spectra. These variations will be analyzed in more detail below.

While in general BP86 and B3LYP provide qualitatively similar spectra, in several cases the energy splitting between peaks differ. For instance, the weak peak at ca. 8981 eV in complexes **C** and **D** for BP86 appears as a shoulder at ca. 8981 eV in the B3LYP calculations. Such a pronounced dependence of the energy splittings between peaks is due to the well-know limitations of TD-DFT in describing the energies of charge-transfer excitations[68,106] that could be overcome for the specific systems by employing range-separated hybrid functionals[143,144] or by carefully tuning the exact exchange admixture.[106] However, even though the exact position of these peaks

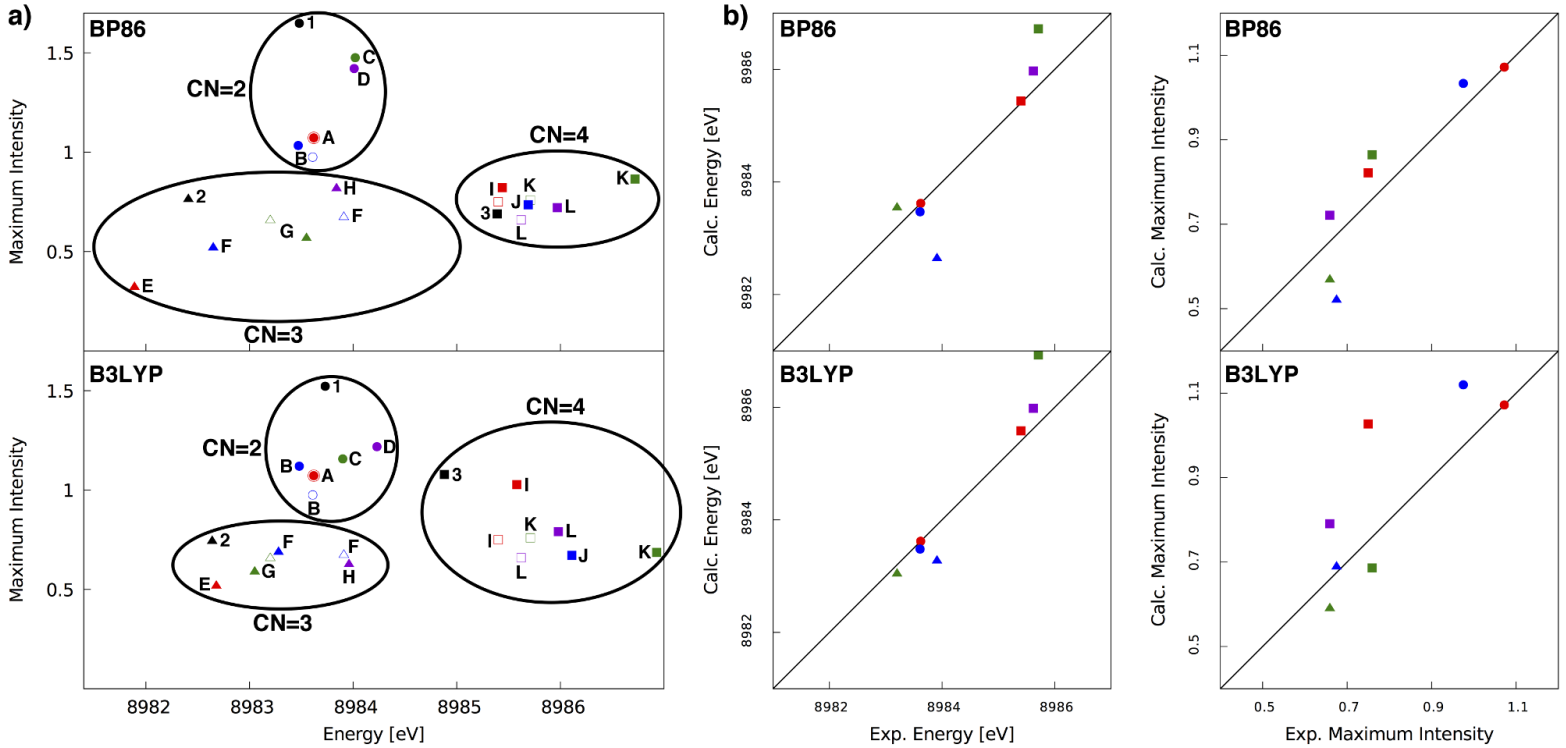

Figure 5.8: (a) Positions and maximum intensities (filled symbols) of the main pre-edge peaks for all Cu(I) complexes **A** - **L** calculated with BP86/QZ4P (top) and B3LYP/QZ4P (bottom). The experimental pre-edge maxima extracted from Fig. 2 of Ref. [126] are included as empty symbols where available. (b) Comparison of the experimental positions and intensities with those calculated with BP86/QZ4P (top) and B3LYP/QZ4P (bottom). The black line indicates equality of experimental and calculated values.

might be unclear, an analysis of the underlying molecular orbital transitions is still possible.[68] In the following, the spectra calculated with BP86 will be employed for a more detailed analysis.

5.3.3 MO analysis of the calculated XAS spectra for copper(I) complexes

Here, a more detailed analysis of the calculated XAS spectra is presented, particularly of the variations within the groups of complexes with the same oxidation state and similar coordination environments (cf. Fig. 5.6). This allows to identify to what extent the features identified in Sec. 5.3.1 for the series of copper amine model complexes and the ligand field picture that was employed to explain them are still valid for realistic, experimentally accessible Cu complexes. Furthermore, the aim is to identify additional mechanisms that influence the electronic structure of Cu complexes that can possibly be probed in XAS experiments.

First, the Cu(I) model complexes **A** - **D** with coordination number two in a linear coordination environment (cf. Fig. 5.6a) were considered. The calculated spectra of the two pyrazole Cu(I) complexes **A** and **B** are almost identical and agree with the one of the linear model complex $[Cu^{I}(NH_3)_2]^+$ (**1**), but the intense peak at ca. 8983 eV is broader than for the amine model complex. For the picoline Cu(I) complexes **C** and **D**, this intense peak is shifted to slightly higher energies and an additional weak peak appears at ca. 8981 eV.

In Fig. 5.9, the calculated spectra are decomposed into the contributions of different types of unoccupied orbitals. Because the unoccupied Cu orbitals mix with unoccupied ligand orbitals, the Cu $4p_x$ and Cu $4p_y$ orbitals identified as responsible for the intense pre-edge peak now contribute to several unoccupied molecular orbitals. The XAS intensity due to unoccupied MOs dominated by the Cu $4p_x$ orbital is highlighted in red in the figure, whereas the XAS intensity due to unoccupied MOs dominated by Cu p_y is highlighted in blue. Isosurface plots of the most important of those MOs are also shown.

For **A** and **B**, the interaction of the Cu $4p_y$ orbital (that lies in the plane of the two pyrazole ligands) with the ligand orbitals is rather weak and does not change the position of the corresponding transitions. However, the Cu $4p_x$ orbital (that is perpendicular to the two pyrazole ligands) strongly interacts with the LUMOs of the pyrazole ligands, resulting in a bonding and an anti-bonding combination. These are split almost symmetrically around the Cu $4p_y$, resulting in the observed broadening of the peak. The two unoccupied MOs have significant contributions of both the Cu $4p_y$ and the pyrazole orbitals. These orbital interactions are illustrated schematically in Fig. 5.10a.

For **C** and **D**, the interaction of the Cu $4p_y$ orbital remains small, but the interaction of the Cu $4p_x$ with the LUMOs of the picoline ligands changes. The ligand LUMOs are now at lower energies, resulting in a bonding combination at lower energies (ca. 8981 eV) that this dominated by the ligand LUMOs with a smaller Cu $4p_x$ contribution and an anti-bonding combination at

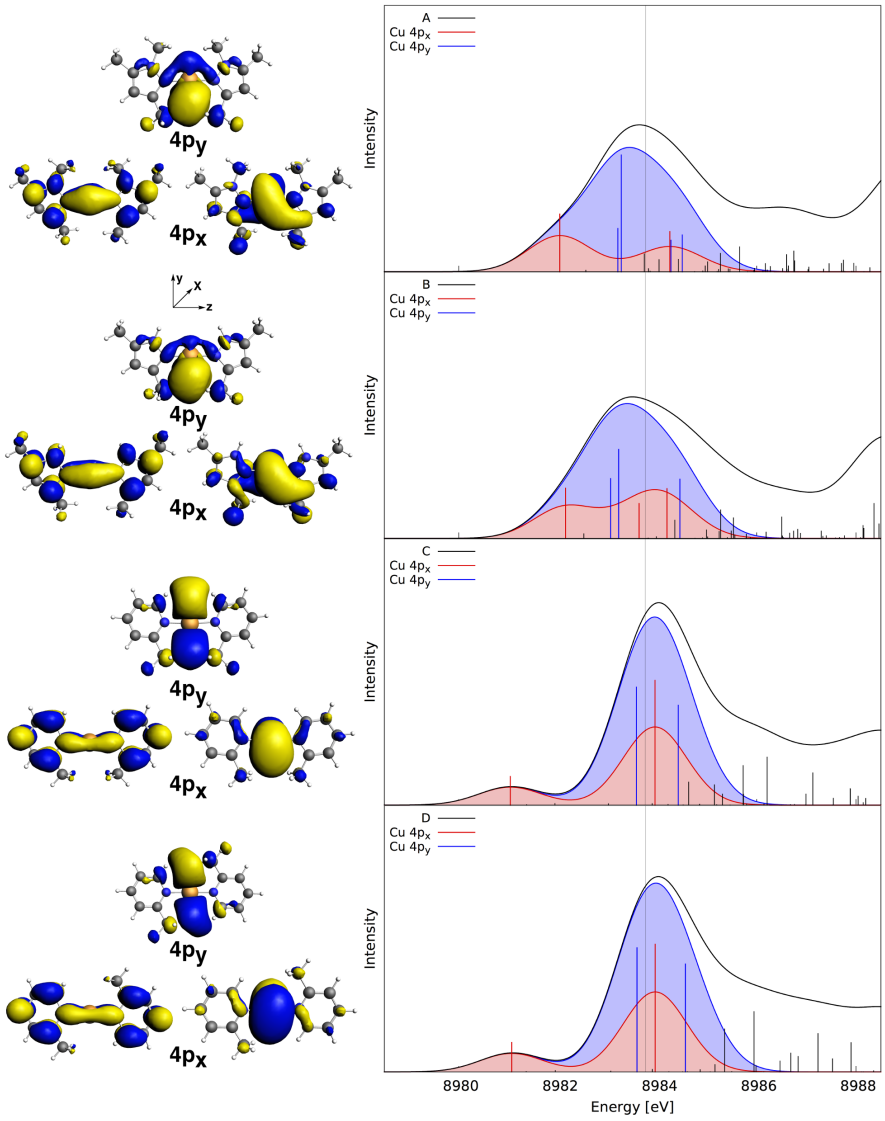

Figure 5.9: Molecular orbital analysis of the main contributions to the pre-edge regions in the calculated Cu K-edge XAS spectra (BP86/QZ4P) of the linear Cu(I) complexes **A** - **D** with coordination number two. Vertical bars indicate the individual transitions contributing to the calculated XAS spectra. The unoccupied orbitals responsible for the most relevant transitions are shown on the left, and the contributions of these transitions are highlighted in the calculated spectra shown on the right.

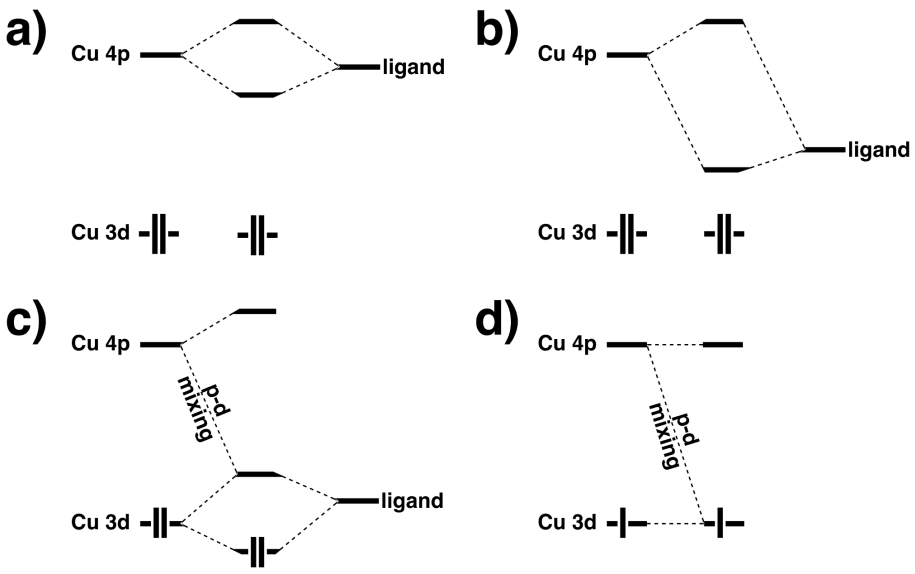

Figure 5.10: Schematic MO diagrams illustrating different mechanisms resulting in additional features in the Cu K-edge XAS spectra compared to the ligand-field picture of Fig. 5.2. (a) Symmetric mixing of Cu 4*p* and unoccupied ligand orbitals; (b) non-symmetric mixing of Cu 4*p* and low-lying unoccupied ligand orbitals resulting in MLCT transitions; (c) mixing of occupied Cu 3*d* and low-lying unoccupied ligand orbitals for Cu(I) complexes; (d) mixing of unoccupied Cu 3*d* and Cu 4*p* orbitals for Cu(II) complexes.

higher energies (ca. 8984 eV) that is dominated by the Cu $4p_x$ orbitals with a smaller contribution of the ligand LUMOs (see Fig. 5.10b). The former is responsible for the additional weak peak appearing at ca. 8981 eV. Thus, this peak is caused by a transition from the Cu core orbital to an unoccupied ligand orbital that acquires intensity through the admixture of Cu 4*p* contributions and can be classified as a metal-ligand charge transfer (MLCT) excitation. Such weak pre-edge peaks due to MLCT excitations to low-lying unoccupied ligand orbitals have recently been observed in HERFD-XAS spectra of Cu(I) complexes with bipyridine ligands.[13]

For the Cu(I) complexes **E** - **H** with coordination number three all calculated XAS spectra are shown in Fig 5.6b and a comparison highlighting the contribution of the most relevant unoccupied MOs is shown in Fig. 5.11. For all complexes, the main pre-edge peak appears between ca. 8982 eV and 8984 eV it has a decreased intensity compared to the linear complexes. This is consistent with the results for $[Cu^{I}(NH_3)_3]^+$ (**2**) as well as the ligand field picture discussed earlier.

The main contribution to this pre-edge peak is for all complexes a transition from the core orbital to an unoccupied orbital that is dominated by the Cu $4p_x$ orbital. Isosurface plots of these orbitals are included in Fig. 5.11. For the dinuclear Cu complex **G**, this $4p_x$ peak is slightly broadened due to the interaction of the unoccupied $4p_x$ orbitals at the two copper centers. In addition, a very weak pre-edge peak at ca. 8980 eV appears for complex **G**. The analysis of

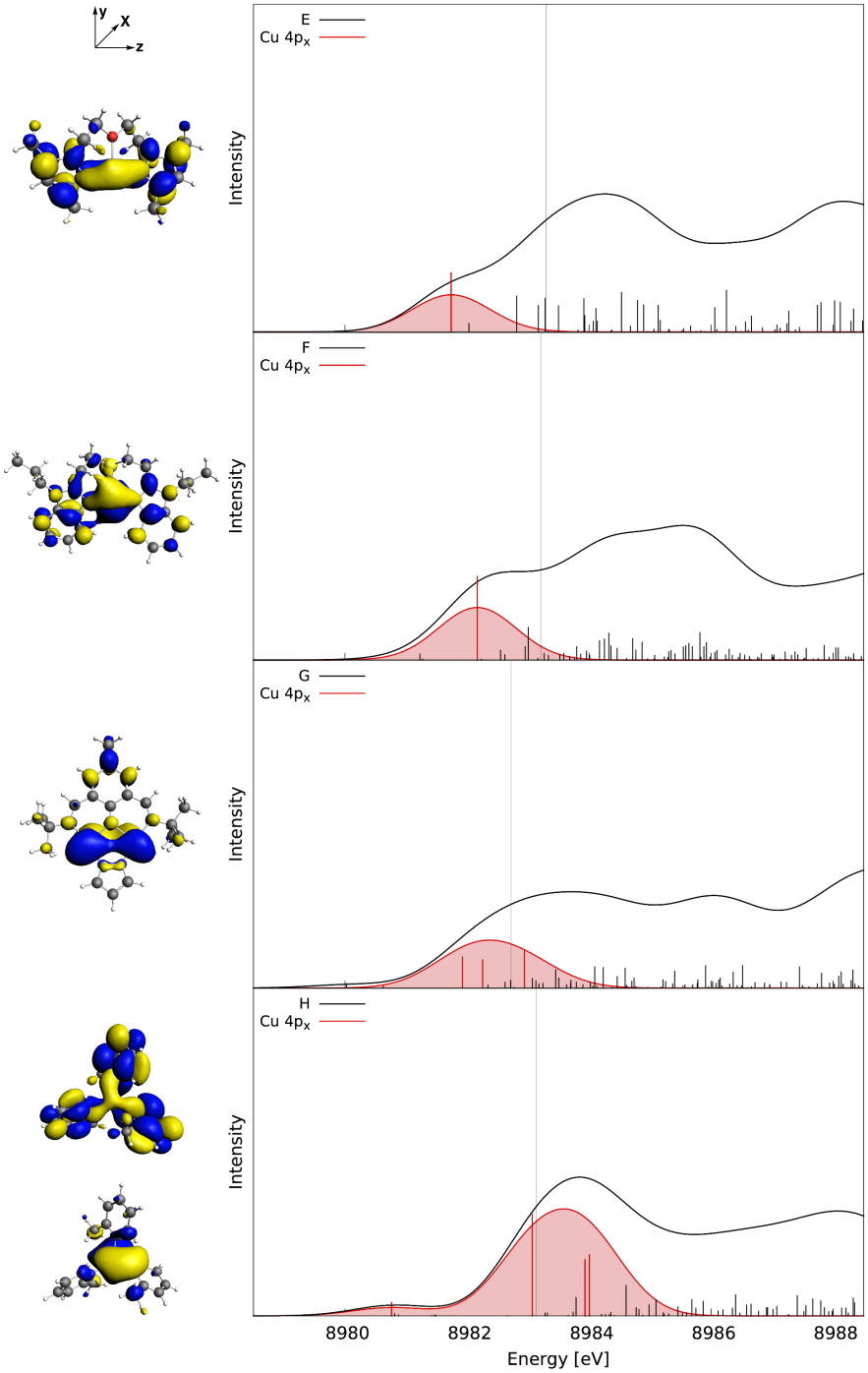

Figure 5.11: Molecular orbital analysis of the main contributions to the pre-edge regions in the calculated Cu K-edge XAS spectra (BP86/QZ4P) of the Cu(I) complexes **E** - **H** with coordination number three. Vertical bars indicate the individual transitions contributing to the calculated XAS spectra. The unoccupied orbitals responsible for the most relevant transitions are shown on the left, and the contributions of these transitions are highlighted in the calculated spectra shown on the right.

the corresponding unoccupied orbitals shows that this peak is due to mixing of the occupied $3d$ orbitals with the low-lying unoccupied ligand orbitals. The transition into these orbitals acquires a small intensity due to p-d mixing. These orbital interactions are illustrated schematically in Fig. 5.10c.

For the trigonal-planar Cu(I) complex with picoline ligands **H**, the interaction of the low-lying ligand LUMO and the unoccupied Cu $4p_x$ orbital leads to a weak MLCT pre-edge peak at ca. 8981 eV. The mechanism responsible for this interaction is identical to the one discussed for the linear Cu(I) picoline complexes above (cf. Fig. 5.10b).

Finally, consider the Cu(I) complexes with coordination number four **I** - **L** (see Fig. 5.6c). For all four complexes, the intensity in the region below 8985 eV decreases compared to those with coordination numbers two and three, and for all four complexes the highest-intensity peak appears at ca. 8985-8987 eV. This is consistent with the results for $[Cu^{I}(NH_3)_4]^+$ discussed in Sec. 5.3.1.

A comparison of the spectra of **I** - **L** highlighting the contribution of the most relevant unoccupied MOs is shown in Fig. 5.12. For all four complexes, the unoccupied Cu $4p_x$, $4p_y$, and $4p_z$ contribute equally to the most intense peaks, which agrees with the ligand field picture discussed previously. For **K** and **L**, the Cu $4p$ orbitals contribute to a large number of unoccupied orbitals in the regions between 8983 eV and 8989 eV and it becomes impossible to clearly distinguish the different $4p_{x,y,z}$ contributions.

Additional features can be identified for all four complexes. For **I**, **K** and **L**, a weak pre-edge peak appears at ca. 8980 eV. This peak is due to mixing of the occupied $3d$ orbitals and unoccupied ligand orbitals, as discussed above for **G**, i.e., it arises according to the mechanism illustrated in Fig. 5.10c. This assignment is supported by the observation that 18 %, 19 % and 29 % of the intensity of this peak are due to quadrupole contributions for **I**, **K** and **L**, respectively.

For **J**, an additional shoulder appears at 8982-8984 eV. This is caused by the lowest-lying unoccupied orbitals of the sulfur ligands, which acquire intensity by admixture of Cu $4p$ orbitals, i.e., this shoulder is due to MLCT excitations arising due to nonsymmetric mixing of Cu $4p$ orbitals and low-lying ligand orbitals as illustrated in Fig. 5.10b. Such a MLCT peak is also observed for the model complex **3** (see Fig. 5.4), where it is caused by the low-lying bonding combination of the unoccupied NH_3 $3s$ orbitals.

Overall, the main features of the calculated Cu K-edge XAS spectra of the considered Cu(I) complexes with different coordination environments are explained by the simple ligand field picture introduced in Ref. [126] (cf. Fig. 5.2). Additional features arising from interactions with unoccupied ligand orbitals are found for some complexes and can be explained by the schematic MO diagrams shown in Fig. 5.10a (symmetric Cu $4p$ - ligand mixing), Fig. 5.10b (MLCT to low-lying ligand orbitals due to non-symmetric Cu $4p$ - ligand mixing), and Fig. 5.10c (Cu $3d$ -

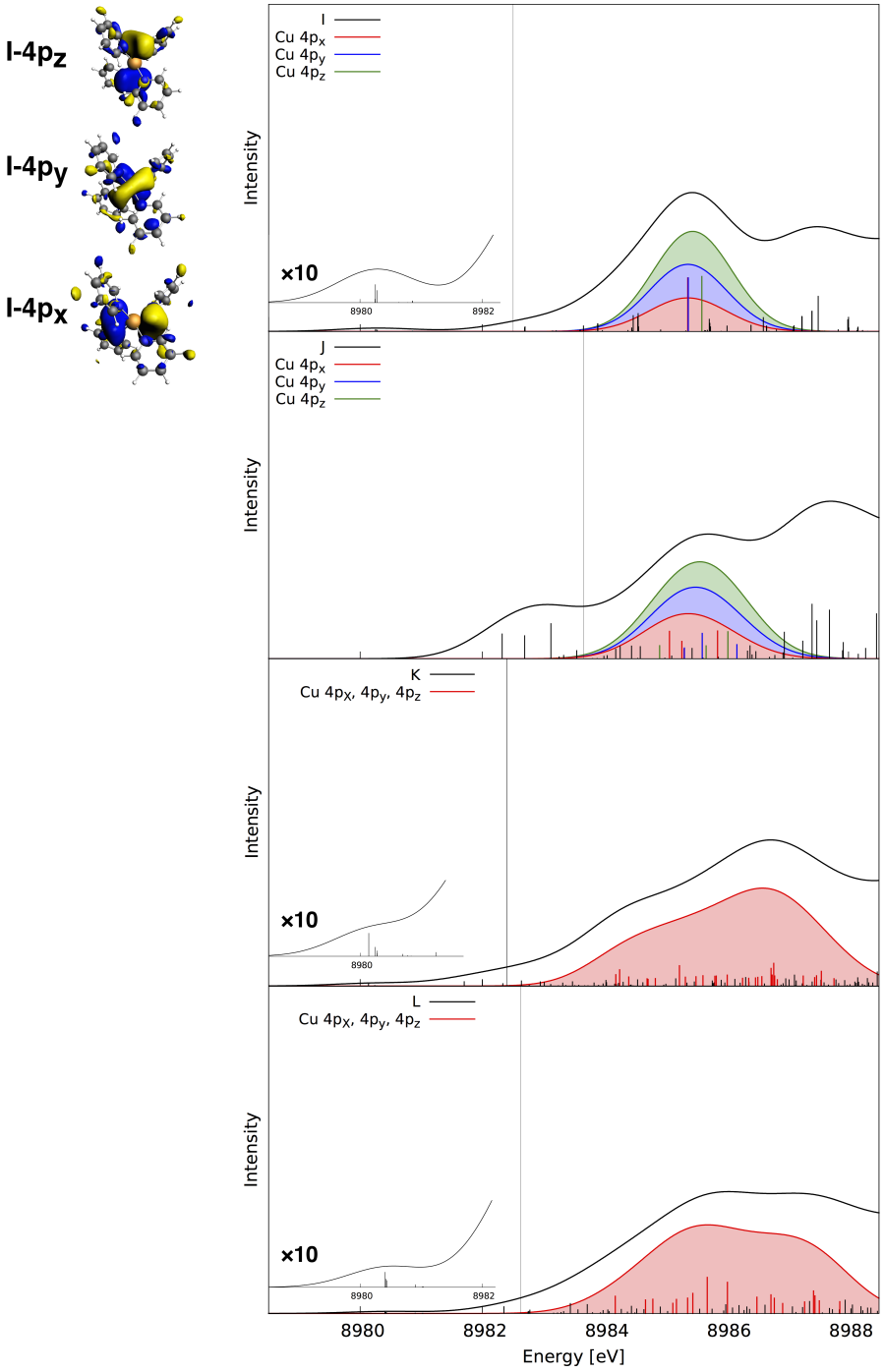

Figure 5.12: Molecular orbital analysis of the main contributions to the pre-edge regions in the calculated Cu K-edge XAS spectra (BP86/QZ4P) of the Cu(I) complexes **I** - **L** with coordination number four. Vertical bars indicate the individual transitions contributing to the calculated XAS spectra. The unoccupied orbitals responsible for the most relevant transitions are shown on the left, and the contributions of these transitions are highlighted in the calculated spectra shown on the right.

ligand mixing plus Cu *d*-*p* mixing).

5.3.4 MO analysis of the calculated XAS spectra for copper(II) complexes

For the Cu(II) complexes **M**-**Q**, the calculated pre-edge XAS spectra are shown in Fig. 5.6d. As expected, for all Cu(II) complexes, a typical weak pre-edge peak appears at ca. 8979.5-8981 eV, which can be assigned to transitions into the singly unoccupied Cu 3*d* orbital. The remaining pre-edge transitions appear above 8984-8985 eV and can, as for the Cu(I) complexes, be assigned to transitions into unoccupied Cu 4*p* orbitals. The calculated spectra of **M**-**Q** are compared in Fig. 5.13, which also includes an analysis of the main contributions (Cu 3*d* vs. Cu 4*p*) to the individual transitions.

In all five cases, the weak pre-edge peak at ca. 8979.5-8981 eV is due to the transition into a singly unoccupied orbital. Isosurface plots of this orbital are included in Fig. 5.13. It can be clearly seen that these orbitals are a combination of a Cu 3*d* orbital with ligand orbitals. The comparison of this peak for the different Cu(II) complexes shows that its intensity varies. The most intense $1s \rightarrow 3d$ pre-edge peak is found for **O**, in which the Cu center is has a coordination number of four and features pseudo-tetrahedral coordination geometry, while weaker $1s \rightarrow 3d$ pre-edge peaks are found for the remaining Cu(II) complexes.

Table I: Calculated intensities (BP86/QZ4P), expressed as dimensionless oscillator strengths, for the weak $1s \rightarrow 3d$ pre-edge peak at ca. 8979.5-8981 eV of the Cu(II) complexes **M** - **Q**. The total intensity is decomposed into dipole and second-order (quadrupole) contributions. For each complex, the coordination geometry and local symmetry of the Cu center are also indicated.

		dipole intensity	quadrupole intensity	total intensity	% dipole
M	square-planar (D_{4h})	$9.2 \cdot 10^{-12}$	$3.7 \cdot 10^{-6}$	$3.7 \cdot 10^{-6}$	0 %
N	distorted octahedral (C_{4h})	$1.1 \cdot 10^{-7}$	$3.8 \cdot 10^{-6}$	$3.9 \cdot 10^{-6}$	3 %
O	pseudo-tetrahedral (D_{2d})	$1.1 \cdot 10^{-5}$	$2.9 \cdot 10^{-6}$	$1.4 \cdot 10^{-5}$	79 %
P	distorted square-planar (D_{2d})	$5.0 \cdot 10^{-7}$	$2.3 \cdot 10^{-6}$	$2.8 \cdot 10^{-6}$	18 %
Q	distorted octahedral (D_{2d})	$2.8 \cdot 10^{-7}$	$2.4 \cdot 10^{-6}$	$2.7 \cdot 10^{-6}$	10 %

Table I lists the intensities calculated for this transition decomposed into dipole and second-order (quadrupole) contributions. For all five complexes, this transitions have a very similar small quadrupole intensity of ca. $2\text{-}4 \cdot 10^{-6}$. The differences in the total intensity of the $1s \rightarrow 3d$ pre-edge peak are mainly due to the variations in the dipole intensity. This dipole intensity is caused by the (small) admixture of Cu 4*p* contributions into the singly unoccupied Cu 3*d* orbital (cf. Fig. 5.10d). These differences in the dipole intensity can be directly related to the coordination geometry and the local symmetry at the Cu center.[145]

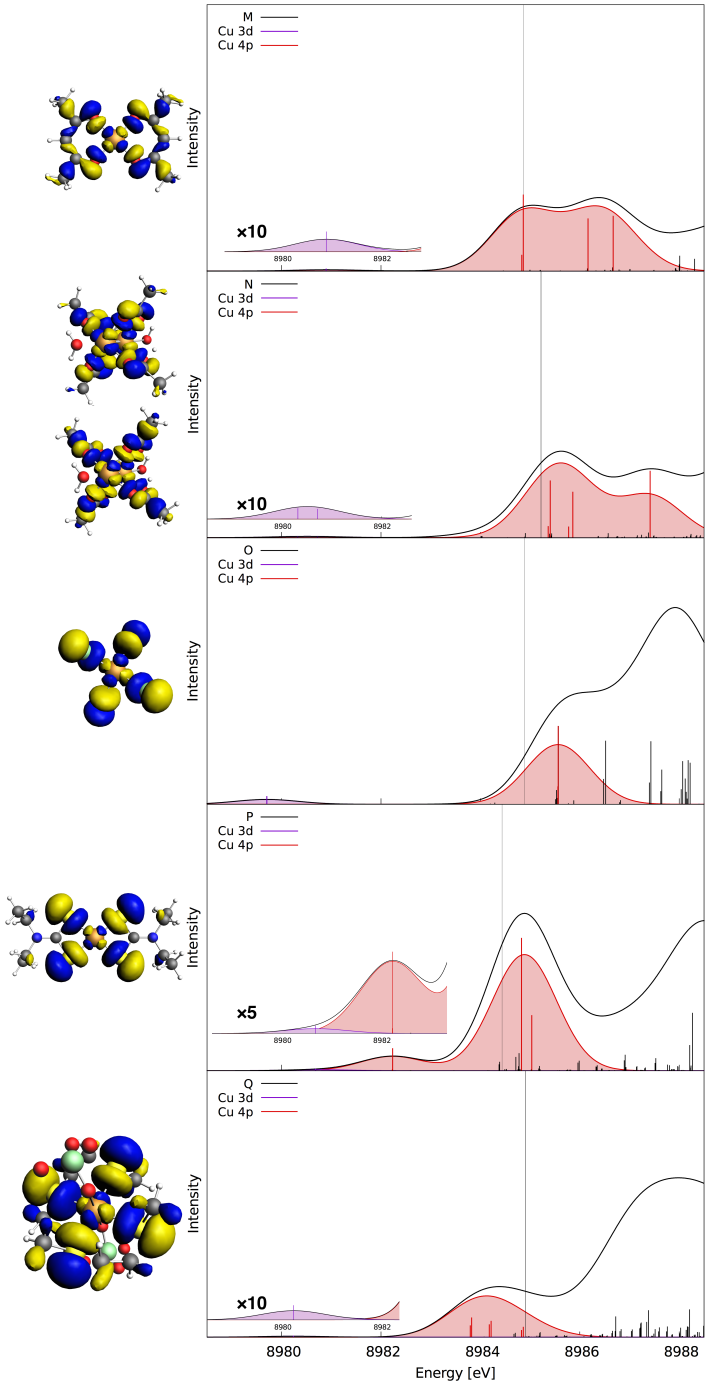

Figure 5.13: Molecular orbital analysis of the main contributions to the pre-edge regions in the calculated Cu K-edge XAS spectra (BP86/QZ4P) of the Cu(II) complexes **M** - **Q**. Vertical bars indicate the individual transitions contributing to the calculated XAS spectra. The unoccupied orbitals responsible for the weak pre-edge peak are shown on the left, and the contributions of transitions into unoccupied orbitals dominated by Cu 3*d* and Cu 4*p* orbitals, respectively, are highlighted in the calculated spectra shown on the right.

For **M** with a square-planar coordination geometry (local D_{4h} symmetry), *p*-*d* mixing is not possible since the Cu *d* and *p* orbitals belong to different irreducible representations (a_{2u} as well as e_u for the *p* orbitals and a_{1g}, b_{1g}, b_{2g}, and e_g for the *d* orbitals, respectively). This is also the case for an axially distorted octahedral coordination geometry. The two Cu centers in **N** feature such a coordination geometry. However, as the two axial ligands differ, the local D_{4h} symmetry is slightly distorted towards C_{4h}, which allows for the admixture of a small *p* contribution into the singly unoccupied Cu 3*d* orbital. Therefore, the dipole intensity increases, but only amounts to ca. 3% of the total intensity, i.e., the total $1s \rightarrow 3d$ pre-edge peak intensity is still determined by the quadrupole contribution.

In **P** and **Q**, the Cu centers are in distorted square-planar and a distorted octahedral coordination geometry, respectively, and in both cases the local symmetry is thus lowered to D_{2d}. This allows for the mixing of Cu 3*d* and 4*p* orbitals, which now both belong to the b_2 and e irreducible representation. Consequently, the $1s \rightarrow 3d$ pre-edge peak in **P** acquires 18 % dipole intensity and in **Q** it gains 10 % dipole intensity. Still, for both complexes the total intensity of this pre-edge peak is determined by the quadrupole contribution, which is slightly lower than for **M** and **N**. With an increased distortion towards a tetrahedral coordination environment in **O**, the *p*-*d* mixing is increased and the dipole intensity further increases, now amounting to 79 % of the total intensity. The is reflected in an increase of the total intensity of the $1s \rightarrow 3d$ pre-edge peak by a factor of five compared to the other Cu(II) complexes.

Except for the weak pre-edge peak discussed so far, the remaining features in the calculated XAS spectra of the Cu(II) complexes **M** - **Q** are due to transitions into Cu 4*p* orbitals (cf. Fig. 5.13). For the Cu(II) complexes **M**, **N**, **O**, and **P**, this intense pre-edge transition appears at ca. 8985-8986 eV and its intensity is comparable to the one of the corresponding pre-edge transitions in the four-coordinated Cu(I) complexes. This is in agreement with the experimental spectra of Ref. [126], in which the first pre-edge peak is found at ca. 8986 eV. For **M** and **N**, this peak is broadened via symmetric mixing with unoccupied ligand orbitals (cf. Fig. 5.10a). For the (distorted) square-planar complexes **M** and **P**, the calculated spectra show the first intense peak at a slightly lower energy (ca. 8985 eV), and for **P** its intensity is increase compared to the other complexes. This is consistent with the ligand-field picture discussed in Sec. 5.3.1, as the unoccupied lone-pair 4*p* orbital perpendicular to the ligand plane will provide a higher intensity.

Furthermore, for complex **P**, the non-symmetric mixing of the low-lying unoccupied orbitals of the sulfur with the Cu 4*p* orbitals (cf. Fig. 5.10b) introduces a MLCT transition at ca. 8982 eV. Such MLCT transitions, are most likely responsible for the low-intensity tails in the region between 8983 eV and 8985 eV observed in the K-edge XAS spectra of Cu(II) complexes reported in Ref. [126], even though individual MLCT transitions were not resolved in these experimental spectra. Such an assignment explains the increased intensity of the tail in this region found for the Cu(II) complexes that were classified as covalent, in which the ligands generally have lower-lying unoccupied orbitals. For **Q**, the first intense pre-edge peak is shifted to a lower

energy and appears at ca. 8984 eV, which is in agreement with Ref. [126] that shows this peak at 8984 eV for **Q**, ca. 1-2 eV lower than for the Cu(II) complexes with ligands coordinating via oxygen atoms.

Altogether, all features of the experimental Cu(II) pre-edge spectra that are identified and discussed in Ref. [126] (i.e., the intensity of the weak $1s \rightarrow 3d$ pre-edge peak, the intensity of the tails between 8983 eV and 8985 eV, and the dependence of the position of the first intense pre-edge peak on the type of ligand) are correctly reproduced by the calculations for complexes **M** - **Q**. The first intense pre-edge peaks in the K-edge XAS spectra of Cu(I) complexes have previously assigned to shake-down transitions.[126] Such an assignment can also explain the shift of the position of this peak when comparing ionic and covalent complexes as well as ligands coordinating via oxygen and sulfur.[131] The description of such shake-down transitions is not possible with TD-DFT, which lacks the ability to account for double excitations. However, Wieghardt and co-workers[127] recently found in an experimental and computational study of Cu(II):η^2-L complexes that the position of the first intense pre-edge position is correctly described by TD-DFT calculations, calling the assignment to shake-down transitions into question. Thus, future computational studies using quantum-chemical methods[146,147] that can account for shake-down transitions will be required for a definite assignment.

5.4 Conclusions

The results of the calculations presented here provide a comprehensive picture of the dependence of Cu K-edge XAS spectra on oxidation state and coordination geometry. First, Cu(II) complexes show a characteristic weak pre-edge peak that is due to the (dipole-forbidden) transition into the singly occupied Cu $3d$ orbital. Its intensity is determined by the admixture of p-orbital contributions. Therefore, it is sensitive to the local symmetry at the Cu center and increases when going from a square-planar to a pseudo-tetrahedral coordination geometry.[145]

Second, the calculations for Cu amine model complexes and for the test set of 17 Cu(I) and Cu(II) complexes are in agreement with the earlier experimental assignments of Solomon and coworkers.[126] Linear Cu(I) complexes show a characteristic intense pre-edge peak at ca. 8982 - 8984 eV. For Cu(I) complexes with a coordination number of three the intensity of this peak decreases. For complexes with a coordination number of four, the intensity of this pre-edge peak is equal (respect to CN=3) but its position shifts to higher energies. The MO analysis of the underlying transitions is in overall agreement with a simple ligand-field picture.[126,131] The calculations for Cu amine model complexes as well as the MO analysis indicate that the same characteristic pre-edge features will also be present for Cu(II) complexes. However, since experimentally accessible Cu(II) complexes usually have a coordination number of four, this prediction awaits confirmation by further calculations and experimental studies.

These characteristic pre-edge features of different coordination environments are preserved across the test set of complexes featuring a diverse set of different ligands. However, additional variations in the pre-edge spectra were found that are caused by the interaction of the Cu orbitals with unoccupied ligand orbitals. Three different mechanisms, which are summarized in Fig. 5.10a-c, have been identified. First, a symmetric mixing of Cu 4*p* and unoccupied ligand orbitals can lead to a splitting and broadening of the characteristic pre-edge features. Second, a non-symmetric mixing of Cu 4*p* and low-lying unoccupied ligand orbitals results in weak MLCT peaks below 8983 eV. Third, such weak pre-edge peaks can also arise from the mixing of Cu 3*d* and low-lying unoccupied ligand orbitals.

The additional pre-edge features arising from these three mechanisms can provide detailed insights into the identity and the electronic structure of the ligands. MLCT peaks have recently been observed in experimental Cu K-edge XAS spectra.[13,127] HERFD methods offer the possibility to resolve these weak peaks and thus have the potential to confirm the predictions made in this work and to make use of the additional electronic structure information encoded in Cu K-edge XAS spectra.

Altogether, the results presented here will allow for the reliable analysis and assignment of experimental Cu K-edge XAS spectra. Therefore, they provide a valuable tool for the investigation catalytic reaction mechanisms (e.g., of SCR in exhaust gas catalysis) by revealing oxidation state and coordination environment of Cu centers.

Chapter 6

Application XES: Structural sensitivity of X-ray emission spectra

A methodology for analyzing the dependence of molecular spectra calculated with quantum-chemical methods on the underlying molecular structure is presented. This analysis is applied to investigate the structural sensitivity of calculated valence-to-core X-ray emission (VtC-XES) spectra for the test case of three iron carbonyl complexes, $Fe(CO)_5$, $[FeCp(CO)_2(THF)]^+$ (Cp = cyclopentadienyl, THF = tetrahydrofuran), and $Fe(CO)_3$(cod) (cod = cyclooctadienyl). Based on this analysis, discussing how the VtC-XES spectra depend on changes of metal-ligand bond distances and bond angles as well as on the structure of the ligands. The benefits of such an analysis of the structural sensitivity are discussed. This methodology can serve as a first step towards quantifying and accounting for uncertainties due to the underlying model structure in theoretical spectroscopy.

The publication [148] is based on this chapter of this thesis.

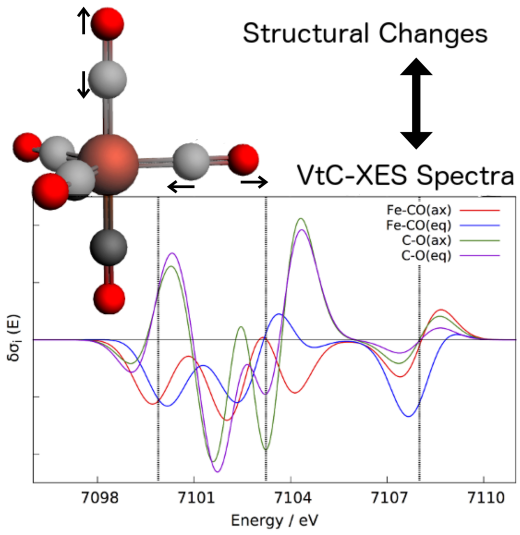

Figure 6.1: Schematic overview, which represents this chapter in one picture. One of the three examined test iron carbonyl complexes, ironpentacarbonyl, is shown with some indicated bond length displacements. To illustrate the effect of molecular structures on VtC-XES spectra, these spectra are shown as difference spectra for different bond length elongations.

6.1 Introduction

As already mentioned in Sec. 3.2, many important spectroscopic techniques such as vibrational spectroscopy, UV/Vis spectroscopy, or X-ray absorption and emission spectroscopy, only provide indirect access to structural information. In this case, spectroscopic experiments are often combined with quantum-chemical calculations[63] in order to connect them to specific features of the underlying molecular structure.

For X-ray spectroscopy, quantum-chemical calculations can provide an assignment of the peaks in X-ray emission and absorption spectra to occupied and unoccupied electronic states, and can connect those to the structure of the ligand environment in transition-metal complexes (see, e.g., Refs. [16, 67–69]).

In this chapter the focus is on valence-to-core (VtC) X-ray emission spectroscopy (XES).[84,90] In combination with quantum-chemical calculations, VtC-XES can be used to obtain partial structural information, in particular in the vicinity of transition metal centers. VtC-XES makes it possible to identify which ligands are coordinated to a transition metal center, for instance in molecular transition metal complexes,[15–18] for catalytic metal centers in zeolites,[22,23] and for metal clusters in enzymes.[19–21] The ability of VtC-XES spectroscopy to unravel further structural details, such as coordination number or bond angles, as well as insights into the electronic structure has also been explored.[16,18,91,92]

Quantum-chemical calculations of molecular spectra, including VtC-XES spectra, always require an atomistic structure as starting point. This structure is usually obtained by searching for a local minimum on the potential energy surface. For this single, fixed structure one can then predict the corresponding spectrum. However, in general one is interested in the *inverse problem*:[149–151] Given a measured experimental spectrum, one seeks to determine the underlying molecular structure, or at least to obtain some partial structural information.

Conventionally, this is achieved by calculating spectra for likely structures constructed with chemical knowledge and then confirming (or disproving) this structure by comparing the calculated and the experimental spectrum. More generally, different possible structures can be constructed (manually or using computational tools) in order to identify the structure for which the best match between calculated and experimental spectrum is obtained. However, quantum-chemical calculations for all but the smallest molecular systems will always be subject to inaccuracies introduced by the choice of the employed quantum-chemical method [e.g., the approximate exchange-correlation functional used in density-functional theory (DFT)] as well as the construction of the (model) structures.

Therefore, the agreement between calculated and experimental spectra will never be perfect. Instead, it becomes necessary quantify this uncertainty[152] in order to judge whether an assignment is reliable or whether it is expected to be highly sensitive to the unavoidable inaccuracies in the quantum-chemical calculations. Methods for including error estimates due to the inaccuracies of the exchange-correlation functional in the calculation of catalytic reaction energies with DFT have recently been proposed.[153–156] For extending such approaches to theoretical spectroscopy, it becomes necessary to consider not only the sensitivity with respect to the exchange-correlation functional, but also the sensitivity with respect to changes in the model structures that are used. This will also be a prerequisite for a structural refinement based on quantum-chemical calculations of molecular spectra.

The sensitivity of simulated EXAFS spectra, for instance of photosystem II and of corresponding model complexes, to the underlying molecular structure has been investigated systematically,[157–159] and a methods for an automatic structural refinement based on a combination of simulated EXAFS spectra and quantum-chemical geometry optimizations have been developed.[160,161] However, in the quantum-chemical calculation of molecular spectra the structural sensitivity is usually not assessed systematically, or is only considered by comparing the calculated spectra for a few distinct model structures (see, e.g., Ref. [162] for NMR spectroscopy, Refs. [163, 164] for vibrational spectroscopy, or Refs. [165, 166] for X-ray photoelectron spectroscopy).

Here, as a step towards systematically quantifying and accounting for uncertainties in theoretical spectroscopy, this sensitivity on the underlying structure for the quantum-chemical calculation of molecular spectra were systematically investigate. The aim is to identify which structural

changes affect which parts of the spectrum and which ones leave certain parts of the spectrum unaffected. To answer these questions not only qualitatively but in a quantitative fashion, the structural sensitivity $\delta\sigma_i(E)$ for the structural change R_i were define as

$$\delta\sigma_i(E) = \frac{\mathrm{d}\sigma(E)}{\mathrm{d}R_i}, \tag{6.1}$$

where $\sigma(E)$ is the spectral intensity (i.e., the calculated intensity as a continuous function of the excitation or emission energy E, which is usually obtained by applying an appropriate broadening to the discrete transitions obtained in quantum-chemical calculations) and R_i is a suitable Cartesian or internal nuclear coordinate describing the relevant structural change.

To explore the usefulness of such an analysis, we will consider the VtC-XES spectroscopy of a test set of three iron carbonyl complexes[16] as an example. VtC-XES spectroscopy is ideal for focussing on the structural sensitivity, because its sensitivity to the choice of exchange-correlation functional has been shown to be small[91] for the simple yet reliable ΔDFT method[115] that will be used here.

This work is organized as follows. Sec. 6.2 presents the considered test set of iron-carbonyl complexes (Sec. 6.2.1), the methodology employed for the calculation of VtC-XES spectra (Sec. 6.2.2), and introduces the analysis of the structural sensitivity of computed VtC-XES spectra (Sec. 6.2.3). This is followed by results of such an analysis for three prototypical iron carbonyl complexes in Sec. 6.3, illustrating the structural sensitivity with respect to bond distances in $Fe(CO)_5$ (Sec. 6.3.2), sensitivity differences with respect to metal-ligand distances and angles in $[FeCp(CO)_2(THF)]^+$ (Sec. 6.3.3), and the structural sensitivity with respect to the ligand environment as well as ligand structure in $Fe(CO)_3$(cod) (Sec. 6.3.4). Finally, a summary and concluding remarks are given in Sec. 6.4.

6.2 Computational Methodology

6.2.1 Test set of iron-carbonyl complexes

As a first target for exploring the structural sensitivity of calculated VtC-XES spectra, a test set of three closed-shell iron-carbonyl complexes, ironpentacarbonyl, $Fe(CO)_5$, $[FeCp(CO)_2(THF)]^+$ (Cp = cyclopentadienyl, C_5H_5, THF = tetrahydrofuran, C_4H_8O), and $Fe(CO)_3$(cod) (cod = cyclooctadienyl, C_8H_{12} have been chosen. These Iron carbonyls have been chosen as prototypical metal complexes, for which high-quality experimental data as well as previous quantum-chemical calculations are available.[16,69] A detailed comparison of the experimental and calculated VtC-XES spectra of these complexes as been presented previously.[16]

The molecular structures of these complexes have been optimized using DFT as implemented in

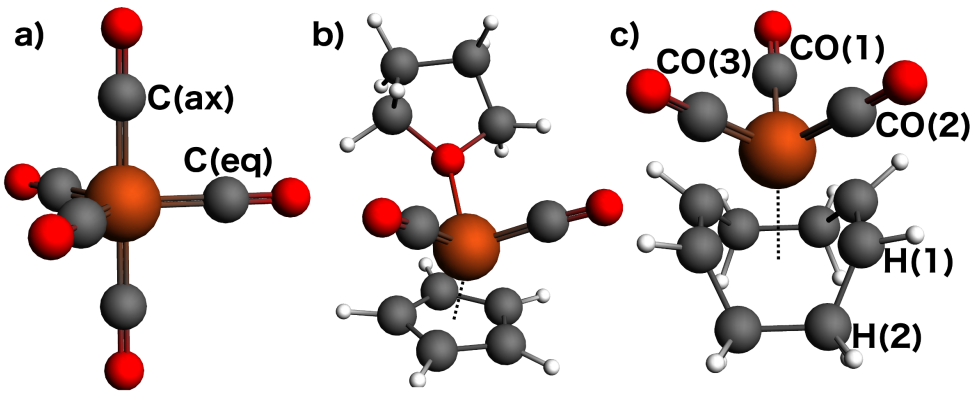

Figure 6.2: Molecular structures of the iron carbonyl model complexes investigated here. (a) $Fe(CO)_5$, (b) $[FeCp(CO)_2(THF)]^+$ (Cp = cyclopentadienyl, C_5H_5, THF = tetrahydrofuran, C_4H_8O), (c) $Fe(CO)_3(cod)$ (cod=cyclooctadienyl, C_8H_{12}).

the Amsterdam density functional (ADF) program package,[132,133] employing the BP86 exchange-correlation functional[98,99] and the Slater-type TZ2P basis set.[134] The resulting structures are shown in Fig. 6.2.

6.2.2 Calculation of VtC-XES spectra

For these optimized structures, VtC-XES spectra are calculated using the simple ΔDFT approach of Lee et al.[115] as implemented in ADF (Sec. 4.3).

If not stated otherwise, the BP86 exchange-correlation functional, the Slater-type QZ4P basis set[134] have been used for the calculation of VtC-XES spectra, and a constant shift of 180.62 eV has been applied.[69] For comparison, VtC-XES spectra calculated using the B3LYP[135] exchange-correlation functional are included in Sec. 6.3.1. In this case, a constant shift of 147.82 eV has been applied. These constant shifts have been chosen such that peak A is aligned with the corresponding peak in the experimental spectrum of Ref..[16] In all calculations of VtC-XES spectra, the COSMO solvation model[114] with default parameters has been used to include a first approximation of environment effects. All calculations are performed using non-relativistic DFT because it has been found previously that the inclusion of relativistic effects only reduces the constant shift ΔE_{shift}, but leaves the overall VtC-XES spectra unaffected.[91]

The calculated VtC-XES spectra are then plotted by applying a Gaussian line broadening with a full-width at half maximum (FWHM) of 1.5 eV, i.e., the spectral intensity as a function of the emission energy is given by

$$\sigma(E) = \sum_n f_n G(E_n - E), \tag{6.2}$$

where $G(E)$ is a normalized Gaussian line-shape function with a FWHM of 1.5 eV, and where the sum runs over all transitions in the relevant energy range.

6.2.3 Analysis of the structural sensitivity

The calculated spectral intensity $\sigma(E) = \sigma(E, \boldsymbol{R})$ is, in fact, a function of the underlying molecular structure, defined by the nuclear coordinates $\boldsymbol{R}$. Usually, only the spectra calculated for a single, fixed minimum structure $\boldsymbol{R}_0$ are considered.

To quantitatively analyze the structural sensitivity of the calculated VtC-XES spectra, selected distortions along internal coordinates R_i were chosen, in particular bond distances and angles. Of course, other coordinates, such as Cartesian coordinates or normal mode coordinates could also be employed. The structural sensitivity with respect to coordinate R_i is then defined by Eq. (6.1) as derivative of the spectral intensity. Here, this structural sensitivity is calculated by numerical differentiation as a difference spectrum,

$$\delta\sigma_i(E) = \frac{\mathrm{d}\sigma(E)}{\mathrm{d}R_i} \approx \frac{\sigma(E, \boldsymbol{R}_0 + \Delta R_i) - \sigma(E, \boldsymbol{R}_0)}{\Delta R_i}, \tag{6.3}$$

where ΔR_i is a small displacement along the internal coordinate R_i and $\sigma(E, \boldsymbol{R}_0 + \Delta R_i)$ is the spectral intensity calculated for the displaced molecular structure. Here, the magnitude of the displacement ΔR_i serves as a normalization of the difference spectrum. The dependence on the magnitude of the displacement will be discussed in Sec. 6.3.1 below. If not stated otherwise, $|\Delta R_i| = 1$ pm for bond distances and $|\Delta R_i| = 1°$ for bond angles have been used. Here, a non-symmetric difference quotient for the numerical differentiation were used instead of a symmetric one, which would require twice the number of calculations of the VtC-XES spectra.

Of course, the analytical calculation of $\delta\sigma_i(E)$ could be derived and implemented in a straightforward way. It would, however, require the solution of coupled-perturbed Kohn-Sham equations for each displacement because the orbital energies as well as the transition moments are not stationary with respect to molecular orbital coefficients. Thus, the computational effort for calculating the structural sensitivity $\delta\sigma_i(E)$ of VtC-XES spectra within the simple ΔDFT approach of Lee et al.[115] for all $3N$ Cartesian displacements will be comparable to the analytical calculation of the molecular Hessian.

Finally, it was noted that derivatives of spectral parameters, analogous to those needed here, are also required for calculating vibrational corrections to molecular properties,[167] such as vibrational corrections to nuclear magnetic resonance (NMR) parameters[168] or to hyperfine coupling constants in electron paramagnetic resonance (EPR) spectroscopy.[169,170] So far, these derivatives have usually been calculated numerically, but with the advent of open-ended high-order response theory the analytical calculation of such vibrational corrections becomes possible.[171]

6.3 Results and Discussion

6.3.1 $FeCO_5$: Assessment and illustration of sensitivity analysis

To illustrate the analysis method introduced above for a simple test case, ironpentacarbonyl $Fe(CO)_5$ (see Fig. 6.2a) was chosen, in which the bond distance between the central iron atom and one of the axial CO ligands was elongated while keeping the C-O bond length as well as the bond distance between the iron atom and all other ligands fixed. This first test case will also be used to verify the choice of technical details, such as the displacement used for the numerical differentiation of the spectral intensity, and to assess the dependence of $\delta\sigma_i(E)$ on the choice of the exchange-correlation functional.

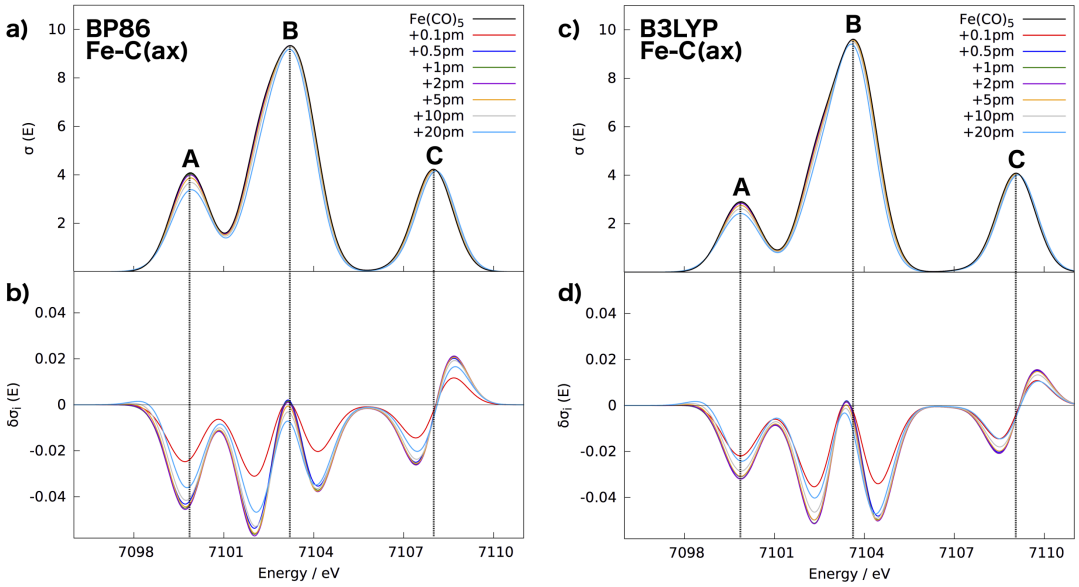

Figure 6.3: Calculated VtC-XES spectrum of $Fe(CO)_5$ for the equilibrium structure as well as distorted structures in which one of the axial the Fe-CO bond distances has been increased by different displacements (top) as well as structural sensitivity $\delta\sigma_i(E)$ calculated as normalized difference spectra for these different displacements (bottom). The left part shows spectra calculated with BP86/QZ4P while the right part shows spectra calculated with B3LYP/QZ4P.

Fig. 6.3a (top left panel) shows the calculated VtC-XES spectrum (BP86/QZ4P) of the equilibrium structure (see also Ref. [16]) together with those calculated for structures in which the axial Fe-CO bond distances has been increased by 0.1 pm to 20 pm. For bond lengths increases up to 2 pm, the changes in the spectrum are hardly noticable, but for 5 pm, 10 pm, and 20 pm the effects become clearly visible. For the first peak (peak A) at ca. 7100 eV, the intensity decreases as the bond distance increases, while the position of the peak remains unchanged. For the second peak (peak B), the position and intensity of the maximum are not affected, but a

subtle decrease of the shoulder at ca. 7103 eV has been noticed. Finally, for the third peak (peak C) at ca. 7108 eV there is a small shift to lower emission energies as the bond distance is increased.

The structural sensitivity $\delta\sigma_i(E)$, calculated as normalized difference spectra, corresponding to these bond length elongations for one of the axial Fe-CO bonds, is shown in Fig. 6.3b (bottom left panel). Because of the normalization, qualitatively similar difference spectra are obtained for all displacements. For the smallest bond length increase of 0.1 pm, it appears that the difference spectrum is affected by numerical errors, while for a bond length increase of 20 pm the change of the spectrum starts to behave nonlinearly with respect to the displacement. However, for displacements of 0.5 pm up to 10 pm the normalized difference spectra are almost identical. Thus, a displacement of 1 pm for bond distances (and in analogy, of 1° for angles) was chosen to calculate $\delta\sigma_i(E)$ throughout this work.

At this point, it is instructive to consider how certain changes in the full calculated spectra (as observed in Fig 6.3a) are reflected in the structural sensitivity (shown in Fig. 6.3b) and *vice versa*. For peak A in the full VtC-XES spectrum, the decrease of the intensity with increasing bond distance is reflected by a negative peak in the structural sensitivity $\delta\sigma_i(E)$ that appears at the same position as the peak maximum in the full spectrum. For peak B, $\delta\sigma_i(E)$ vanishes at the maximum of the peak, but there are negative peaks in $\delta\sigma_i(E)$ at ca. 7102 eV and ca. 7104 eV, which correspond to a decrease of the shoulders of the second peak in the full spectrum. While such a decrease can be identified in Fig 6.3a for the low-energy shoulder, the decrease of the high-energy shoulder is more subtle and can only be clearly recognized in the difference spectrum. For peak C the shift of the maximum to lower emission energies shows up as a combination of a positive and a negative peak in $\delta\sigma_i(E)$ to the left and right of the peak maximum in the full spectrum, respectively.

Finally, Figs. 6.3c and d (right panels) show the corresponding calculated spectra for the equilibrium structure as well as displaced structures and the structural sensitivity $\delta\sigma_i$ obtained with B3LYP/QZ4P. Comparing those to the spectra and structural sensitivity obtained with BP86/QZ4P (upper panels), it can be confirmed that the dependence of the calculated VtC-XES spectrum on the choice of the functional is negligible. For the structural sensitivity, only small differences in the size of some of the features are found, but overall the structural sensitivity shows an identical picture for both BP86 and B3LYP.

6.3.2 $FeCO_5$: Sensitivity with respect to bond distances

As a first application of analyzing the structural sensitivity of VtC-XES spectra, the effect of modifying four different bond distances in $FeCO_5$ were compared: The axial and the equatorial Fe-CO bond distances as well as the C-O bond distances within the axial and equatorial carbonyl

ligands. The structural sensitivity $\delta\sigma_i(E)$ with respect to individually elongating these four bond distances is shown in Fig. 6.4. Here, each of the normalized difference spectra, calculated as described above, corresponds to an elongation of one of the respective bond distances (i.e., the Fe-CO or C-O bond distances of a single carbonyl ligand) while keeping all other bond distances fixed. The effect of changing the axial Fe-CO bond distance has already been discussed in the

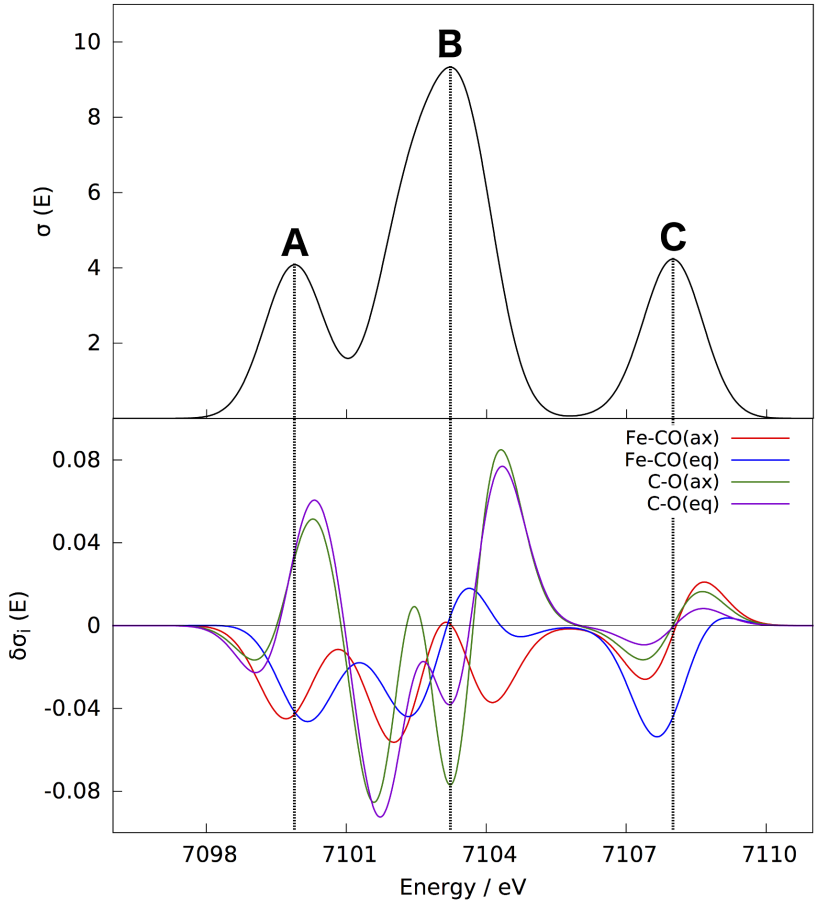

Figure 6.4: Calculated VtC-XES spectrum (BP86/QZ4P) of $FeCO_5$ (top, black) and structural sensitivity $\delta\sigma_i(E)$ (bottom) with respect to increasing the axial and equatorial Fe-CO bond distances, Fe-CO(ax) (red) and Fe-CO(eq) (blue), as well as the C-O bond distances within the axial and equatorial carbonyl ligands, C-O(ax) (green) and C-O(eq) (purple).

previous section. When elongating the equatorial Fe-CO bond distance, peak A responds in a similar fashion and shows a decreasing intensity when increasing the bond distance, while the second and the third peak respond differently to an increase of the axial and the equatorial Fe-CO bond distances. For peak B, a combination of a negative and a positive peak in $\delta\sigma_i(E)$ were observed, which corresponds to a shift of the second peak to higher energies when elongating the equatorial Fe-CO bond distance. For peak B, the negative peak in $\delta\sigma_i(E)$ indicates a decrease in intensity when elongating the equatorial bond Fe-CO distance. The latter effect is significantly

more pronounced than the shift in the peak position found for the axial ligand.

Changing the C-O bond distance within the carbonyl ligands induces a qualitatively similar response in the VtC-XES spectra for the axial and equatorial carbonyl groups, but this response is very different from the one observed when changing the Fe-CO bond distances. For peak A, the intensity increases when elongating a C-O bond, as opposed to a decrease for elongations of the Fe-CO bonds. For peak B, increasing the C-O bond distance results in a pronounced decrease of the low-energy shoulder at ca. 7101.5 eV and a shift of the high-energy shoulder at ca. 7103.5 eV to higher energies. Finally, an elongation of the C-O bond distances leads to a rather small shift of peak C to higher energies.

Overall, changes in the axial and equatorial Fe-CO bond distance and in the C-O bond distances have a distinctly different effect on the VtC-XES spectra that can be revealed by this analysis. To some extent, these effects are in line with an analysis of the orbital contributions to the different peaks: As was shown in Ref. [16] peaks A and B are dominated by contributions arising from carbonyl orbitals, while peak C is mainly due to iron 3*d*-orbitals. Consequently, a change of the C-O bond distance within the carbonyl ligand has little effect on the third peak. However, the analysis of the structural sensitivity applied here is able to reveal not only which building blocks contribute to certain a peak, but can also distinguish a different response (increase or decrease in intensity, change in peak position) of individual peaks to different structural changes within one ligand.

6.3.3 $[FeCp(CO)_2(THF)]^+$: Sensitivity differences for different ligands

As a second example, a complex with three different types of ligands, $[FeCp(CO)_2(THF)]^+$ (see Fig. 6.2b) were considered. It features two carbonyl ligands, an η^5-coordinated cyclopentadienyl ligand and a tetrahydrofuran (THF) ligand coordinated via its oxygen atom. The aim is to identify how structural changes in this mixed ligand environment affect the VtC-XES spectra.

The calculated VtC-XES spectrum of $[FeCp(CO)_2(THF)]^+$ is shown in the upper part of Fig. 6.5. The different features of this spectrum and their assignment to orbitals of the iron center and the different ligands has been previously discussed in Ref. [16]. Compared to $Fe(CO)_5$, three peaks now appear in the region below 7097.5 eV, one very weak peak D at ca. 7087.5 eV, and two stronger peaks E and F at ca. 7091 eV and at ca. 7095.5 eV, respectively. These can be assigned to the Cp and the THF ligands. In the region above 7097.5 eV, the peaks A, B, and C observed for $Fe(CO)_5$ also appear for $[FeCp(CO)_2(THF)]^+$. However, peak B is shifted to higher energy by ca. 0.5 eV and its the shoulders have decreased, and peak C has become more intense compared to peak A and is now shifted to lower energies (ca. 7106.5 eV), while a pronounced shoulder appears at ca. 7108 eV. Again, the additional signal at ca. 7108 eV is assigned to the Cp and THF ligands in Ref. [16].

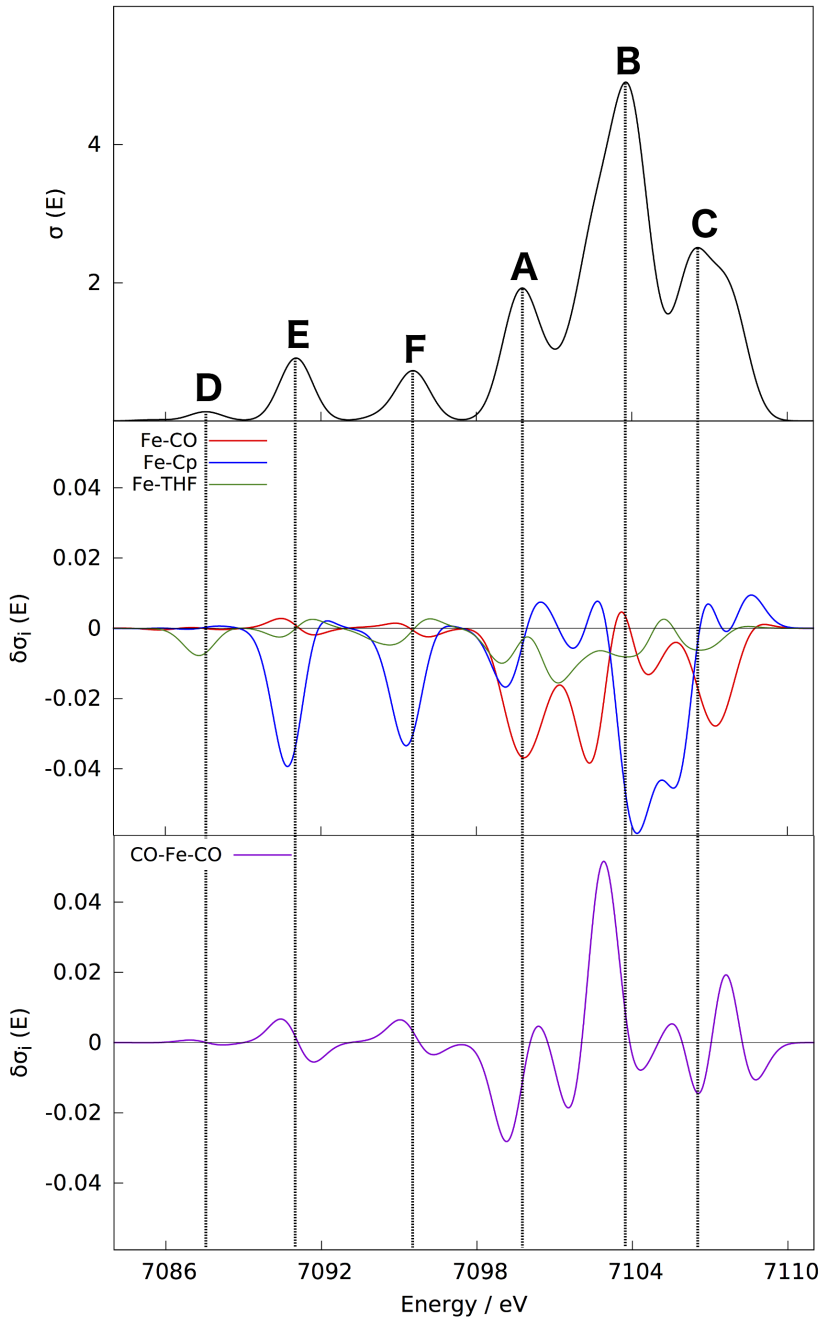

Figure 6.5: Calculated VtC-XES spectrum (BP86/QZ4P) of $[FeCp(CO)_2(THF)]^+$ (top, black) and structural sensitivity $\delta\sigma_i(E)$ with respect to increasing the Fe-CO (red), Fe-Cp (blue), and Fe-(THF) (green) bond distances (middle) as well as with respect to increasing the CO-Fe-CO bond angle (bottom, purple).

To investigate how the VtC-XES spectra respond to structural changes in the ligand environment, the middle part of Fig. 6.5 shows the structural sensitivity $\delta\sigma_i(E)$ for an elongation of the distances between the iron center and the three different types of ligands: the distance Fe-CO between the iron atom and one of the carbonyl ligands, the distance Fe-THF between the iron atom and the oxygen atom of the THF ligand, and the distance Fe-Cp between the iron and the center of the cyclopentadienyl ring. In all three cases, these iron-ligand distances are increased individually while keeping the structure of the ligand as well as the distances between the iron center and all other ligands fixed. Finally, the lower part of Fig. 6.5 shows the structural sensitivity with respect to an increase of the CO-Fe-CO angle, while keeping all bond distances fixed.

All four considered structural changes lead to a distinct response in the calculated VtC-XES spectra. An elongation of the Fe-CO bond distance leaves the region below 7097.5 eV (peaks D, E, and F) mostly unaffected, while decreasing the intensities of peak A, the shoulders of peak B, and the high-energy shoulder of peak C at ca. 7108 eV. This is in line with the response to elongations of the equatorial Fe-CO bond lengths in $Fe(CO)_5$. Increasing the CO-Fe-CO bond angle affects the same region, but shows a different pattern. While the intensity of peak A decreases (together with a shift to higher energies), the low-energy shoulder of peak B shows a pronounced increase and the intensity at the maximum of peak C decreases while its high-energy shoulder increases.

An elongation of the Fe-Cp distance affects both the region below and above 7097.5 eV, and the intensities of peaks E and F as well as peaks B and C decrease. This precisely matches the components of the VtC-XES spectrum that have been assigned to the Cp ligand in Ref. [16]. In addition, peak A shifts to higher energies, as indicated by the combination of a negative and positive signal to the left and right of the maximum of peak A, respectively, in $\delta\sigma_i(E)$. The overall smallest change in the calculated VtC-XES spectrum is found when increasing the Fe-THF distance. Most noticeable are a decrease in the intensity of the very weak peak D, of the low-energy part of peak A, and in between peaks A and B. Again, this matches the components of the spectrum that were assigned to the THF ligand in Ref. [16].

Overall, the analysis of the structural sensitivity can clearly distinguish the contributions of different ligands to the calculated VtC-XES spectra by inspecting the structural sensitivity with respect to changes in the metal-ligand distances. It could be obtained that certain peaks are left unaffected when changing the distance to specific ligands. For instance, peaks E and F are not affected by changes in the Fe-CO distance, while the very weak peak D only responds to changes in the Fe-THF distance. In addition, the analysis provides specific patterns for the response to the different metal-ligand distances and can distinguish different structural changes for the same ligands, as illustrated for the change of the Fe-CO bond distance and the CO-Fe-CO angle.

6.3.4 $Fe(CO)_3$(cod): Sensitivity to ligand structure

The third test case is $Fe(CO)_3$(cod) (see Fig. 6.2c), featuring three carbonyl ligands as well as an η^4-coordinated cyclooctadienyl ligand. This complex has a mirror plane perpendicular to the cyclooctadienyl ligand that includes the iron atom and one of the carbonyl ligands, CO(1). The other two carbonyl groups, CO(2) and CO(3) are symmetry equivalent. Its calculated VtC-XES spectrum is shown in the upper part of Fig. 6.6.

In the region below 7097.5 eV, this spectrum shows a broad weak feature D which has been assigned to the cyclooctadienyl ligand in Ref. [16]. Above 7097.5 eV the spectrum shows the three intense peaks A, B, and C that are also found for $Fe(CO)_5$ and $[FeCp(CO)_2(THF)]^+$. However, the maxima of peaks A is shift to lower energies by ca. 1 eV compared to the other two complexes. The maximum of peak B is found at ca. 7102.5 eV, i.e., ca. 0.5 eV lower in energy than for $FeCO_5$ and ca. 1 eV lower in energy than for $[FeCp(CO)_2(THF)]^+$. At the same time, the intensity of peak B be is decreased relative to peaks A and B. Finally, for peak C the same pattern is found as for $[FeCp(CO)_2(THF)]^+$, with a maximum at ca. 7106.5 eV and a pronounced shoulder at ca. 7108 eV.

First, the structural sensitivity of the VtC-XES spectra with respect to structural changes in the carbonyl ligand sphere (see middle part of Fig. 6.6) will be discussed. For elongations of the Fe-CO(1) and Fe-CO(2) bond distances, respectively, a rather similar $\delta\sigma_i(E)$ is obtained. In both cases, the response of the VtC-XES spectra is similar as for elongations of the Fe-CO bond length in $[FeCp(CO)_2(THF)]^+$ and for the equatorial Fe-CO bond length in $Fe(CO)_5$. Slight differences are only found for the different components of peak C. The structural sensitivity $\delta\sigma_i(E)$ with respect on an increase of the CO(2)-Fe-CO(3) angle shows a similar pattern as for the increase of the corresponding angle in $[FeCp(CO)_2(THF)]^+$ for peak A and B, while the sign of the response is reversed for peak C. When increasing the C-O bond length within the carbonyl ligands, the VtC-XES spectra respond similar as for an increase of the C-O bond length of the equatorial carbonyl ligand in $Fe(CO)_5$. Comparing $\delta\sigma_i(E)$ for the two different carbonyl bond distances, C-O(1) and C-O(2), only very minor differences are found. Finally, it is worth noting that all these structural changes within the carbonyl ligand sphere only affect peaks A, B, and C and leave the region below 7097.5 eV unmodified.

Now turning to the structural sensitivity with respect to the cyclooctadienyl ligand (see lower part of Fig. 6.6). Increasing the Fe-(cod) distance (defined as distance from the iron atom to the center of the cyclooctadienyl ligand, see Fig. 6.2c) leads to a decrease of the broad feature D found in the region below 7097.5 eV. For the region above 7097.5 eV, the patterns found in $\delta\sigma_i(E)$ correspond to shifts in the emission energy: Upon increasing the Fe-(cod) distance, peak A shifts to lower energy and the shoulder of peak C at ca. 7108 eV shifts to higher energies. In addition, further energy shifts can be identified in the shoulders of peak B. It is worth noting that the observed structural sensitivity with respect to the Fe-(cod) distance is in line with the assignment

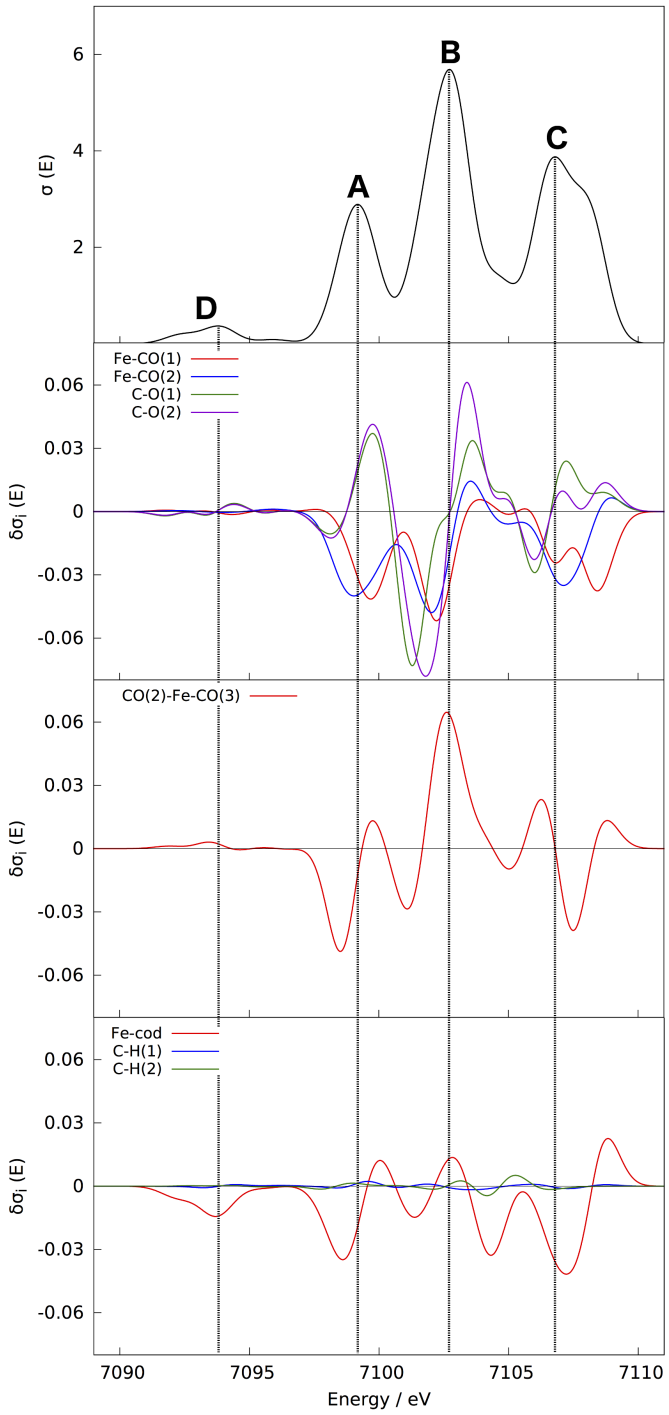

Figure 6.6: Calculated VtC-XES spectrum (BP86/QZ4P) of $Fe(CO)_3$(cod) (top, black) and structural sensitivity $\delta\sigma_i(E)$ for structural changes affecting the carbonyl ligands (middle) and the cyclooctadienyl ligand (bottom). The middle panels include $\delta\sigma_i(E)$ with respect to increasing the two Fe-CO bond distances, Fe-CO(1) (red) and Fe-CO(2) (blue), the two C-O bond distances, C-O(1) (green) and C-O(2) (purple), as well as the CO(2)-Fe-CO(3) angle (red). The bottom panel shows $\delta\sigma_i(E)$ with respect to increasing the Fe-cod distance (red) as well as two different C-H distances with the cyclooctadienyl ligand, C-H(1) (blue) and C-H(2) (green).

of Ref. [16], which identified contributions of the cyclooctadienyl ligands to all three peaks A, B, and C as well as the broad feature D. Finally, increasing different C-H bond distances within the cyclooctadienyl ligand only results in minor changes in the calculated VtC-XES spectrum, i.e., the spectrum is rather insensitive with respect to structural changes in the outer ligand sphere.

To summarize, different structural changes to the ligand environment in $Fe(CO)_3(cod)$ lead to distinct changes to the calculated VtC-XES spectra. To some extent, the patterns identified in $\delta\sigma_i(E)$ with respect to certain ligands are transferable between different complexes. For instance, changes in the Fe-CO and C-O bond distances and in CO-Fe-CO angles are similar across the investigated complexes, while different ligands, such as cyclopentadienyl, show patterns that were not present in other complexes. Further regions of the spectrum could be identified that are not affected by certain structural changes as well as structural changes that have only a negligible effect on the calculated VtC-XES spectra.

6.4 Conclusions

Theoretical spectroscopy is usually employed to calculate spectra for fixed molecular model structures, which can then be compared to experimental spectra. However, this common strategy ignores the sensitivity of the calculated spectra on the underlying model structure. In order to quantify and account for the uncertainty due to the underlying structural model, a novel analysis tool have been introduced. To this end, the structural sensitivity $\delta\sigma_i(E)$ have been defined as derivative of the calculated spectra with respect to defined structural changes, such as bond distances or bond angles. Here, this structural sensitivity is obtained as numerical derivative by calculating spectra for displaced structures (i.e., as a normalized difference spectrum), but the analytical calculation is also possible and will be considered in future work. While the methodology is not restricted to a specific type of spectroscopy, VtC-XES spectroscopy have been chosen as a first example.

Such an analysis have been explored for selected structural changes in three iron carbonyl model complexes and demonstrate that it can be a useful tool for analyzing the assignment of spectral features. For VtC-XES spectroscopy, this can complement existing analysis tools based on population analysis of the orbital contributions to the different signals[16,172] that can identify which molecular fragments contribute to certain peaks in the calculated spectrum. When considering the structural sensitivity with respect to the metal-ligand bond distances, this analysis identifies similar contributions of each ligand to the peaks in the VtC-XES spectra. Moreover, the structural sensitivity can reveal which structural changes leave certain parts of the calculated spectrum unaffected, or have only little effect on the overall spectrum.

However, the structural sensitivity provides additional information and not only shows which peaks depend on contributions of certain ligands, but also provides a detailed picture of ***how***

the spectra respond to specific structural changes affecting these ligands. For the examples considered here, the characteristic patterns found for, e.g., changing Fe-CO distances, the C-O bond length of the carbonyl ligands, and CO-Fe-CO bond angles, seem to be partly preserved between different complexes. The small test set employed here does not allow to draw general conclusions, but demonstrates that the methodology presented here will provide a valuable tool for more extensive future studies.

In addition to such a use for analyzing and assigning spectral features by considering selected structural changes, the calculation of the structural sensitivity $\delta\sigma_i(E)$ for a complete set of Cartesian or internal coordinates will provide a tool for guiding the search of molecular structures that match a certain spectrum, i.e., for a structural refinement based on theoretical spectroscopy. In the context of such inverse problems, the structural sensitivity can also be used to assess the uncertainties in the calculated spectra due to the choice of the underlying structure, possibly in combination with accounting for uncertainties due to the computational methodology.[156]

Chapter 7

Application SCR: Mechanism of the selective catalytic reduction: Fe- versus Cu-exchanged zeolite catalysts

The mechanism of the reduction half-cycle of the selective catalytic reduction (SCR) of nitrogen oxides with ammonia will be computationally investigated. Both Fe- and Cu-exchanged zeolite catalysts will be compared and the aim is to explore all accessible reaction pathways. From the calculations, a comprehensive picture emerges that unifies several previous mechanistic proposals. For both Fe and for Cu catalysts, different reaction pathways are feasible, but some of the possible reaction pathways differ in these two cases. The computational results provide a basis for the interpretation of *in situ* spectroscopic investigations that can possibly distinguish the different mechanistic pathways.

The publication [173] is based on this chapter of this thesis.

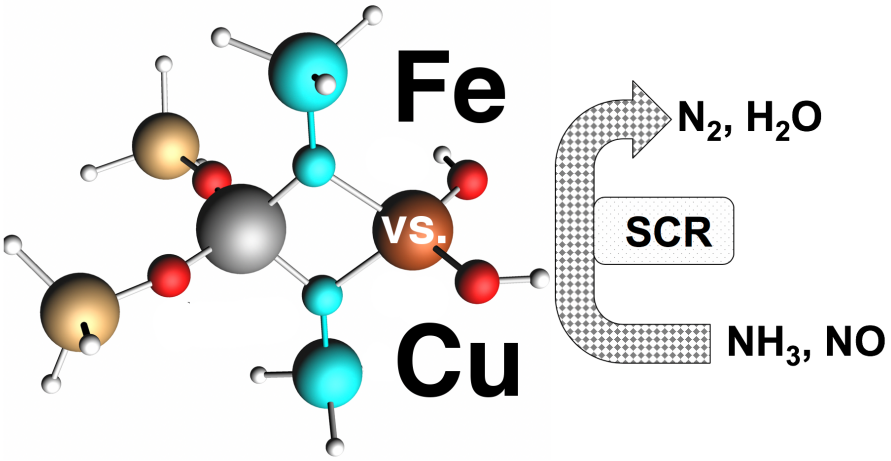

Figure 7.1: Schematic overview, which represents this chapter in one picture. An example of the developed small catalytic model system is shown. This model system is used to explain the significant differences between the SCR mechanism over iron- and copper- exchanged zeolite catalysts based on thermodynamic DFT calculations and theoretical X-ray valence-to-core emission spectroscopy.

7.1 Introduction

The selective catalytic reduction (SCR) is widely used for the removal of nitrogen oxides (NO_x) in exhaust-gas aftertreatment systems of vehicles with Diesel engines.[174–177] In the presence of suitable heterogeneous catalysts, NO_x can be reduced by reaction with ammonia injected into the exhaust-gas flow. Transition metal zeolite catalysts are available for SCR and are predominately used in automotive applications.[175,177–179] The most widely used zeolite catalysts are the iron-based Fe-ZSM-5[9,180,181] and copper-exchanged zeolites with the chabazite structure, particularly Cu-SSZ-13 and Cu-SAPO-34.[182,183] The latter are particularly attractive due to their hydrothermal stability. More recently, the chabazite iron-catalyst Fe-SSZ-13 has also been demonstrated to show high-temperature SCR activity.[184]

Both the structure of the catalytically-active metal centers in these catalysts as well as the catalytic mechanism of the SCR reaction have been studied extensively both experimentally and computationally. For the chabazite-based catalysts, the nature of the catalytically-active sites has been investigated, both for Cu-SSZ-13[87,185–187] and Cu-SAPO-34[188] as well as for Fe-SSZ-13.[189,190] Different studies agree that the major active species are single Cu(II) or Fe(III) centers located in the six-membered or eight-membered rings of the zeolite framework, where they balance the negative charge of an Al^{3+} site. Depending on the coordination of further ligands such as water, NH_3, or NO as well as on temperature, the Cu centers can detach from the zeolite framework and can become mobile.[53,187,191–194] On the other hand, Fe centers are believed to be more strongly bound and remain immobile within the zeolite framework.[190]

Even though many details of the catalytic mechanism have been elucidated, the SCR mechanism is still not fully understood.[76,195–197] This is particularly true for Fe-exchanged zeolite catalysts, which have been studied less extensively than Cu-exchanged zeolite catalysts. While for Cu catalysts, computational studies explored different possible mechanistic pathways,[23,53,54,188,198,199] a comprehensive computational picture of the SCR mechanism for Fe catalysts is still lacking.[195,200] Here, the aim is to close this gap by computationally exploring different possible mechanistic pathways for the reduction half-cycle of the SCR reaction with Fe catalysts. In addition, these reaction pathways for Fe and Cu zeolite catalysts were compared in order to provide a unified picture.

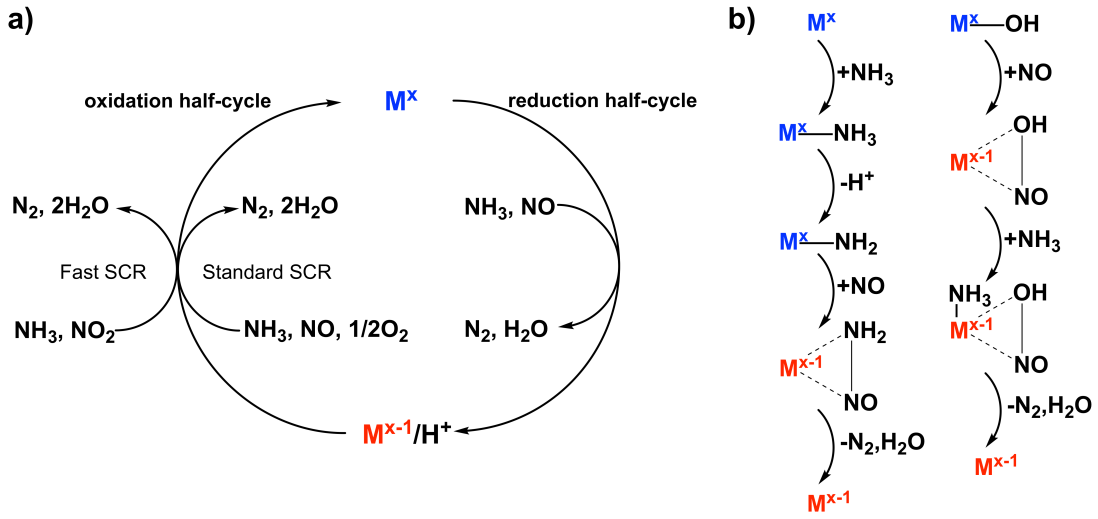

Figure 7.2: (a) Schematic redox cycle for the standard and fast SCR reaction. M^x (blue) denotes the oxidized catalytic metal center, while M^{x-1} (red) refers to a reduced form of the catalytic metal center. (b) Possible simplified reactions mechanisms for the SCR reduction half-cycle on the "NH_3-first pathway" (left) and the "NO-first pathway" (right).

There is general agreement that the SCR reaction proceeds via the redox cycle schematically shown in Fig. 7.2a (Ref. [197]). First, in the reduction half-cycle, NO and NH_3 react to N_2 and H_2O while reducing the catalytic metal center. Second, in the oxidation half-cycle, the catalytic metal center is reoxidized. This slow reoxidation is generally considered to be the rate-determining step. The reaction equation of the oxidation half-cycle will differ depending on the availability of NO_2 (see Fig. 7.2a). Different detailed mechanistic proposals have been made for the oxidation half-cycle with Cu-exchanged zeolite catalysts under both standard SCR and fast SCR conditions.[53,54,188,198,199,201] Most likely, the oxidation half-cycle proceeds via the formation of dimeric Cu species.[53,62]

Here, the focus is on the reduction half-cycle of the SCR reaction. Most generally, this first part of the SCR reaction can proceed via two different mechanistic pathways (see Fig. 7.2b) by either adsorbing NH_3 or NO at the catalytic metal center in the first step. If NH_3 is coordinated first

("NH_3-first pathway"), a proton needs to be transferred either to another ligand or to the zeolite framework. NO can subsequently either be adsorbed at the metal center or directly attack the coordinated NH_2 ligand. Both possibilities lead to the release of N_2 and H_2O via an NH_2NO intermediate. If NO reacts first ("NO-first pathway"), one generally assumes the intermediate formation of a HONO ligand, either via an intermediate NO complex or via a direct attack of NO at an OH^- ligand. Subsequently, this HONO ligand reacts with NH_3 to form N_2 and 2 H_2O. Again, this step could proceed either via intermediates in which NH_3 is coordinated to the metal center or via a direct attack of NH_3 at the HONO ligand.

Previous computational studies for Cu-exchanged zeolite catalysts provide an ambiguous picture for the reduction half-cycle. While Refs. [53, 54, 188] assume the SCR reduction-half cycle to proceed via the "NH_3-first pathway", Refs. [198, 199] consider the "NO-first pathway". In Ref. [201] both pathways are explored, with the computational results suggesting that the reaction via a HONO intermediate is preferred. Further details of these different mechanistic proposals will be discussed below. Based on kinetic and spectroscopic studies of SCR catalyzed by Fe-ZSM-5, mechanisms proceeding via different variants of an "NO-first pathway" have been suggested,[60,202] whereas computational investigations assumed mechanisms via the "NH_3-first pathway".[200,203]

7.2 Computational Methodology

The molecular structures of all considered models have been optimized using DFT as implemented in the Amsterdam density functional (ADF) program package,[132,133] employing the BP86 generalized-gradient approximation (GGA) exchange-correlation functional[98,99] in combination with the Slater-type TZ2P basis set.[134] Further details on the construction of the model structures are given in the Sec. 7.3. All relative energies refer to the differences in the total electronic energy without additional corrections. For all Fe(III) species the ground-state is the high-spin ($S = 5/2$) state, while for Fe(II) both the low-spin ($S = 0$) and the high-spin ($S = 2$) state were considered. For all Cu(I) models, a closed-shell singlet ground state was assumed, whereas for all Cu(II) models, spin-unrestricted calculations were performed for the doublet ($S = 1/2$) ground state. Optimized molecular structures as well as all calculated relative energies are shown in Fig. 7.5–7.6 and Table I–II, respectively. For comparison, all calculations have been repeated using the B3LYP hybrid exchange-correlation functional[135] with the same basis set as well as including Grimme's D3 dispersion correction[204] (see Secs. 7.4.1.1, 7.4.1.2, 7.4.2.1 and 7.4.2.2). XES spectra were calculated using the standard ΔDFT approach[91,115] including higher-order intensity contributions[113] with BP86/QZ4P. Fe K-edge and Cu K-edge spectra have been shifted by 181.34 eV and by 229.14 eV, respectively, in order to align them with the experimental energy scale.

7.3 Construction of the active-site model

7.3.1 Minimal active site model

The minimal model of the active site in Fe- and Cu-exchanged zeolites is based on the cluster model of Cu-SSZ-13 shown in Fig. 7.3a. This cluster model has been obtained from a crystal structure of the zeolite, and the terminal Si atoms have been saturated with hydroxyl groups.

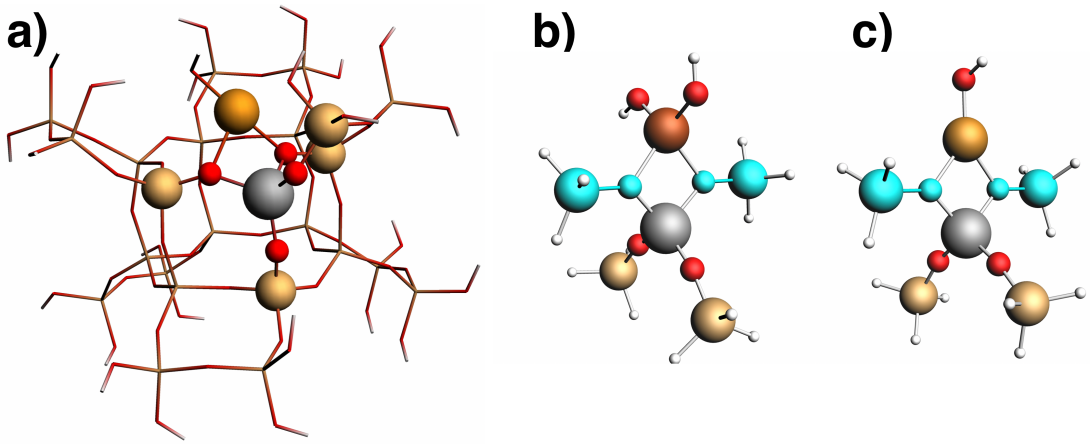

Figure 7.3: (a) Optimized molecular structure of a model of the active metal center in Cu-SSZ-13. The atoms shown here in as spheres are used in the minimal model of the catalytic centers employed in the calculations. (b) Optimized molecular structure of the starting model of the active centers in Fe-exchanged zeolite catalysts [Z-$Fe^{III}(OH)_2$]. (c) Optimized molecular structure of the starting model of the active centers in Cu-exchanged zeolite catalysts [Z-$Cu^{II}(OH)$]. Color code: Fe (dark brown), Cu (orange), O (red), N (blue), Al (grey), Si (light brown) and H (white). The coordinates of the atoms highlighted in cyan for models (b) and (c) are kept fixed at their positions in model (a) in all calculations.

The minimal models shown in Figs. 7.3b and c have been obtained from this cluster model and terminal silicon atoms were saturated with hydrogen atoms. The atomic coordinates of the atoms highlighted in these figures were fixed in all further geometry optimizations in order to preserve the structure of the active site. For Fe-exchanged and Cu-exchanged zeolites, the metal centers were saturated with hydroxyl groups in order to obtain an overall neutral model. To estimate the stability of such a neutral active-site model for Fe zeolite catalyst compared to a positively-charged model of the active site, the hypothetical reaction were considered

$$[\text{Z-Fe}^{\text{III}}(\text{OH})_2] \longrightarrow [\text{Z-Fe}^{\text{III}}(\text{OH})]^+ + \text{OH}^-(\text{aq}),$$

where the energy of $\text{OH}^-(\text{aq})$ was calculated using the COSMO solvation model[114] with standard parameters of water in order to obtain an estimate for the stabilization or coordination of a hydroxyl group within the zeolite framework. Within this crude model, the neutral active-site

model is clearly preferred by 502 kJ/mol.

Similarly, for comparing a neutral active-site model for Cu zeolite catalyst compared to a negatively-charged model of the active site, the hypothetical reaction

$$[\text{Z-Cu}^{\text{II}}(\text{OH})] + \text{OH}^-(\text{aq}) \longrightarrow [\text{Z-Cu}^{\text{II}}(\text{OH})_2]^-,$$

were considered and an energy difference of only 17 kJ/mol were obtained. Therefore, all calculations of intermediates with Cu catalysts have also been repeated for the negatively charged model of the active site (see Section 7.4.3).

All relative energies were calculated by as differences of the total electronic energies of the corresponding active-site models, possibly included also the total electronic energies of the relevant gas-phase molecules, which were calculated for the isolated molecules without any solvation model. Zero-point corrections were not included as the active-site models were obtained from constraint geometry optimizations and do thus nor correspond to true minima on the potential energy surface. This precludes the calculation of the corresponding vibrational frequencies.

No entropic corrections were applied to the electronic energies, as large errors have to be expected with the conventionally used models because (a) a free-particle approximation is nor appropriate for the involved gas-phase molecules within the zeolite framework; (b) rotational contributions are not meaningful for the active-site models that form part of the fixed zeolite framework; and (c) vibrational contributions are not accessible because constraint geometry optimizations have been employed. The largest entropic contributions are expected for the steps involving the adsorption of release of molecules from or to the gas phase. The prediction of ΔG for these steps will require more a advanced computational methodology as well as the consideration of temperature and partial pressures of the involved gas-phase species (see, e.g., Refs [53, 54]). Thus, the inclusion of entropic contributions is beyond the scope of the present work that only aims at identifying and comparing feasible catalytic reaction pathways.

7.3.2 Comparison with larger zeolite model and NH_3 solvated model

To assess the impact of using the minimal active-site model described above on the relative energies of different catalytic intermediates, also calculations for selected intermediates (**A**-**G**, **J**) of the "NH_3-first pathway" for the large zeolite model, shown in Fig. 7.3a, were performed (all intermediates are marked with capital letters, see Fig. 7.5). For this large model, the coordinates of all atoms were fully optimized. The comparison of the BP86/TZ2P results for this large and the minimal active-site model is shown in the left part of Fig. 7.4.

While there are some notable differences between the two models for **B**, **C**, and **J**, the relative energies of the remaining intermediates are hardly changed when using the larger model. Overall,

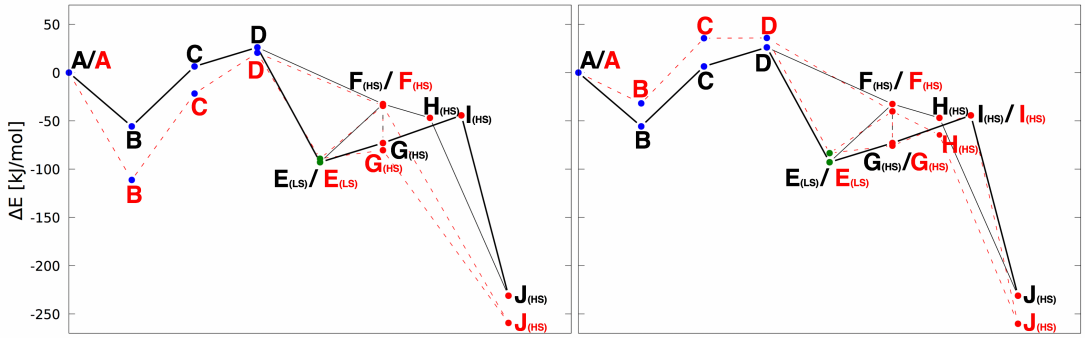

Figure 7.4: Comparison of the energy profiles for the considered reaction pathways of the reduction-half cycle of the SCR reaction catalyzed by **Fe-exchanged zeolite catalysts** calculated with BP86/TZ2P for minimal active-site model (black) compared to the larger zeolite model (red) [left] and for the minimal active-site model (black) compared to 'NH_3-solvated model' (red) [right]. Only the lowest-energy spin state is included for each intermediate.

the energy profiles remain qualitatively unchanged. In addition, the right part of Fig. 7.4 compares the BP86/TZ2P results for the minimal active-site model to a model of a NH_3-solvated Fe center, i.e., using $[Fe^{III}(NH_3)_2(OH)_2]^+$ as starting point, that does not include the zeolite at all. While also in this case, the relative energies of some of the intermediates change, the overall energy profile remains qualitatively unchanged.

Overall, these findings give confidence that the minimal active-site model is sufficient to identify feasible reaction pathways and to reveal intrinsic mechanistic differences between Fe- and Cu-catalysts that are independent of the precise nature of the active center.

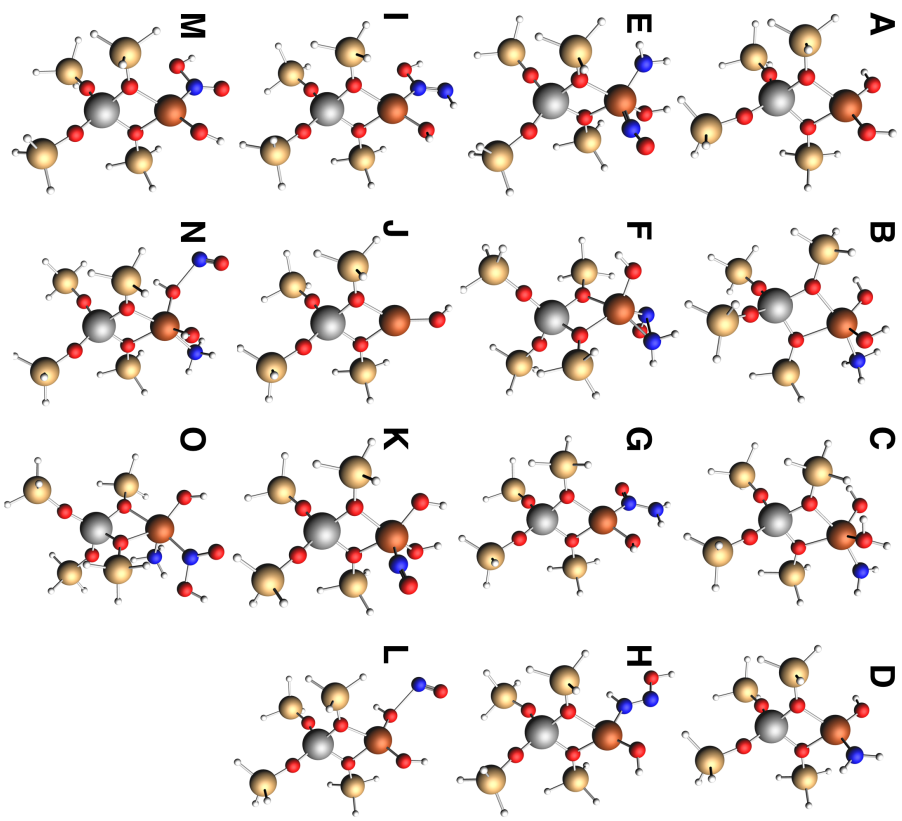

Figure 7.5: Optimized molecular structures (BP86/TZ2P) for all considered intermediates for Fe-exchanged zeolite catalysts.

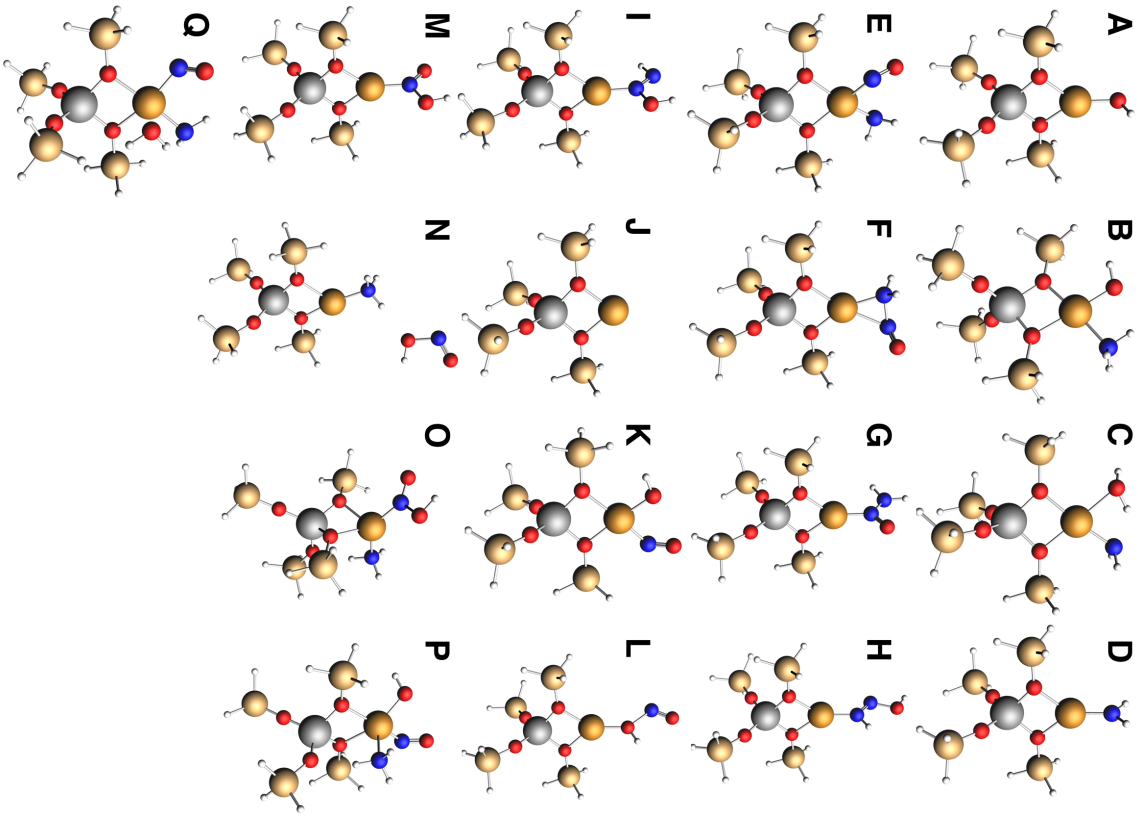

Figure 7.6: Optimized molecular structures (BP86/TZ2P) for all considered intermediates for Cu-exchanged zeolite catalysts.

Table I: Calculated BP86/TZ2P and B3LYP/TZ2P relative energies (ΔE, with respect to model **A**) and spin-state energy differences (ΔE_{spin}, with respect to the low-spin state of the same model) for all calculated intermediates for Fe-exchanged zeolite catalysts.

		BP86/TZ2P		B3LYP/TZ2P	
	Spin	ΔE	ΔE_{spin}	ΔE	ΔE_{spin}
A	5/2	0.0	−78.5	0.0	
	1/2		0.0		
B	5/2	−55.7	0.0	−56.4	
C	5/2	6.4		15.6	
D	5/2	26.1	0.0	31.9	0.0
	1/2		56.1		108.8
E	0	−92.8	0.0		0.0
	2		62.2	29.3	−82.7
F	0		0.0		0.0
	2	−32.5	−55.8	−9.9	−139.3
G	0		0.0		0.0
	2	−73.0	−55.2	(-58.3)[a]	(-193.5)[a]
H	0		0.0		0.0
	2	−46.9	−70.4	(-34.7)[a]	(-186.3)[a]
I	0		0.0		0.0
	2	−44.3	−60.5	−38.6	−195.4
J	0		0.0		0.0
	2	−231.1	−142.3	−268.8	−229.7
K	0	−95.4	0.0		0.0
	2		48.4	−5.1	−108.8
L	0		0.0		0.0
	2	−15.0	−80.2	−2.6	−139.5
M	0		0.0		0.0
	2	−17.9	−71.2	24.7	−154.2
N	0		0.0		0.0
	2	−71.7	−84.9	−59.8	−161.7
O	0		0.0		0.0
	2	−85.4	−2.9	−37.6	−95.2

[a] geometry optimization not fully converged

Table II: Calculated BP86/TZ2P and B3LYP/TZ2P relative energies (ΔE, with respect to model **A**) for all calculated intermediates for Cu-exchanged zeolite catalysts.

	Spin	BP86 ΔE	B3LYP ΔE
A	1/2	0	0
B	1/2	−76.4	−82.3
C	1/2	−28.5	−23.4
D	1/2	−20.2	−11.9
E	0	−76.6	3.8
F	0	−112.5	−70.9
G	0	−153.9	−112.9
H	0	−145.0	−111.0
I	0	−134.2	−98.3
J	0	−237.1	−270.0
K	0	−92.7	−17.2
L	0	−63.8	−21.6
P	0	−142.7	−87.1
Q	0	−106.8	−27.3
M	0	−114.3	−61.1
N	0	−134.9	−128.1
O	0	−146.2	−82.0

7.4 Results and Discussion

7.4.1 Iron SCR reaction pathways

In the first step, possible reaction pathways for the reduction half-cycle of the SCR reaction with Fe-exchanged zeolite catalysts (see Fig. 7.7) were considered for the overall neutral model [Z-Fe^{III}(OH)$_2$] (**A**, see Fig. 7.3b) with a d^5 high-spin electron configuration. Such species have been identified as the major monomeric Fe species in Fe-SSZ-13 catalysts.[189]

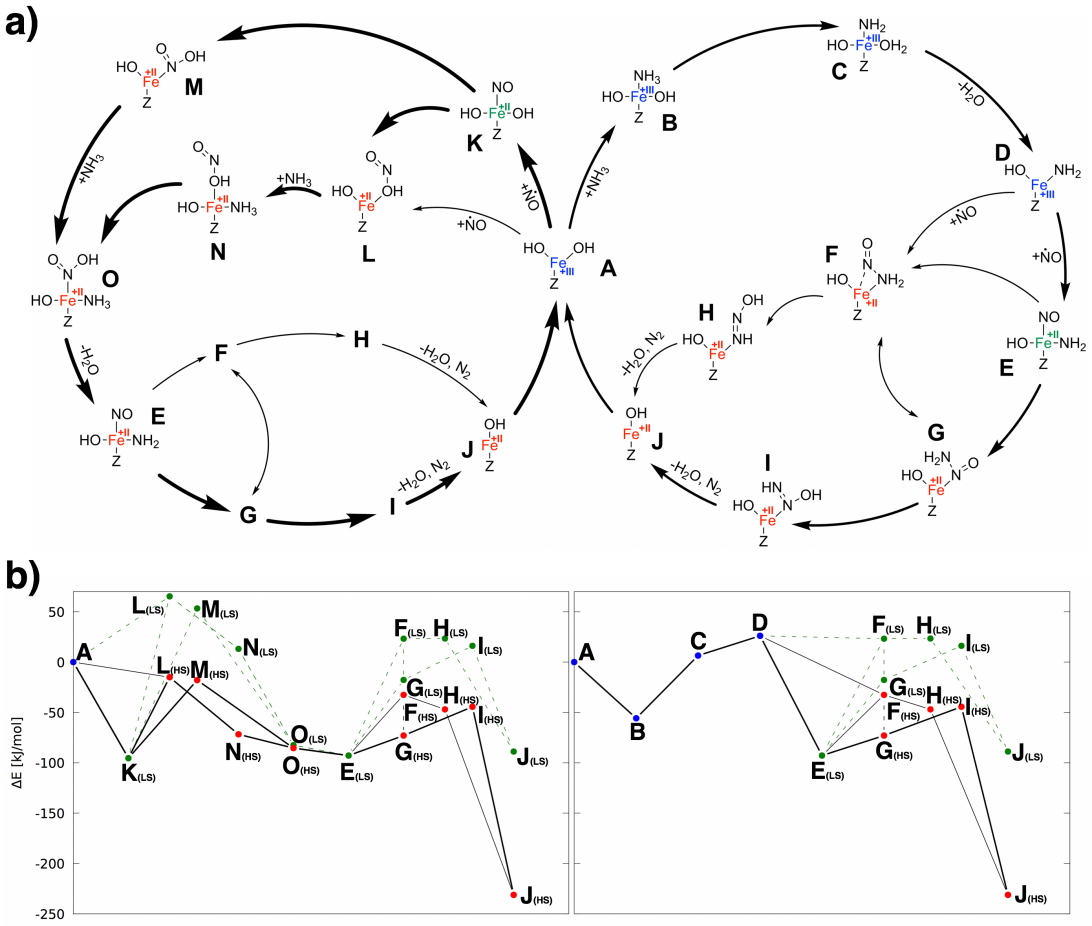

Figure 7.7: (a) Reaction pathways considered for the mechanism of the reduction-half cycle of the SCR reaction catalyzed by **Fe-exchanged zeolite catalysts**. Both pathways staring with the adsorption of NO (left) and with the adsorption of NH_3 (right) are considered. (b) Calculated energy profiles (BP86/TZ2P) for the considered reaction pathways. For all Fe(III) species (blue), the high-spin ($S = 5/2$) state is the ground-state. For the Fe(II) species the calculated energies of both the high-spin ($S = 2$, red) and low-spin ($S = 0$, green) state are included.

The first possible SCR reaction pathway ("NH_3-first pathway", see right part of Fig. 7.7a) starts with the adsorption of NH_3, leading to [Z-Fe^{III}(OH)$_2$(NH_3)] (**B**). This step is exothermic

by −56 kJ/mol. Subsequently, a proton is shifted from the NH_3 ligand to one of the OH^- ligands, resulting in [Z-Fe^{III}(OH)(H_2O)(NH_3)] (**C**), which can abstract a water molecule to arrive at [Z-Fe^{III}(OH)(NH_2)] (**D**). This proton shift and the water abstraction are endothermic and altogether require 82 kJ/mol. However, we could not identify any feasible alternatives on the "NH_3-first pathway".

Intermediate **D** can now react with NO in two different ways. First, NO can be coordinated to form [Z-Fe^{II}(OH)(NH_2)(NO)] (**E**), reducing Fe(III) to low-spin ($S = 0$) Fe(II). A rearrangement, in which the NH_2 ligand shifts to form a N-N bond, then leads to [Z-Fe^{II}(OH)($NONH_2$)] (**G**). According to our computations, **G** has a high-spin ($S = 2$) ground-state, i.e., this step requires a spin crossover. Species **G** can release N_2 and H_2O via (**I**), finally resulting in a reduced iron species [Z-Fe^{II}(OH)] (**J**). Alternatively, one could assume a direct reaction of NO from the gas phase with the NH_2 ligand. The only plausible resulting intermediate that we could find in our calculations is species **F**, which contains an ON-NH_2 ligand coordinated to the Fe center via the nitrogen atoms. Again, our computations show a high-spin ($S = 2$) ground-state for this species, which could further react to **J** under release of N_2 and H_2O. However, the formation of the alternative intermediate **E** from **D** is exothermic by −119 kJ/mol, while **F** is 60 kJ/mol higher in energy than **E**. Therefore, this reaction path would most likely proceed via **E** with a coordination of NO to the iron center instead of a direct reaction of NO from the gas phase.

The second possible SCR reaction pathway ("NO-first pathway", see left part of Fig. 7.7a) starts with the adsorption of NO, leading to [Z-Fe^{II}(OH)$_2$(NO)] (**K**) while reducing the Fe center to low-spin ($S = 0$) Fe(II). This step is exothermic by −95 kJ/mol. The subsequent formation of a intermediate [Z-Fe^{II}(OH)$_2$(NO)(NH_3)], in which NO and NH_3 are simultaneously coordinated to the Fe center, was not stable in our computations. Instead, **K** rearranges under formation of a HONO ligand, which could either be coordinated via an oxygen atom (**L**) or via the nitrogen atom (**M**), which are almost equal in energy. Both **L** and **M** have a high-spin ($S = 2$) ground-state in our calculations and the formation of the HONO ligand thus requires a spin crossover.

After the formation of **L** or **M**, NH_3 can coordinate, resulting in [Z-Fe^{II}(HONO)(NH_3)] with HONO coordinated via the an oxygen atom (**N**) or via the nitrogen atom (**O**), respectively. This step is exothermic by 57 kJ/mol and 68 kJ/mol, respectively, and the two intermediates **N** and **O** differ in energy by only 14 kJ/mol. Abstraction of H_2O from **O** leads to [Z-Fe^{II}(OH)(NH_2)(NO)] (**E**), which can release N_2 and H_2O via **G** and **I** or via **F** and **I** (see above).

Overall, according to the calculations a mechanism via the "NO-first pathway" seems more likely, as it does not require the energetically unfavorable intermediate **D** that needs to be formed on the "NH_3-first pathway". The highest-energy intermediates on the "NO-first pathway" are **L** and **M**, which are 41-44 kJ/mol lower in energy than **D**. Both the mechanisms via **L** and **M**, i.e., via the formation of a HONO ligand and subsequent adsorption of NH_3, are possible according to our computational results. According to our calculations, all accessible reaction pathways require

spin crossover from low-spin to high-spin Fe(II). However, because of the known insufficiencies of density-functional approximations for spin-state energy differences[205–207] it cannot be ruled out that for some of our high-spin Fe(II) intermediates the corresponding low-spin species are actually more stable (see Sec. 7.4.1.1 for additional calculations and discussion).

7.4.1.1 Comparison DFT functionals: BP86 vs. B3LYP

In order to assess the dependence of the computational results on the exchange-correlation functional, all BP86/TZ2P calculations were repeated with B3LYP/TZ2P. The corresponding energies are included in Table I. Fig. 7.8 compares the calculated energy profiles. Overall, very similar relative energies are obtained for all Fe(III) species, whereas for the Fe(II), B3LYP provides higher relative energies compared to **A**. However, these differences do not affect the general conclusions.

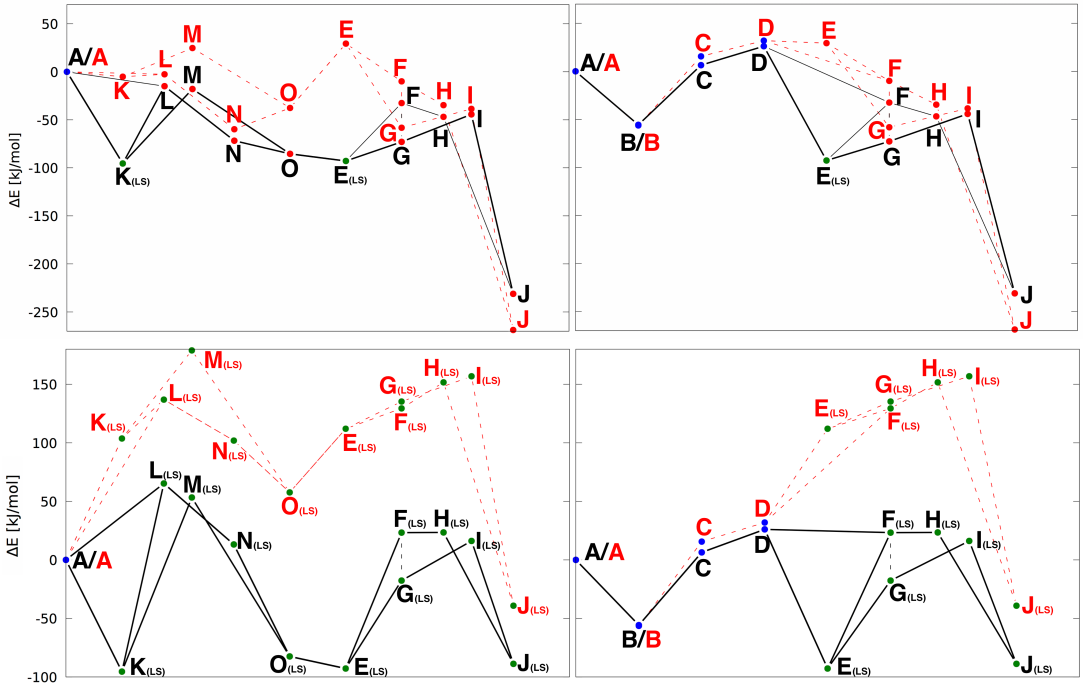

Figure 7.8: Comparison of the energy profiles for the considered reaction pathways of the SCR reaction catalyzed by **Fe-exchanged zeolite catalysts** calculated with BP86/TZ2P (black) and B3LYP/TZ2P (red). [**top**] Only the lowest-energy spin state is included for each intermediate. [**bottom**] All low-spin state of the Fe(II) species are presented.

For all Fe(II) species, with the B3LYP hybrid functional provides a larger spin-state energy difference between the low-spin and the high-spin state and stabilizes the high-spin state. This is in line with the well-known tendency of hybrid functionals to prefer high-spin states.[205,207] Thus, both the non-hybrid BP86 and the hybrid B3LYP functional consistently point to a

high-spin ground state for the involved Fe(II) species (see also Fig. 7.8).

7.4.1.2 Comparison dispersion: BP86/B3LYP vs. BP86-D3/B3LYP-D3

In order to assess the dependence of the computational results on dispersion correction, all BP86/TZ2P and B3LYP/TZ2P calculations were repeated with BP86-D3/TZ2P and B3LYP-D3/TZ2P. Fig. 7.9 compares the calculated BP86/TZ2P and B3LYP/TZ2P energy profiles with and without the D3 dispersion correction. Overall, very similar relative energies are obtained for all Fe species, and the inclusion of dispersion corrections does not change the general conclusions.

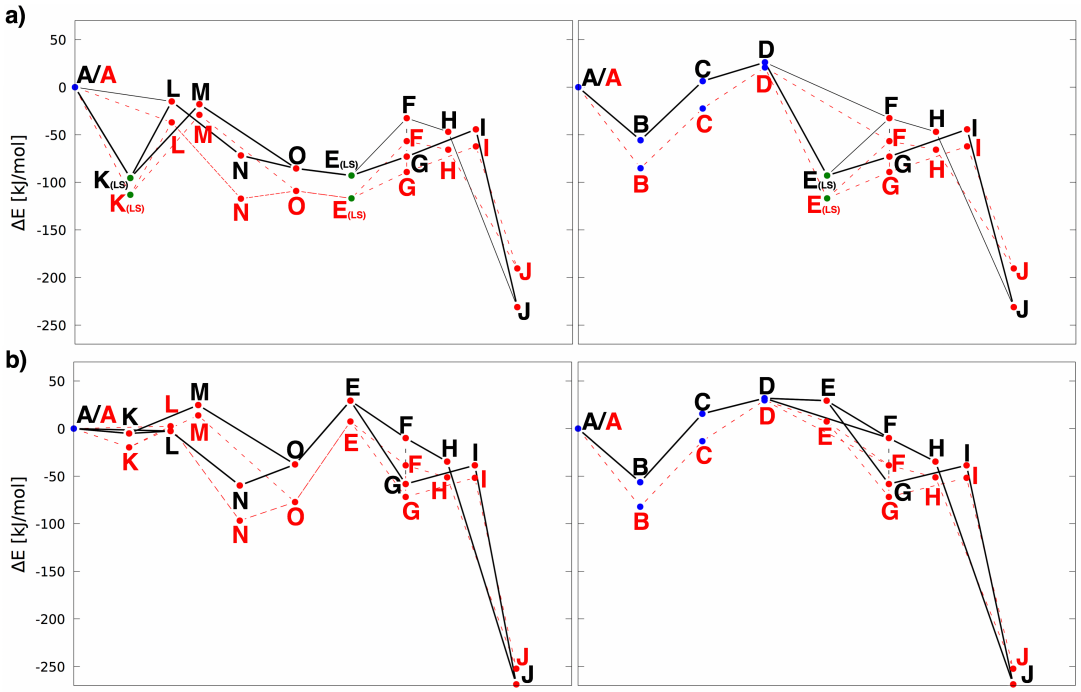

Figure 7.9: Comparison of the energy profiles for the considered reaction pathways of the reduction-half cycle of the SCR reaction catalyzed by **Fe-exchanged zeolite catalysts** calculated with **a)** BP86/TZ2P (black) compared to BP86-D3/TZ2P (red) and **b)** with B3LYP/TZ2P (black) compared to B3LYP-D3/TZ2P (red).

7.4.2 Copper SCR reaction pathways

For comparison, we considered the same possible reaction pathways for the SCR reaction catalyzed by Cu-exchanged zeolites (see Fig. 7.10). Here, the overall neutral model [Z-Cu^{II}(OH)] (**A**, see Fig. 7.3c) is the starting structure, which is in line with the neutral models considered in Refs. [53, 198, 201]. Similar results are obtained for a negatively-charged model [Z-$Cu^{II}(OH)_2]^-$ resembling the models used in Refs. [54, 188, 199] (see Sec. 7.4.3).

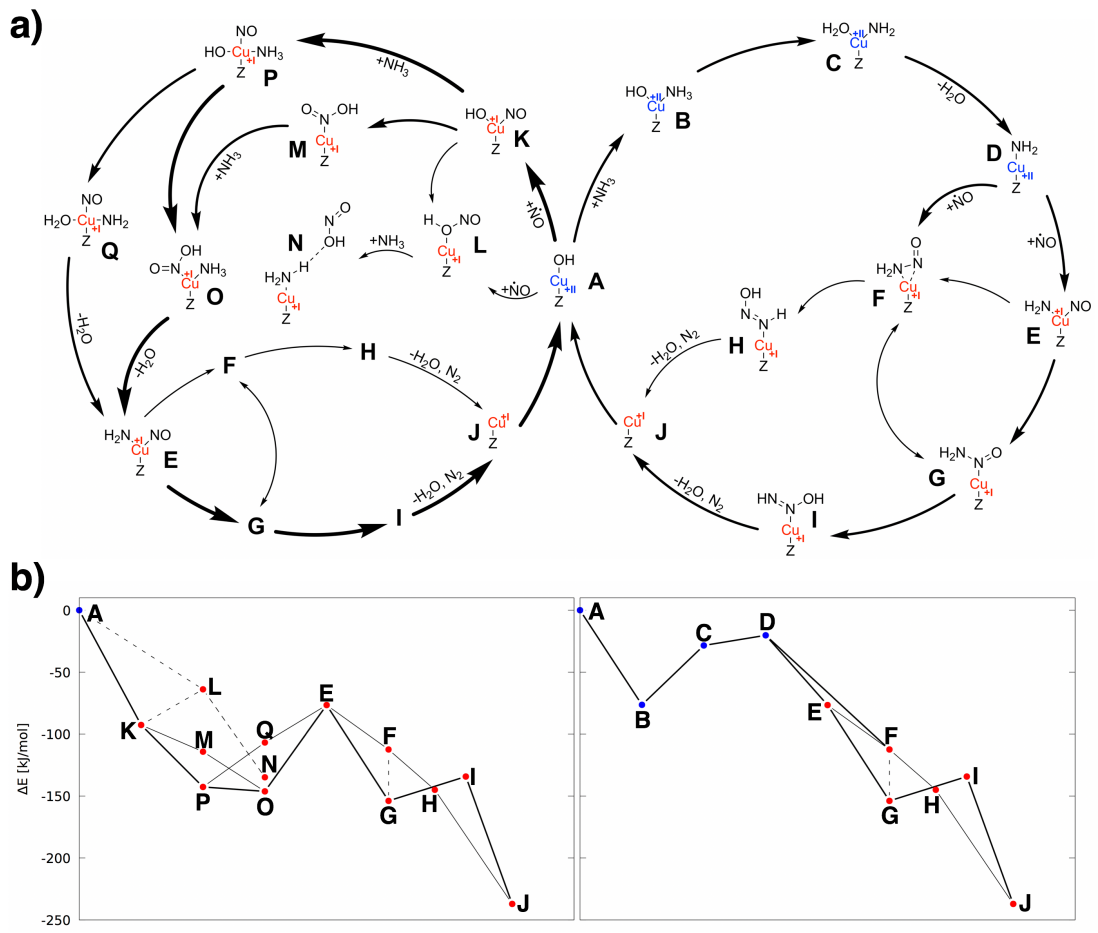

Figure 7.10: (a) Reaction pathways considered for the mechanism of the reduction-half cycle of the SCR reaction catalyzed by **Cu-exchanged zeolite catalysts**. Both pathways staring with the adsorption of NO (left) and with the adsorption of NH_3 (right) are considered. (b) Calculated energy profiles (BP86/TZ2P) for the considered reaction pathways.

For the "NH_3-first pathway" (see right part of Fig. 7.10), the same possible reaction steps and intermediates as for the case of Fe-exchanged zeolite catalysts was found, even though the relative energies of the different intermediates differ. Most importantly, the transfer of a proton from the NH_3 ligand to the OH ligand and the subsequent abstraction of water (**B** to **D**) now require only 56 kJ/mol, with **D** lying lower in energy by 20 kJ/mol than the starting point **A**. Note that some previous calculations assume a proton transfer to the zeolite framework in this step,[53,54,188] which cannot be described by our small model. However, according to Ref. [188] such a proton transfer would require 114 kJ/mol. The further reactions via the formation and decomposition of an ON-NH_2 ligand (**F** or **G**) can proceed via steps that are all exothermic or only require little energy.

For the "NO-first pathway" (see left part of Fig. 7.10), there are some fundamental differences to the case of Fe-exchanged zeolite catalysts. After coordination of NO (**K**) the formation of a

HONO ligand coordinated via its oxygen atom **L** leads to the dissociation of the HONO ligand after coordination of NH_3 (**N**). Thus, this path does not lead to the reduction of NO. Instead, the formation of a HONO ligand coordinated via its nitrogen (**M**) atom is preferred and leads to **O** after coordination of NH_3. Alternatively, ammonia can coordinate to **K** under formation of **P**. Such an intermediate was not available in the case of an Fe zeolite catalyst. Here, the formation of **P** is energetically preferred compared to **M** by 28 kJ/mol, but both can further react to the same intermediate **O**. The remaining steps proceed via the formation of **E**, which is endothermic by +70 kJ/mol, and match those discussed above for Fe zeolite catalyst.

Overall, also for Cu-based zeolite catalysts the "NO-first pathway" seems to be preferred, even though on the "NH_3-first pathway" the high-energy intermediate **D** is more favorable in the case of a Cu catalyst than for an Fe catalyst. However, for a Cu catalyst the "NO-first pathway" cannot proceed via an intermediate **L** as it does for Fe catalysts. Instead, the SCR reaction will most likely proceed via intermediate **P**, which is not accessible with an Fe catalyst. The only slightly disfavored route via **M** is available for both Cu and Fe catalysts.

7.4.2.1 Comparison DFT functionals: BP86 vs. B3LYP

A comparison of the energy profiles obtained for the neutral active-site model of Cu-exchanged zeolite catalysts with BP86/TZ2P and with B3LYP/TZ2P is shown in Fig. 7.11. Similar as for the Fe catalyst, these are very similar for the Cu(II) species, but B3LYP provides higher relative energies for the open-shell Cu(II) species. Nevertheless, the general conclusions remain unaffected.

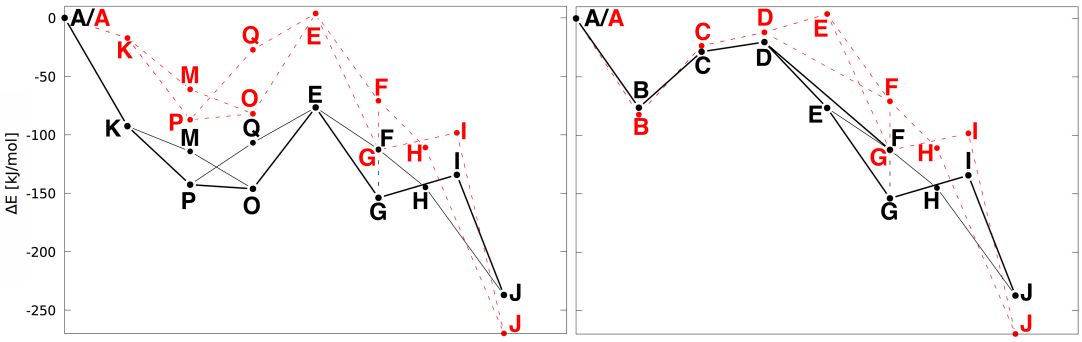

Figure 7.11: Comparison of the energy profiles for the considered reaction pathways of the SCR reaction catalyzed by **Cu-exchanged zeolite catalysts** (neutral active-site model) calculated with BP86/TZ2P (black) and with B3LYP/TZ2P (red).

7.4.2.2 Comparison dispersion: BP86/B3LYP vs. BP86-D3/B3LYP-D3

In order to assess the dependence of the results on dispersion correction, all calculations were repeated with BP86-D3/TZ2P and B3LYP-D3/TZ2P. Fig. 7.12 compares the calculated energy profiles. Similar as for the Fe catalyst, the relative energies obtained for all Cu species are very similar, and the inclusion of dispersion corrections does not change the general conclusions.

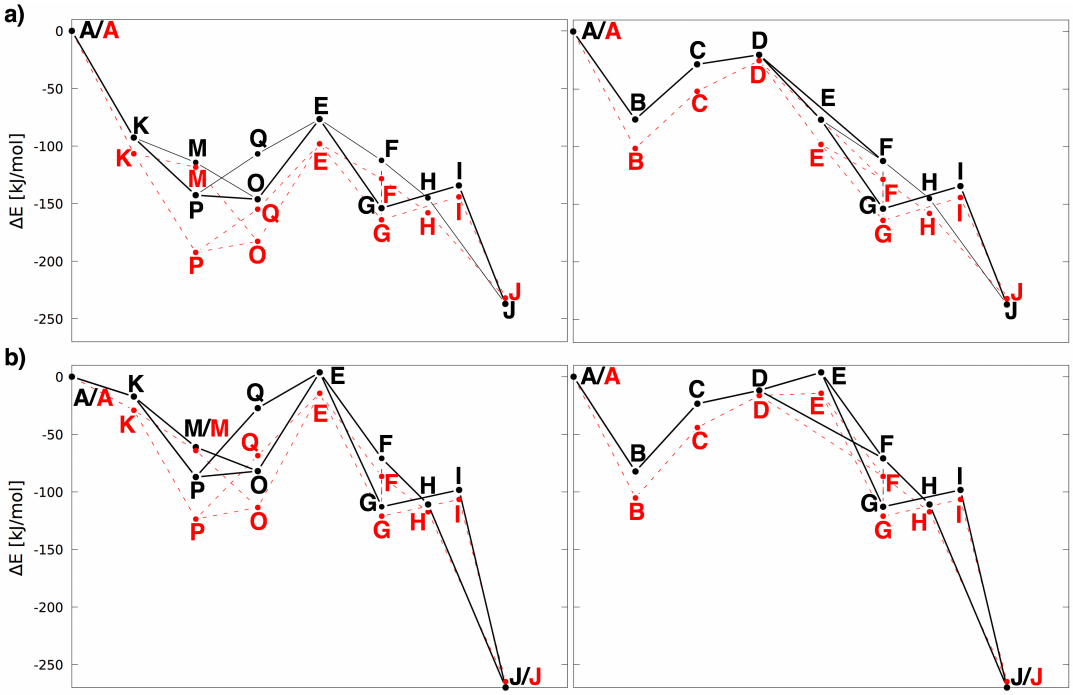

Figure 7.12: Comparison of the energy profiles for the considered reaction pathways of the SCR reaction catalyzed by **Cu-exchanged zeolite catalysts** calculated with **a)** BP86/TZ2P (black) compared to BP86-D3/TZ2P (red) and **b)** with B3LYP/TZ2P (black) compared to B3LYP-D3/TZ2P (red).

7.4.3 Copper negatively-charged active-site model

The possible reaction pathways for a negatively-charged model of the active site of Cu-exchanged zeolites are summarized in Fig. 7.13, and the corresponding relative energies are listed in Table III.

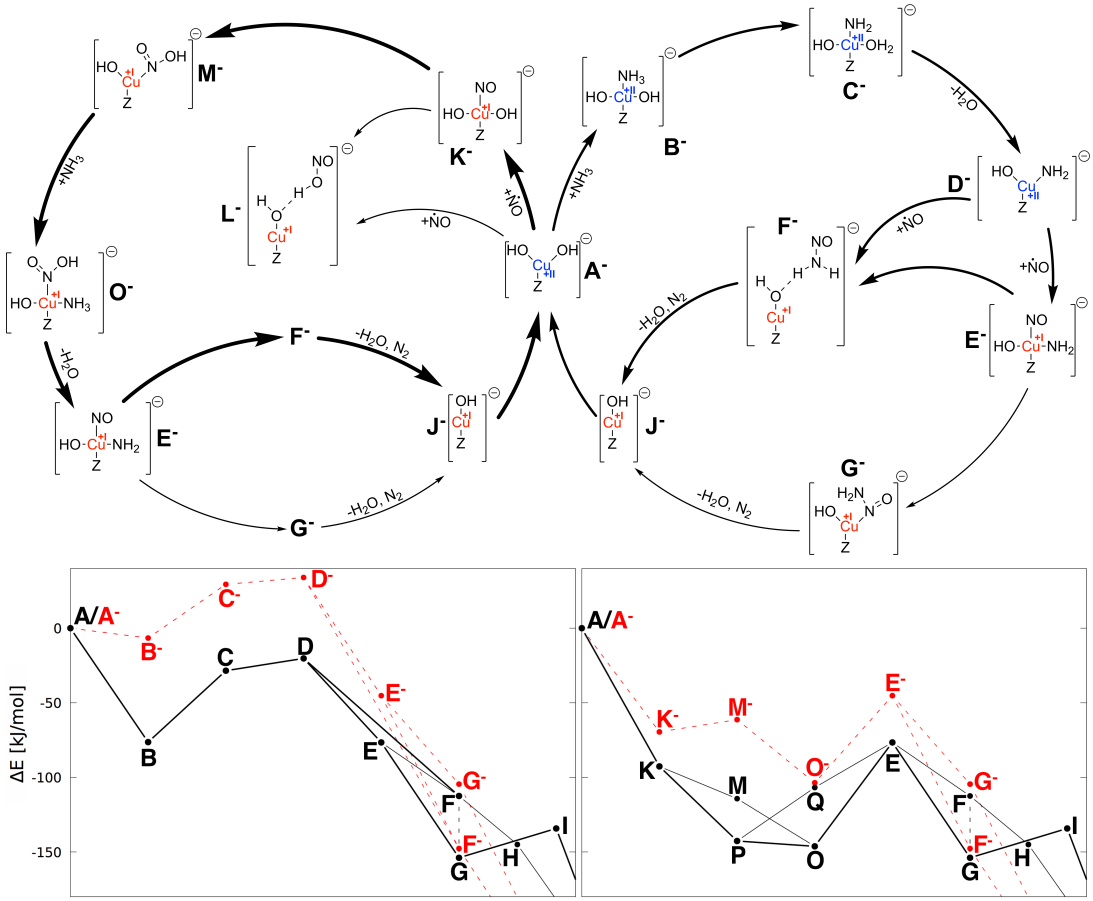

Figure 7.13: (a) Reaction pathways considered for the mechanism of the reduction-half cycle of the SCR reaction catalyzed by **Cu-exchanged zeolite catalysts with a negatively-charge model of the active center**. Both pathways staring with the adsorption of NO (left) and with the adsorption of NH_3 (right) are considered. (b) Calculated energy profiles (BP86/TZ2P) for the considered reaction pathways (red) in comparison to the energy profile calculated for a neutral model of the active center (black).

Table III: Calculated BP86/TZ2P and B3LYP/TZ2P relative energies (ΔE, with respect to model **A**) for all calculated intermediates for Cu-exchanged zeolite catalysts using a negatively-charged active site model.

		BP86	B3LYP
	Spin	ΔE	ΔE
A^-	1/2	0.0	0.0
B^-	1/2	−6.6	−6.8
C^-	1/2	29.4	N/A
D^-	1/2	34.0	45.4
E^-	0	−45.2	48.6
F^-	0	−147.7	−104.1
G^-	0	−104.5	−117.3
H^-		N/A	
I^-		N/A	
J^-	0	−306.9	−310.7
K^-	0	−69.5	22.2
L^-	0	−131.5	−93.8
P^-		N/A	
Q^-		N/A	
M^-	0	−61.3	13.8
N^-		N/A	
O^-	0	−103.6	−14.4

7.4.4 Valence-to-Core X-ray Emission Spectroscopy (VtC-XES)

The computational elucidation of the possible catalytic reaction pathways provides the basis for spectroscopic identification of catalytic intermediates. A unique method for this purpose is provided by X-ray spectroscopy.[88,208] Based on *in operando* valence-to-core X-ray emission spectroscopy (VtC-XES), previously a peak at ca. 7087 eV ("Peak A") was observed for Fe-ZSM-5 that appears at lower energies than the peak due to the lone pair at ligands coordinated via oxygen (ca. 7091 eV. "Peak B") and peak due to the lone pair at ligands coordinated via nitrogen (ca. 7096 eV, "Peak C"). This led to the conclusion that with Fe-ZSM-5, the SCR reaction proceeds via the "NO-first pathway"[22] with an intermediate featuring HONO coordinated via its central oxygen atom that bears a positive partial charge. On the other hand, for Cu-SSZ-13 such a peak is absent from the *in operando* XES spectra and thus a different mechanism via the "NH_3-first pathway" seems to be employed.[23]

To reconcile these earlier spectroscopic results with the present computational study, the XES spectra of all considered intermediates were calculated. The calculated spectra of selected inter-

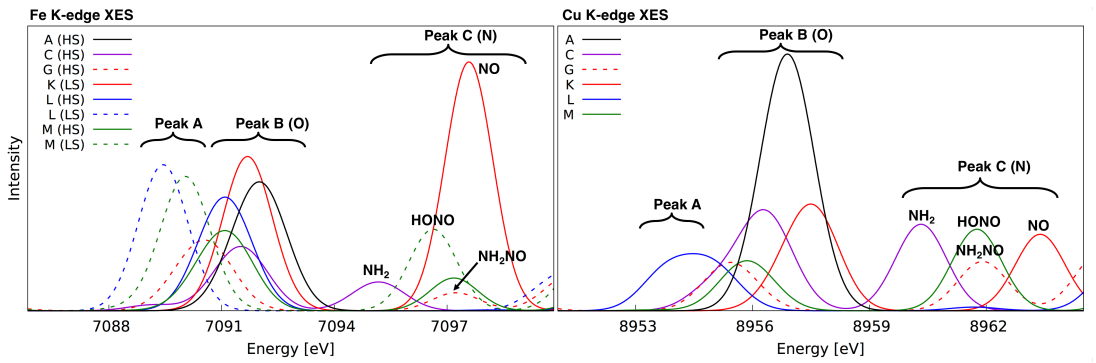

Figure 7.14: Calculated (BP86/QZ4P) Fe K-edge and Cu K-edge XES spectra of selected intermediates on the considered catalytic reaction pathways of the SCR reaction with Fe catalysts (left) and with Cu catalysts (right). The indicated assignment refers to the *in operando* measurements of Refs. [22] and [23].

mediates are shown in Fig. 7.14. For sake of completeness all other XES spectra are shown in Fig. 7.15. These results confirm the previous assignment of Peaks B and C. For Fe catalysts, a spectroscopic feature that is clearly shifted to lower energies by ca. 3 eV with respect to Peak B is only found for the low-spin state of **L**, **N** and **M**. Thus, the Peak A that was experimentally observed in Ref. [22] could indeed indicate that the SCR reaction proceeds via the "NO-first pathway" for Fe catalysts. However, this assignment only holds if the reaction proceeds via low-spin Fe(II) intermediates that are not the ground state in the calculations. On the other hand, it can clearly rule out that "Peak A" is due to the coordination of NO to the iron center, as was suggested in Ref. [197].

Of the intermediates considered for Cu catalysts, only intermediate **L** and **N** shows a peak clearly shifted to lower energies compared to Peak B in the calculated spectra. However, this species does not lie on a feasible reaction path that leads to the reduction of NO. Thus, the absence of such a peak in the *in operando* XES spectra reported in Ref. [23] does not allow to distinguish between the "NH_3-first" and "NO-first" (via **M** or **P**) reaction pathways.

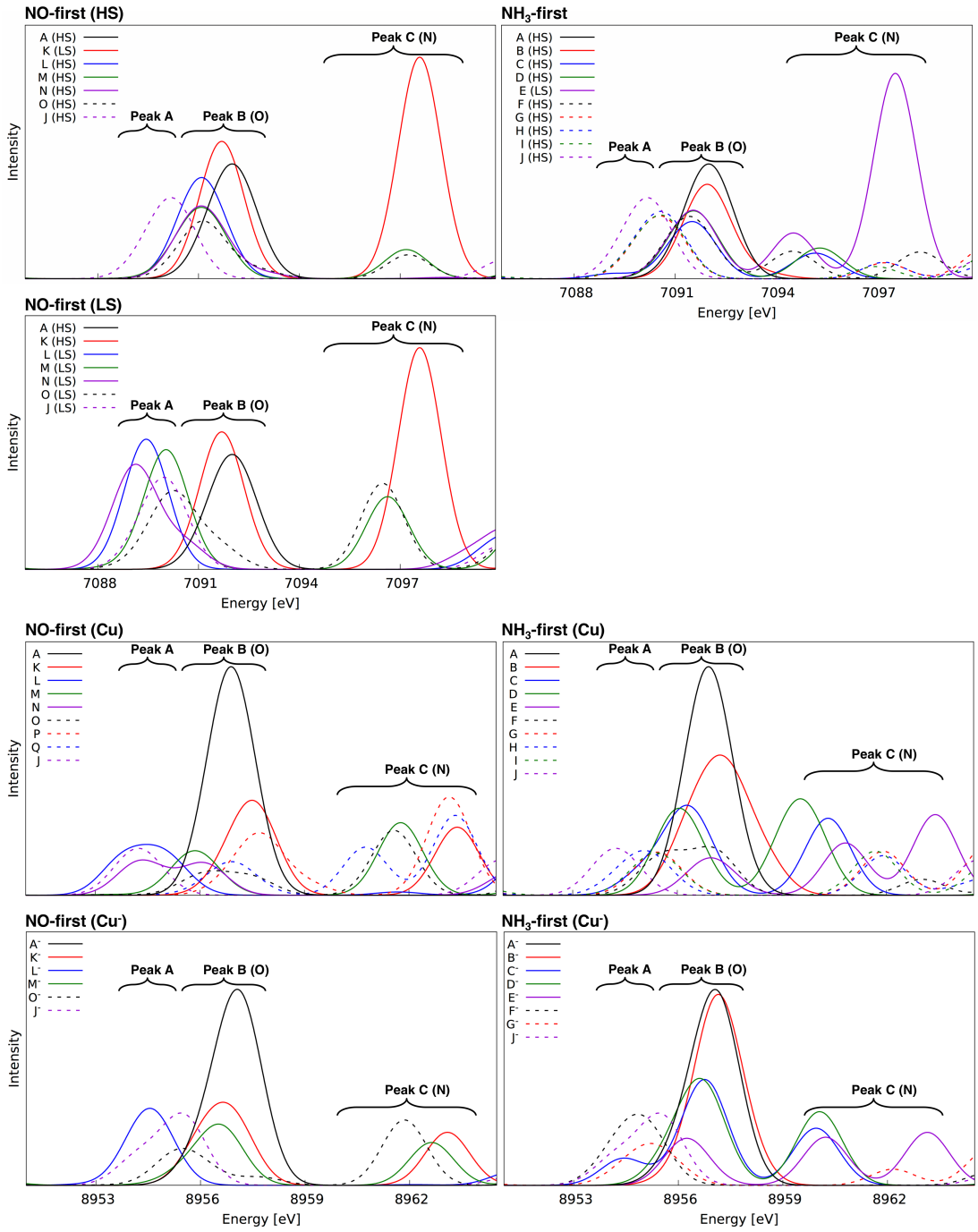

Figure 7.15: Calculated (BP86/QZ4P) Fe (**top**) and Cu (**bottom**) K-edge XES spectra of all intermediates on the considered catalytic reaction pathways of the SCR reaction [Cu catalysts (top: neutral active-site model, bottom: negatively-charged active-site model]).

7.5 Conclusions

In summary, several possible catalytic reaction pathways could be computationally identified for the reduction half-cycle of the selective catalytic reduction of NO_x with Fe- and Cu-exchanged zeolite catalysts. This provide a comprehensive picture that unifies several previous mechanistic proposals. It could be found that both for Fe and for Cu catalysts, different reaction pathways are available and both an "NH_3-first pathway" and an "NO-first pathway" seem feasible, of which the "NO-first pathway" is preferred according to the computational results. While on both pathways, a coordination of NO at the metal center and its direct reaction of NO with ligands coordinated at the metal center are both possible, NH_3 can only react further after its adsorption at the metal center. However, some of the available reaction pathways differ for Fe and Cu catalysts. While for Fe catalysts, the SCR reaction can proceed via an intermediate with a HONO ligand coordinated to the metal center via its central oxygen atoms, this pathway is not possible for Cu catalysts. This is in agreement with previous *in operando* XES measurements. On the other hand, for Cu catalysts a reaction path via an intermediate that simultaneously coordinates NO and NH_3 is available that is inaccessible for Fe catalysts.

A distinction between the different pathways that are feasible according to the present computational results will require further spectroscopic and computational studied. Computationally, larger models of the active site as well as the use of higher accuracy computational methods could decrease the computational error bars and possibly distinguish between different pathways. For Fe catalysts, quantum-chemical methods beyond density-functional theory might be required to provide more accurate spin-state energy differences. Moreover, the determination of the transition states connecting different intermediate as well as the calculation of the corresponding activation energies will be required for a complete picture. Of course, additional reaction pathways might become possible when considering larger active-site models, e.g., by involving a second metal center or by allowing for mobile, NH_3-solvated metal centers. Nevertheless, the unified mechanistic picture provided here will form an ideal starting point for such future studies.

Chapter 8

Summary

The stated goal of this thesis was to elucidate the reaction mechanism of the selective catalytic reduction over copper- and iron-exchanged zeolite catalysts based on computational thermodynamic and X-ray spectroscopic studies. For this purpose, theoretical X-ray absorption and emission spectroscopic methods have been selectively used in Chap. 5–6 to check the suitability for the investigation on the SCR reaction. Finally, in Chap. 7 thermodynamic calculations and theoretical X-ray emission spectroscopy were combined and the results were compared with experiment to propose a consistent mechanistic picture.

Calculations of K-edge X-ray absorption spectra on several copper complexes, which differed in the oxidation state of the copper center as well as in the local coordination environment, were presented in Chap. 5. These complexes were divided into four groups, Cu(I) complexes with a coordination number (CN) of 2, 3, 4, and Cu(II) complexes. By applying a systematic computational study combined with molecular orbital analysis on these complexes, the aim was to reproduce the experimental results and then explain the occurring peaks in detail. To investigate the dependence of the XAS spectra on the coordination number, the copper complexes were constructed, optimized, and XAS spectra were calculated.

For the linear copper complexes (CN=2), the highest-intensity pre-peaks were obtained (see filled symbols in Fig. 8.1a). The maximum peaks of the trigonal planar and T-shaped copper complexes (CN=3) were weakly shifted to lower energies and the intensity decreased by about half. The highest-intensity pre-peaks of the complexes with a CN=4 ligand environment lost intensity compared to the linear complexes and were shifted to higher energies. The main results obtained were qualitatively consistent with the experimental results, which are also shown in Fig. 8.1a as empty symbols. The same was true for all Cu(II) compounds, which are not shown in Fig. 8.1a. Overall, the calculated spectra provide a consistent picture of these general features.

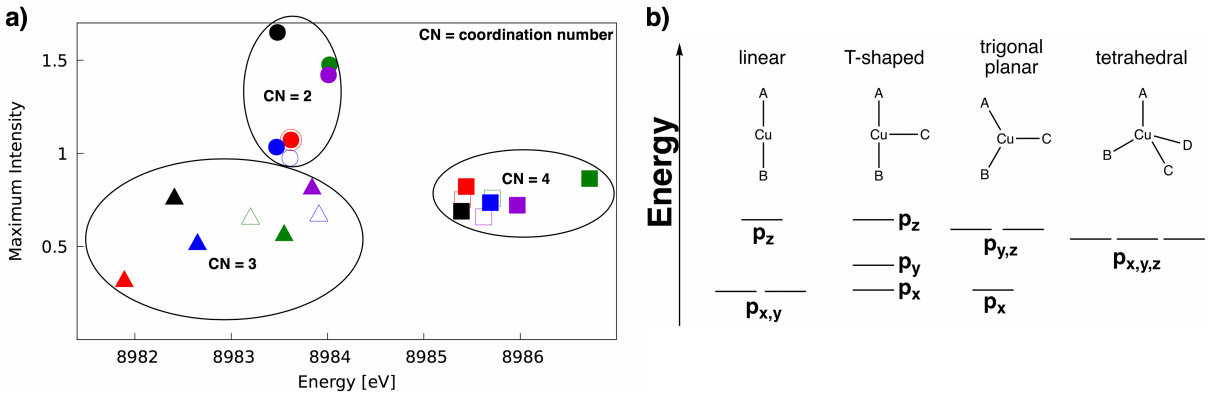

Figure 8.1: (a) Positions and maximum intensities (filled symbols) of the main pre-edge peaks for all Cu(I) complexes calculated with BP86/QZ4P. The experimental pre-edge maxima extracted from Fig. 2 of Ref. [126] are included as empty symbols where available. (b) Ligand field splitting of the unoccupied copper $4p$ orbitals in different coordination geometries.

In a second step, these interesting pre-edge features were analyzed by comparing a more accurate orbital analysis with a simple ligand field theory picture. It could be shown that the spectral dependence on the coordination number can be qualitatively explained by a simple ligand field picture (see Fig. 8.1b). The calculated spectra for CN=2 complexes were decomposed into the contributions of different types of unoccupied orbitals. Because the unoccupied Cu orbitals mixed with unoccupied ligand orbitals, the Cu $4p_x$ and Cu $4p_y$ orbitals were identified as responsible for the intense pre-edge peak. The second group, containing CN=3 complexes, showed pre-peaks at lower energies with decreased intensity compared to the linear group. This peaks were dominated only by the Cu $4p_x$ orbital. For all complexes with a CN=4, the highest-intensity peaks appeared at higher energies. The unoccupied Cu $4p_x$, $4p_y$, and $4p_z$ orbitals contributed equally to these most intense peaks, which also agreed with the ligand field picture 8.1b. Overall, all main features of the calculated Cu K-edge XAS spectra of the considered Cu(I) complexes could be explained by a simple ligand field picture.

Furthermore, additional features arising from interactions with unoccupied ligand orbitals were found and could be explained by schematic MO diagrams. For all Cu(II) complexes a typical weak pre-edge peak appeared, which could be assigned to transitions into the singly unoccupied Cu $3d$ orbital. In contrast, these Cu $3d$ orbitals were fully occupied in Cu(I) complexes and no peak could be observed. The comparison of this peak for the different Cu(II) complexes showed that its intensity varied, which could be directly related to the coordination geometry and the local symmetry at the Cu center. The remaining pre-edge transitions could, as for the Cu(I) complexes, be assigned to transitions into unoccupied Cu $4p$ orbitals. Altogether, the results presented in Chap. 5 will allow for the reliable analysis and assignment of experimental Cu K-edge XAS spectra. Therefore, they provide a valuable tool for the investigation of catalytic reaction mechanisms by revealing oxidation state and coordination environment of Cu (or in

general metal) centers.

Chap. 6 focused on valance-to-core X-ray emission spectroscopy. The structures of three different iron test molecules (see Fig. 8.2a) were systematically changed to investigate the effect of the structure on the VtC-XES spectrum. For the first example ironpentacarbonyl, the spectrum showed three interesting peaks (see Fig. 8.2b, **black** spectrum, peaks **1**, **2**, and **3**). To investigate the influence of directly coordinated ligands on the emission spectrum, four different bond lengths were changed. By increasing the axial Fe-CO bond distance, a decrease in intensity for the first peak could be seen, but the energetic position remained unaffected. The intensity and position of the maximum of the second peak were not affected by this displacement. The third peak underwent a minimal shift to higher energies without change in intensity. A Fe-CO bond length change on one of the three equatorial carbonyl ligands led to a decrease of the first peak, similar to the axial Fe-CO bond elongation. The second peak was shifted to higher energies and for the third peak, a strong decrease in intensity could be seen. The displacements of the C-O bond distances within the carbonyl ligands were almost independent of whether axial or equatorial carbonyls were considered. The first peak showed an increase in intensity, which was the opposite of the Fe-CO bond length enlargement. The maximum of the second peak was shifted to higher energies and the influence on the third peak was rather small, which was similar to the displacement of an axial Fe-CO bond length.

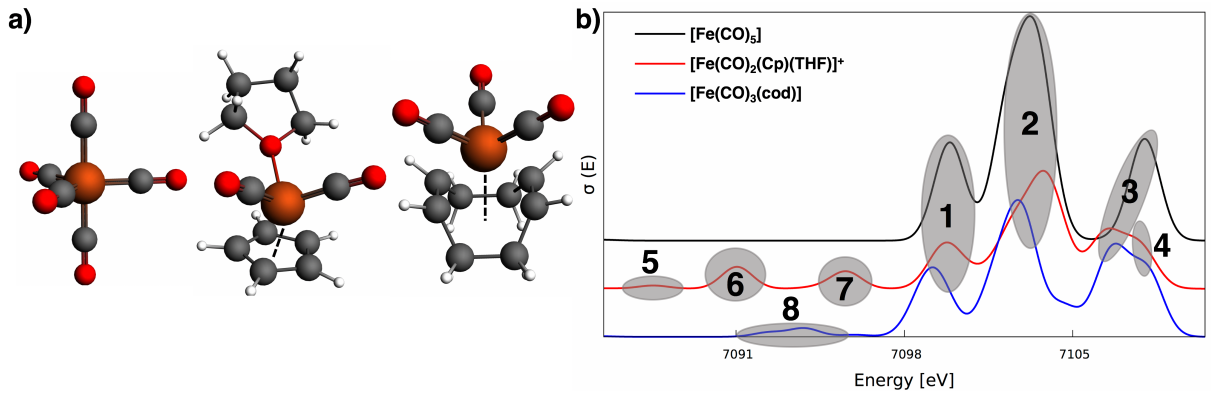

Figure 8.2: (a) Molecular structures of the three iron carbonyl model complexes: $[Fe(CO)_5]$, $[FeCp(CO)_2(THF)]^+$, $[Fe(CO)_3(cod)]$. (b) Calculated VtC-XES spectra of all three iron carbonyl complexes for the equilibrium structures with highlighted occurring peaks. These spectra were calculated with BP86/QZ4P.

Overall, changes in the axial and equatorial Fe-CO bond distance and in the C-O bond distances had a distinctly different effect on the VtC-XES spectra that could be revealed by this analysis. To some extent, these effects were in line with an analysis of the orbital contributions to the different peaks in literature. Peaks **1** and **2** are dominated by contributions arising from carbonyl orbitals, while peak **3** is mainly due to iron 3*d*-orbitals. Consequently, a change of the C-O bond

distance within the carbonyl ligand had little effect on the third peak. However, the analysis of the structural sensitivity applied in Chap. 6 was able to reveal which building blocks contribute to a certain peak. Furthermore, it was also possible to distinguish a different response (increase or decrease in intensity, change in peak position) of individual peaks to different structural changes within one ligand.

As a second example, the four-coordinate iron complex $[FeCp(CO)_2(THF)]^+$ was chosen (see Fig. 8.2a). Generally, the second part of the VtC spectrum (peaks **1**-**3** of $FeCO_5$) resembled the results of $FeCO_5$, with some small exceptions. Overall, four new signals could be obtained by adding the two new ligands, Cp and THF (see Fig. 8.2b, **red** spectrum, peaks **5**, **6**, **7** and shoulder **4**): a very weak peak at lower energy (**5**), two stronger peaks also at lower energies (**6** and **7**), and a good identifiable shoulder (**4**) at peak **3**. In addition to the three Fe-ligand bond lengths, the angle displacement of CO-Fe-CO was also considered. As expected, by changing the Fe-CO bond distance and the CO-Fe-CO bond angle, the new signals were almost unaffected. An elongation of the Fe-Cp bond length led to changes in both parts of the spectrum. The intensities of the peaks **6** and **7** as well as peaks **2** and **3** became less intense, and peak **1** was shifted to higher energies. By changing the Fe-THF bond length the most important observation was the decrease in intensity of the weak peak **5**.

This analysis of the structural sensitivity showed that the occurring features in VtC-XES spectra could be assigned to the individual ligands. More specifically, displacements of iron ligand bond lengths not always had an effect on the whole spectrum. Finally, the peaks at lower energies (**5**, **6**, and **7**) could be clearly assigned to the THF (**5**) and Cp ligand (**6** and **7**).

As a last example $[Fe(CO)_3(cod)]$ was chosen (see Fig. 8.2a), which had three carbonyl ligands and a η^4-coordinated cyclooctadienyl ligand attached to the central iron atom. In addition to the peaks of $FeCO_5$, the spectrum showed a broad weak peak at lower energies (see Fig. 8.2b, **blue** spectrum, peak **8**). Compared with the spectra of the previous two complexes, the spectrum showed a shift toward lower energies for the peaks **1** and **2**. The elongations of the Fe-CO bond, the C-O bond, and the CO-Fe-CO bond angle effected the spectrum in a similar pattern as for the other two complexes. As expected, by increasing the Fe-cod distance, the broad peak at lower energies (**8**) nearly disappeared. Finally, the spectrum changes, which were obtained by increasing the C-H bonds within the cod ligand, were very weak and could be neglected.

In summary, through Chap. 6 of the thesis, the occurrence of special features in VtC emission spectra could be explained in more detail. In contrast to the experiment, specific changes to molecular structures could be made to observe the direct influence on the spectrum. With this fairly simple approach, it was possible to show that a CO ligand provided a very similar peak pattern in different complexes. Based on the selected test cases, e.g. the peaks **1**-**3** could be assigned to the functional groups consisting of a iron atom and a carbonyl ligand. Further, the newly occurring features could be uniquely assigned to the inserted ligands (THF, Cp, cod).

In the last Chap. 7 of this thesis, investigations on the mechanism of the SCR reaction based on computational thermodynamic and X-ray spectroscopic studies were presented. In the first step, small iron and copper catalytic model systems were developed, which were tested to guarantee reliable results. With these model systems an overall picture of possible reaction paths was created by chemical intuition. Basically, the mechanism could proceed over two different pathways, the "NH3-first pathway" or the "NO-first pathway".

On the "NH3-first pathway", upon reaction with ammonia, after hydrogen rearrangement and subsequent dehydration, a metal species with a coordinated NH_2 ligand was formed (see Fig. 8.3). The following reaction with NO reduces the oxidation state of the metal center from +III to +II (**Fe**) or +II to +I (**Cu**). Afterwards the leaving group $NONH_2$ was formed, which could bind to the metal either via the nitrogen of the amino group or of the NO group. The energies of these two possible steps differed only minimally. In general, the "NH_3-first pathway" could be verified as an energy-wise possible reaction path for both iron- and copper-exchanged zeolite catalysts. Only the two species $[M(NH_2)(H_2O)]$ and $[M(NH_2)]$ were slightly higher in energy as the starting complex in the iron mechanism. In the case of copper, these two mentioned species were energetically more favorable.

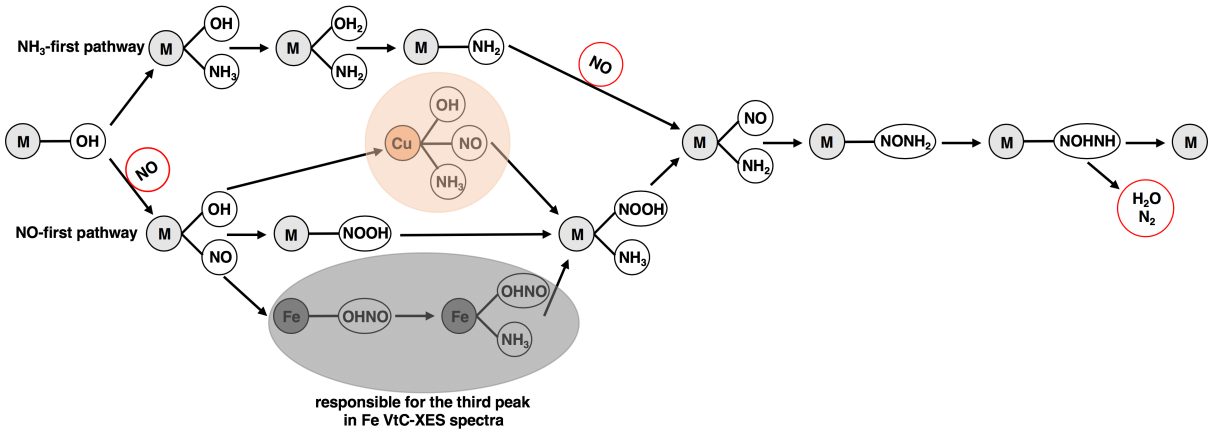

Figure 8.3: Schematic representation of the SCR mechanism over both copper- and iron-exchanged zeolite catalysts. Only the most thermodynamically favorable reaction pathways are shown. The two highlighted areas represent mechanistic steps, which were only computational accessible for copper or iron catalysts. The capital letter **M** stands for Cu or Fe. For the sake of clarity, the second hydroxyl group at the iron center, which has no impact on the reaction, is not shown.

For the second possible reaction pathway, the coordination of NO at the metal center proceeds first. From this point, three different mechanistic paths were available according to the DFT calculations, depending on the used metal. First, after ligand rearrangement, a metal complex (**iron** or **copper**) with a bound NOOH ligand could be obtained (see Fig. 8.3). This ligand was bound to the metal center via the nitrogen of NO. By the subsequent reaction with ammonia and

the release of a water ligand, the [M(NH_2)(NO)] species could be formed. A second reaction path was only accessible for the iron catalyst. Here, after ligand rearrangement a iron complex with a bound OHNO ligand (bound to the metal center via the hydroxyl oxygen) could be obtained (highlighted in Fig. 8.3). The reaction with ammonia and the subsequent release of water led also to complex [M(NH_2)(NO)]. According to the thermodynamic calculation, these two possible reaction pathways for iron differed only marginally in energy. The complexes containing the OHNO ligand were inaccessible or not existent for the copper catalyst, respectively, because the OHNO ligand was released from the metal center, and subsequent reactions were prevented. In contrast to iron, the copper mechanism could proceed via a third possible reaction path (highlighted in Fig. 8.3). After the reaction with nitrogen monoxide, the complex [Cu(OH)(NO)] could react directly with ammonia. This step was inaccessible for iron catalyst due to steric reasons. This described reaction path was, according to the calculations, the energetically most favorable reaction path for copper.

Overall, the consideration of the energies obtained clearly showed that the reaction pathway to the [M(NH_2)(NO)] complex is thermodynamically much more favorable over the "NO-first pathway" than over the "NH_3-first pathway" in both iron and copper cases.

In the next step VtC-XES spectra were calculated for all interesting complexes, which were determined by the thermodynamic calculations. As described in the introduction of the thesis and also in Chap. 7, spectroscopic measurements and calculations showed that the respective mechanisms must be different for iron and copper catalysts. For Fe catalysts, the SCR reaction could proceed via an intermediate with a OHNO ligand coordinated to the metal center via its central oxygen atom. This is in agreement with previous in operando XES measurements. The experimentally obtained peak at lower energy, could be assigned to the iron compounds [Fe(OHNO)] and [Fe(OHNO)(NH_3)], which are highlighted in Fig. 8.3. On the other hand, for Cu catalysts a reaction path via an intermediate that simultaneously coordinates NO and NH_3 was available. According to the VtC-XES calculations, for all copper intermediates during this pathway, no peak at lower energy could be obtained. Overall, several possible catalytic reaction pathways of the selective catalytic reduction of NO_x could be computationally identified. Furthermore, experimental obtained VtC-XES peaks could be assigned to individual complexes, which occurred in the developed reaction pathways. This provided a comprehensive picture that unifies several previous mechanistic proposals.

In summary, the results in Chap. 5 and 6 showed that the application of theoretical X-ray spectroscopy to transition metal complex provides important features beyond experimental accessible results. Furthermore, in Chap. 7 a consistent reaction mechanism for the SCR reaction over iron- and copper-exchanged zeolite catalysts could be developed based on a combination of thermodynamic and X-ray spectroscopic DFT calculations.

Chapter 9

Outlook

Throughout this thesis a solid basis has been developed to explore the SCR mechanism in more detail. For the first time, considering multiple possible reaction pathways together, a consistent reaction mechanism for both iron and copper SCR catalysts has been developed based on thermodynamic studies. The reaction pathways obtained here could be confirmed by comparing theoretical X-ray emission spectroscopy spectra with the experimental results in Chap. 7. It was possible to assign the occurring peaks to different complexes and therefore distinguish between different reaction pathways. Both thermodynamic and spectroscopic studies have shown that the results are not directly related to the size of the chosen model system, as small systems showed their ability to produce reliable results. Of course, considering larger model systems with more than one metal center in the zeolite framework, which is heavily discussed in literature,[22,23,48–59] could be interesting for the future. Also considering other metals, for example vanadium or manganese, for the non-stationary approach could give interesting insights into their reaction pathways.

To clearly distinguish between the different pathways that are feasible according to the presented computational results, further spectroscopic and computational studies are needed. Computationally larger models of the catalytic system as well as the use of higher accuracy computational methods could decrease the computational error bars. For Fe catalysts, quantum-chemical methods beyond DFT might be required to provide more accurate spin-state energy differences. Also kinetic investigations, more specifically transition state calculations, should follow soon to complete the overall picture.

From a spectroscopic point of view, in Chap. 7 it could be shown that the SCR mechanism is a suitable example to apply theoretical X-ray spectroscopic methods. The calculated XES spectra could explain the differences obtained in the experimental spectra during the SCR reaction over iron- and copper-exchanged zeolite catalysts. X-ray spectroscopic studies on the XES K$\beta_{2,5}$ region, which were not considered in Chap. 7, could be used to obtained more information from

the peaks that occur. The developed XES method, presented in Chap. 6, showed its reliability on assigning peaks to ligands in transition metal complexes. The use of this approach on all relevant SCR intermediates, obtained in Chap. 7, could be very helpful to identify occurring peaks and assign this peaks to different ligands, respectively. In Chap. 7 only Kβ" peaks, which depending on ligand electron lone-pairs, were considered and discussed. Here, the energy splitting between the obtained peaks also need further investigations to clearly assign these peaks to different intermediates during the SCR process.

Furthermore, K-edge XAS analysis, as presented in Chap. 5, for all relevant SCR intermediates could provide more information beyond the oxidation state of the metal. It is conceivable that such investigations could further explain the geometry around the metal center of SCR catalysts.

There are certainly more possible approaches from other points of view to continue working on the field of the SCR reaction. This research field will continue to provide a wide variety of possible approaches. Even if the mechanism is fully elucidated further studies will be needed to improve the catalytic behavior in a targeted way.

Bibliography

[1] Gao, F., Walter, E., Kollar, M., Wang, Y., Szanyi, J., and Peden, C. *J. Catal.* 319 (2014), pp. 1–14.

[2] Lomachenko, K. A., Borfecchia, E., Negri, C., Berlier, G., Lamberti, C., Beato, P., Falsig, H., and Bordiga, S. *J. Am. Chem. Soc.* 138 (2016), pp. 12025–12028.

[3] Xin, Y., Li, Q., and Zhang, Z. *ChemCatChem* 10 (2018), pp. 29–41.

[4] Taylor, K. *Catal. Rev.* 35 (1993), pp. 457–481.

[5] Gabrielsson, P. L. *Top. Catal.* 28 (2004), pp. 177–184.

[6] Brandenberger, S., Kröcher, O., Tissler, A., and Althoff, R. *Catal. Rev.* 50 (2008), pp. 492–531.

[7] Arnarson, L., Falsig, H., Rasmussen, S., Lauritsen, J., and Moses, P. *J. Catal.* 346 (2017), pp. 188–197.

[8] Held, W., König, A., Richter, T., and Puppe, L. *SAE Tech. Pap.* 900496 (1990).

[9] Long, R. Q. and Yang, R. T. *J. Catal.* 188 (1999), pp. 332–339.

[10] Long, R. Q. and Yang, R. T. *J. Am. Chem. Soc.* 121 (1999), pp. 5595–5596.

[11] Rahkamaa-Tolonen, K., Maunula, T., Lomma, M., Huuhtanen, M., and Keiski, R. L. *Catal. Today* 100 (2005), pp. 217–222.

[12] Bauer, M. and Bertagnolli, H. In: *Methods in Physical Chemistry*. Ed. by Schäfer, R. and Schmidt, P. C. Wiley-VCH Verlag GmbH & Co. KGaA, 2012, pp. 231–269.

[13] Walroth, R. C., Uebler, J. W. H., and Lancaster, K. M. *Chem. Commun.* 51 (2015), pp. 9864–9867.

[14] Bokhoven, J. A. van and Lamberti, C. In: *Nanotechnology in Catalysis*. Ed. by Voorde, M. V. d. and Sels, B. Wiley-VCH Verlag GmbH & Co. KGaA, 2017, pp. 1029–1054.

[15] Beckwith, M. A., Roemelt, M., Collomb, M.-N., DuBoc, C., Weng, T.-C., Bergmann, U., Glatzel, P., Neese, F., and DeBeer, S. *Inorg. Chem.* 50 (2011), pp. 8397–8409.

[16] Delgado-Jaime, M. U., DeBeer, S., and Bauer, M. *Chem. Eur. J.* 19 (2013), 15888–15897.

[17] MacMillan, S. N., Walroth, R. C., Perry, D. M., Morsing, T. J., and Lancaster, K. M. *Inorg. Chem.* 54 (2014), pp. 205–214.

[18] Pollock, C. J. and DeBeer, S. *Acc. Chem. Res.* 48 (2015), pp. 2967–2975.

[19] Lancaster, K. M., Roemelt, M., Ettenhuber, P., Hu, Y., Ribbe, M. W., Neese, F., Bergmann, U., and DeBeer, S. *Science* 334 (2011), pp. 974–977.

[20] Lancaster, K. M., Hu, Y., Bergmann, U., Ribbe, M. W., and DeBeer, S. *J. Am. Chem. Soc.* 135 (2013), pp. 610–612.

[21] Rees, J. A., Bjornsson, R., Schlesier, J., Sippel, D., Einsle, O., and DeBeer, S. *Angew. Chem.* 127 (2015), pp. 13447–13450.

[22] Boubnov, A., Carvalho, H. W. P., Doronkin, D. E., Günter, T., Gallo, E., Atkins, A. J., Jacob, Ch. R., and Grunwaldt, J.-D. *J. Am. Chem. Soc.* 136 (2014), pp. 13006–13015.

[23] Günter, T., Carvalho, H. W. P., Doronkin, D. E., Sheppard, T., Glatzel, P., Atkins, A. J., Rudolph, J., Jacob, Ch. R., Casapu, M., and Grunwaldt, J.-D. *Chem. Commun.* 51 (2015), pp. 9227–9230.

[24] Grassian, V. *Environmental catalysis*. New York: Taylor & Francis, 2005.

[25] Chorkendorff, I. and Niemantsverdriet, J. *Concepts of Modern Catalysis and Kinetics*. Weinheim: Wiley-VCH, 2003.

[26] Peace, H., Owen, B., and Raper, D. *Sci. Total Environ.* 334-335 (2004), pp. 347–357.

[27] Busca, G., Lietti, L., Ramis, G., and Berti, F. *Appl. Catal. B* 18 (1998), pp. 1–36.

[28] Devadas, M., Kröcher, O., Elsener, M., Wokaun, A., Söger, N., Pfeifer, M., Demel, Y., and Mussmann, L. *Appl. Catal. B* 67 (2006), pp. 187–196.

[29] Koebel, M., Elsener, M., and Kleemann, M. *Catal. Today* 59 (2000), pp. 335–345.

[30] Bosch, H. and Janssen, F. *Catal. Today* 2 (1988), pp. 369–379.

[31] Forzatti, P. and Lietti, L. *Heterogen. Chem. Rev.* 3 (1996), pp. 33–51.

[32] Haug, N. and Scharer, B. *Staub Reinhalt. d. Luft* 51 (1991), pp. 389–394.

[33] Heck, R., Farrauto, R., and Gulati, S. *Catalytic Air Pollution Control*. New York: Wiley Intersciences, 2002.

[34] Nova, I. and Tronconi, E. *Urea-SCR Technology for deNOx After Treatment of Diesel Exhausts*. New York: Springer-Verlag, 2014.

[35] Beale, A., Gao, F., Lezcano-Gonzalez, I., Peden, C., and Szanyi, J. *Chem. Soc. Rev.* 44 (2015), pp. 7371–7405.

[36] Rizzotto, V., Chen, P., and Simon, U. *Catalysts* 8 (2018).

[37] Koebel, M., Elsener, M., and Madia, G. *SAE Tech. Pap.* 2001-01-3625 (2001).

[38] Praveena, V. and Martin, M. *J. Energy Inst.* 91 (2018), pp. 704–720.

[39] Costa, C., Savva, P., Fierro, J., and Efstathiou, A. *Appl. Catal. B* 75 (2007), pp. 147–156.

[40] Traa, Y., Burger, B., and Weitkamp, J. *Microporous Mesoporous Mat.* 30 (1999), pp. 3–41.

[41] Topsøe, N.-Y. *Science* 265 (1994), pp. 1217–1219.

[42] Went, G., Leu, L.-j., and Bell, A. *J. Catal.* 134 (1992), pp. 479–491.

[43] Ramis, G., Busca, G., Bregani, F., and Forzatti, P. *Appl. Catal.* 64 (1990), pp. 259–278.

[44] Janssen, F., Van Den Kerkhof, F., Bosch, H., and Ross, J. *J. Phys. Chem.* 91 (1987), pp. 5921–5927.

[45] Inomata, M., Miyamoto, A., and Murakami, Y. *J. Catal.* 62 (1980), pp. 140–148.

[46] Takagi, M., Kawai, T., Soma, M., Onishi, T., and Tamaru, K. *J. Catal.* 50 (1977), pp. 441–446.

[47] Simon, U. and Franke, M. *Microporous Mesoporous Mat.* 41 (2000), pp. 1–36.

[48] Grossale, A., Nova, I., and Tronconi, E. *Catal. Today* 136 (2008), pp. 18–27.

[49] Schwidder, M., Kumar, M., Klementiev, K., Pohl, M., Brückner, A., and Grünert, W. *J. Catal.* 231 (2005), pp. 314–330.

[50] Gao, F., Kollár, M., Kukkadapu, R., Washton, N., Wang, Y., Szanyi, J., and Peden, C. *Appl. Catal. B* 164 (2015), pp. 407–419.

[51] Zhang, R., Anderst, E., Groden, K., and McEwen, J.-S. *Ind. Eng. Chem. Res.* 57 (2018), pp. 13396–13405.

[52] Zhang, R., Li, H., and McEwen, J.-S. *J. Phys. Chem. C* 121 (2017), pp. 25759–25767.

[53] Paolucci, C. et al. *J. Am. Chem. Soc.* 138 (2016), pp. 6028–6048.

[54] Paolucci, C., Verma, A. A., Bates, S. A., Kispersky, V. F., Miller, J. T., Gounder, R., Delgass, W. N., Ribeiro, F. H., and Schneider, W. F. *Angew. Chem. Int. Ed.* 53 (2014), pp. 11828–11833.

[55] Zhang, R., McEwen, J.-S., Kollár, M., Gao, F., Wang, Y., Szanyi, J., and Peden, C. H. *ACS Catal.* 4 (2014), pp. 4093–4105.

[56] Moreno-González, M., Hueso, B., Boronat, M., Blasco, T., and Corma, A. *J. Phys. Chem. Lett.* 6 (2015), pp. 1011–1017.

[57] Janssens, T. V. W. et al. *ACS Catal.* 5 (2015), pp. 2832–2845.

[58] Mao, Y., Wang, Z., Wang, H.-F., and Hu, P. *ACS Catal.* 6 (2016), pp. 7882–7891.

[59] Li, Y., Deng, J., Song, W., Liu, J., Zhao, Z., Gao, M., Wei, Y., and Zhao, L. *J. Phys. Chem. C.* 120 (2016), pp. 14669–14680.

[60] Ruggeri, M., Grossale, A., Nova, I., Tronconi, E., Jirglova, H., and Sobalik, Z. *Catal. Today* 184 (2012), pp. 107–114.

[61] Metkar, P., Salazar, N., Muncrief, R., Balakotaiah, V., and Harold, M. *Appl. Catal. B* 104 (2011), pp. 110–126.

[62] Paolucci, C. et al. *Science* 357 (2017), pp. 898–903.

[63] Grunenberg, J. *Computational spectroscopy: methods, experiments and applications*. Weinheim: Wiley-VCH, 2010.

[64] Jacob, Ch. R. and Reiher, M. *J. Chem. Phys.* 130 (2009), p. 084106.

[65] Jacob, Ch. R., Luber, S., and Reiher, M. *J. Phys. Chem. B* 113 (2009), pp. 6558–6573.

[66] Jacob, Ch. R., Luber, S., and Reiher, M. *Chem. Eur. J.* 15 (2009), pp. 13491–13508.

[67] Lancaster, K. M., Finkelstein, K. D., and DeBeer, S. *Inorg. Chem.* 50 (2011), pp. 6767–6774.

[68] Atkins, A. J., Jacob, Ch. R., and Bauer, M. *Chem. Eur. J.* 18 (2012), 7021–7025.

[69] Atkins, A. J., Bauer, M., and Jacob, Ch. R. *Phys. Chem. Chem. Phys.* 17 (2015), pp. 13937–13948.

[70] Penner-Hahn, J. E. *Coord. Chem. Rev.* 190-192 (1999), pp. 1101–1123.

[71] Bressler, C. and Chergui, M. *Chem. Rev.* 104 (2004), pp. 1781–1812.

[72] Kowalska, J. and DeBeer, S. *BBA - Molecular Cell Research* 1853 (2015), pp. 1406–1415.

[73] Laan, G. van der and Kirkman, I. W. *J. Phys. Condens. Matter* 4 (Apr. 1992), pp. 4189–4204.

[74] Enthaler, S., Junge, K., and Beller, M. *Angew. Chem. Int. Ed.* 47 (2008), pp. 3317–3321.

[75] Du, P. and Eisenberg, R. *Energ. Environ. Sci.* 5 (2012), pp. 6012–6021.

[76] Gao, F., Kwak, J. H., Szanyi, J., and Peden, C. H. F. *Top. Catal.* 56 (2013), pp. 1441–1459.

[77] Lezcano-Gonzalez, I., Deka, U., Arstad, B., Deyne, A. V. Y.-D., Hemelsoet, K., Waroquier, M., Speybroeck, V. V., Weckhuysen, B. M., and Beale, A. M. *Phys. Chem. Chem. Phys.* 16 (2013), pp. 1639–1650.

[78] Solomon, E. I., Szilagyi, R. K., DeBeer George, S., and Basumallick, L. *Chem. Rev.* 104 (2004), pp. 419–458.

[79] Bauer, M. and Gastl, C. *Phys. Chem. Chem. Phys.* 12 (2010), pp. 5575–5584.

[80] Eisenberger, P., Platzman, P. M., and Winick, H. *Phys. Rev. Lett.* 36 (1976), pp. 623–626.

[81] Heijboer, W. M., Glatzel, P., Sawant, K. R., Lobo, R. F., Bergmann, U., Barrea, R. A., Koningsberger, D. C., Weckhuysen, B. M., and Groot, F. M. F. de. *J. Phys. Chem. B* 108 (2004), pp. 10002–10011.

[82] Safonova, O. V., Tromp, M., Bokhoven, J. A. van, Groot, F. M. F. de, Evans, J., and Glatzel, P. *J. Phys. Chem. B* 110 (2006), pp. 16162–16164.

[83] Glatzel, P., Sikora, M., Smolentsev, G., and Fernández-García, M. *Catal. Today* 145 (2009), pp. 294–299.

[84] Bauer, M. *Phys. Chem. Chem. Phys.* 16 (2014), pp. 13827–13837.

[85] McEwen, J.-S., Anggara, T., Schneider, W. F., Kispersky, V. F., Miller, J. T., Delgass, W. N., and Ribeiro, F. H. *Catal. Today* 184 (2012), pp. 129–144.

[86] Giordanino, F., Borfecchia, E., Lomachenko, K. A., Lazzarini, A., Agostini, G., Gallo, E., Soldatov, A. V., Beato, P., Bordiga, S., and Lamberti, C. *J. Phys. Chem. Lett.* 5 (2014), pp. 1552–1559.

[87] Borfecchia, E., Lomachenko, K. A., Giordanino, F., Falsig, H., Beato, P., Soldatov, A. V., Bordiga, S., and Lamberti, C. *Chem. Sci.* 6 (2015), pp. 548–563.

[88] Günter, T., Doronkin, D. E., Boubnov, A., Carvalho, H. W. P., Casapu, M., and Grunwaldt, J.-D. *Top. Catal.* (2016), pp. 1–9.

[89] Glatzel, P. and Bergmann, U. *Coord. Chem. Rev.* 249 (2005), pp. 65–95.

[90] Pollock, C. J. and DeBeer, S. *J. Am. Chem. Soc.* 133 (2011), pp. 5594–5601.

[91] Atkins, A. J., Bauer, M., and Jacob, Ch. R. *Phys. Chem. Chem. Phys.* 15 (2013), pp. 8095–8105.

[92] Pollock, C. J., Lancaster, K. M., Finkelstein, K. D., and DeBeer, S. *Inorg. Chem.* 53 (2014), pp. 10378–10385.

[93] Parr, R. G. and Yang, W. *Density-Functional Theory of Atoms and Molecules*. Oxford: Oxford University Press, 1989.

[94] Koch, W. and Holthausen, M. C. *A Chemist's Guide to Density Functional Theory*. 2nd. Weinheim: Wiley-VCH, 2001.

[95] Orio, M., Pantazis, D. A., and Neese, F. *Photosynth Res.* 102 (2009), pp. 443–453.

[96] Hohenberg, P. and Kohn, W. *Phys. Rev.* 136 (1964), B864–B871.

[97] Kohn, W. and Sham, L. J. *Phys. Rev.* 140 (1965), A1133–A1138.

[98] Becke, A. D. *Phys. Rev. A* 38 (1988), pp. 3098–3100.

[99] Perdew, J. P. *Phys. Rev. B* 33 (1986), pp. 8822–8824.

[100] Stener, M., Fronzoni, G., and Simone, M. de. *Chem. Phys. Lett.* 373 (2003), pp. 115–123.

[101] Ray, K., DeBeer George, S., Solomon, E. I., Wieghardt, K., and Neese, F. *Chem. Eur. J.* 13 (2007), 2783–2797.

[102] DeBeer George, S., Petrenko, T., and Neese, F. *Inorg. Chim. Acta* 361 (2008), pp. 965–972.

[103] Banerjee, P., Sproules, S., Weyhermüller, T., DeBeer George, S., and Wieghardt, K. *Inorg. Chem.* 48 (2009), pp. 5829–5847.

[104] Chandrasekaran, P., Stieber, S. C. E., Collins, T. J., Lawrence Que, J., Neese, F., and DeBeer, S. *Dalton Trans.* 40 (2011), pp. 11070–11079.

[105] Scarborough, C. C., Sproules, S., Weyhermüller, T., DeBeer, S., and Wieghardt, K. *Inorg. Chem.* 50 (2011), pp. 12446–12462.

[106] Roemelt, M., Beckwith, M. A., Duboc, C., Collomb, M.-N., Neese, F., and DeBeer, S. *Inorg. Chem.* 51 (2012), pp. 680–687.

[107] Scarborough, C. C., Sproules, S., Doonan, C. J., Hagen, K. S., Weyhermüller, T., and Wieghardt, K. *Inorg. Chem.* 51 (2012), pp. 6969–6982.

[108] Lima, F. A., Bjornsson, R., Weyhermüller, T., Chandrasekaran, P., Glatzel, P., Neese, F., and DeBeer, S. *Phys. Chem. Chem. Phys.* 15 (2013), pp. 20911–20920.

[109] Römelt, C., Song, J., Tarrago, M., Rees, J. A., Gastel, M. van, Weyhermüller, T., DeBeer, S., Bill, E., Neese, F., and Ye, S. *Inorg. Chem.* 56 (2017), pp. 4745–4750.

[110] Castillo, R. G., Banerjee, R., Allpress, C. J., Rohde, G. T., Bill, E., Que, L., Lipscomb, J. D., and DeBeer, S. *J. Am. Chem. Soc.* 139 (2017), pp. 18024–18033.

[111] Casida, M. E. and Huix-Rotllant, M. *Annu. Rev. Phys. Chem.* 63 (2012), pp. 287–323.

[112] Runge, E. and Gross, E. K. U. *Phys. Rev. Lett.* 52 (1984), pp. 997–1000.

[113] Bernadotte, S., Atkins, A. J., and Jacob, Ch. R. *J. Chem. Phys.* 137 (2012), p. 204106.

[114] Klamt, A. and Schüürmann, G. *J. Chem. Soc., Perkin Trans.* 2 (1993), pp. 799–805.

[115] Lee, N., Petrenko, T., Bergmann, U., Neese, F., and DeBeer, S. *J. Am. Chem. Soc.* 132 (2010), pp. 9715–9727.

[116] Triguero, L., Pettersson, L. G. M., and Ågren, H. *Phys. Rev. B* 58 (1998), pp. 8097–8110.

[117] Nilsson, A. and Pettersson, L. G. M. *Surf. Sci. Rep.* 55 (2004), pp. 49–167.

[118] Smolentsev, G., Soldatov, A. V., Messinger, J., Merz, K., Weyhermüller, T., Bergmann, U., Pushkar, Y., Yano, J., Yachandra, V. K., and Glatzel, P. *J. Am. Chem. Soc.* 131 (2009), pp. 13161–13167.

[119] Kowalska, J. K., Hahn, A. W., Albers, A., Schiewer, C. E., Bjornsson, R., Lima, F. A., Meyer, F., and DeBeer, S. *Inorg. Chem.* 55 (2016), pp. 4485–4497.

[120] Kupper, C., Rees, J. A., Dechert, S., DeBeer, S., and Meyer, F. *J. Am. Chem. Soc.* 138 (2016), pp. 7888–7898.

[121] Wadey, J. D. and Besley, N. A. *J. Chem. Theory Comput.* 10 (2014), pp. 4557–4564.

[122] Roper, I. P. E. and Besley, N. A. *J. Chem. Phys.* 144 (2016), p. 114104.

[123] Rudolph, J. and Jacob, Ch. R. *Inorg. Chem.* 57 (2018), pp. 10591–10607.

[124] Solomon, E. I. and Hadt, R. G. *Coord. Chem. Rev.* 255 (2011), pp. 774–789.

[125] Lancaster, K. M., George, S. D., Yokoyama, K., Richards, J. H., and Gray, H. B. *Nat. Chem.* 1 (2009), pp. 711–715.

[126] Kau, L. S., Spira-Solomon, D. J., Penner-Hahn, J. E., Hodgson, K. O., and Solomon, E. I. *J. Am. Chem. Soc.* 109 (1987), pp. 6433–6442.

[127] Tomson, N. C., Williams, K. D., Dai, X., Sproules, S., DeBeer, S., Warren, T. H., and Wieghardt, K. *Chem. Sci.* 6 (2015), pp. 2474–2487.

[128] Vollmers, N. J., Müller, P., Hoffmann, A., Herres-Pawlis, S., Rohrmüller, M., Schmidt, W. G., Gerstmann, U., and Bauer, M. *Inorg. Chem.* 55 (2016), pp. 11694–11706.

[129] Deka, U., Juhin, A., Eilertsen, E. A., Emerich, H., Green, M. A., Korhonen, S. T., Weckhuysen, B. M., and Beale, A. M. *J. Phys. Chem. C* 116 (2012), pp. 4809–4818.

[130] Zhang, R. and McEwen, J.-S. *J. Phys. Chem. Lett.* (2018).

[131] Baker, M. L., Mara, M. W., Yan, J. J., Hodgson, K. O., Hedman, B., and Solomon, E. I. *Coord. Chem. Rev.* 345 (2017), pp. 182–208.

[132] Theoretical Chemistry, Vrije Universiteit Amsterdam. ADF, *Amsterdam density functional program.* URL: http://www.scm.com.

[133] Velde, G. te, Bickelhaupt, F. M., Baerends, E. J., Fonseca Guerra, C., Gisbergen, S. J. A. van, Snijders, J. G., and Ziegler, T. *J. Comput. Chem.* 22 (2001), pp. 931–967.

[134] Van Lenthe, E. and Baerends, E. J. *J. Comput. Chem.* 24 (2003), pp. 1142–1156.

[135] Becke, A. D. *J. Chem. Phys.* 98 (1993), pp. 5648–5652.

[136] Rehr, J. J. and Albers, R. C. *Rev. Mod. Phys.* 72 (2000), pp. 621–654.

[137] DeBeer George, S., Petrenko, T., and Neese, F. *J. Phys. Chem. A* 112 (2008), pp. 12936–12943.

[138] Epifanovsky, E., Polyakov, I., Grigorenko, B., Nemukhin, A., and Krylov, A. I. *J. Chem. Theory Comput.* 5 (2009), pp. 1895–1906.

[139] Leeuwen, R. van and Baerends, E. J. *Phys. Rev. A* 49 (1994), pp. 2421–2431.

[140] Sorrell, T. N. and Jameson, D. L. *J. Am. Chem. Soc.* 105 (1983), pp. 6013–6018.

[141] Lewin, A. H., Michl, R. J., Ganis, P., and Lepore, U. *J. Chem. Soc., Chem. Commun.* 0 (1972), pp. 661–662.

[142] O'Connor, B. H. and Maslen, E. N. *Acta Cryst.* 20 (1966), pp. 824–835.

[143] Besley, N. A. and Asmuruf, F. A. *Phys. Chem. Chem. Phys.* 12 (2010), pp. 12024–12039.

[144] Capano, G. et al. *Chem. Phys. Lett.* 580 (2013), pp. 179–184.

[145] Sano, M., Komorita, S., and Yamatera, H. *Inorg. Chem.* 31 (1992), pp. 459–463.

[146] Roemelt, M., Maganas, D., DeBeer, S., and Neese, F. *J. Chem. Phys.* 138 (2013), p. 204101.

[147] Pinjari, R. V., Delcey, M. G., Guo, M., Odelius, M., and Lundberg, M. *J. Chem. Phys.* 141 (2014), p. 124116.

[148] Oung, S. W., Rudolph, J., and Jacob, Ch. R. *Int. J. Quantum Chem.* 118 (2018), e25458.

[149] Karwowski, J. *Int. J. Quantum Chem.* 109 (2009), 2456–2463.

[150] Lilienfeld, O. A. von. *Int. J. Quantum Chem.* 113 (2013), pp. 1676–1689.

[151] Weymuth, T. and Reiher, M. *Int. J. Quantum Chem.* 114 (2014), pp. 823–837.

[152] Smith, R. *Uncertainty Quantification: Theory, Implementation, and Applications*. Philadelphia: SIAM, 2014.

[153] Wellendorff, J., Lundgaard, K. T., Møgelhøj, A., Petzold, V., Landis, D. D., Nørskov, J. K., Bligaard, T., and Jacobsen, K. W. *Phys. Rev. B* 85 (2012), p. 235149.

[154] Medford, A. J., Wellendorff, J., Vojvodic, A., Studt, F., Abild-Pedersen, F., Jacobsen, K. W., Bligaard, T., and Nørskov, J. K. *Science* 345 (2014), pp. 197–200.

[155] Wellendorff, J., Lundgaard, K. T., Jacobsen, K. W., and Bligaard, T. *J. Chem. Phys.* 140 (2014), p. 144107.

[156] Simm, G. N. and Reiher, M. *J. Chem. Theory Comput.* 12 (2016), pp. 2762–2773.

[157] Beckwith, M. A. et al. *J. Am. Chem. Soc.* 137 (2015), pp. 12815–12834.

[158] Chernev, P., Zaharieva, I., Rossini, E., Galstyan, A., Dau, H., and Knapp, E.-W. *J. Phys. Chem. B* 120 (2016), pp. 10899–10922.

[159] Askerka, M., Brudvig, G. W., and Batista, V. S. *Acc. Chem. Res.* 50 (2017), pp. 41–48.

[160] Li, X., Sproviero, E. M., Ryde, U., Batista, V. S., and Chen, G. *Int. J. Quantum Chem.* 113 (2013), pp. 474–478.

[161] Luber, S., Rivalta, I., Umena, Y., Kawakami, K., Shen, J.-R., Kamiya, N., Brudvig, G. W., and Batista, V. S. *Biochemistry* 50 (2011), pp. 6308–6311.

[162] Sumowski, C. V., Hanni, M., Schweizer, S., and Ochsenfeld, C. *J. Chem. Theory Comput.* 10 (2014), pp. 122–133.

[163] Jansen, T. l. C., Dijkstra, A. G., Watson, T. M., Hirst, J. D., and Knoester, J. *J. Chem. Phys.* 125 (2006), p. 044312.

[164] Weymuth, T., Jacob, Ch. R., and Reiher, M. *J. Phys. Chem. B* 114 (2010), pp. 10649–10660.

[165] Richter, B., Kuhlenbeck, H., Freund, H.-J., and Bagus, P. S. *Phys. Rev. Lett.* 93 (2004), p. 026805.

[166] Bagus, P. S., Wieckowski, A., and Freund, H. *Comput. Theor. Chem.* 987 (2012), pp. 22–24.

[167] Ruud, K., Åstrand, P.-O., and Taylor, P. R. *J. Chem. Phys.* 112 (2000), pp. 2668–2683.

[168] Rugen, T. A. and Ruud, K. In: *Calculation of NMR and EPR Parameters. Theory and Applications*. Ed. by Kaupp, M., Bühl, M., and Malkin, V. G. Weinheim: Wiley-VCH, 2004, pp. 85–100.

[169] Chen, X., Rinkevicius, Z., Cao, Z., Ruud, K., and Ågren, H. 13 (2010), pp. 696–707.

[170] Chen, X., Rinkevicius, Z., Ruud, K., and Ågren, H. *J. Chem. Phys.* 138 (2013), p. 054310.

[171] Ringholm, M., Jonsson, D., and Ruud, K. *J. Comput. Chem.* 35 (2014), pp. 622–633.

[172] Delgado-Jaime, M. U. and DeBeer, S. *J. Comput. Chem.* 33 (2012), pp. 2180–2185.

[173] Rudolph, J. and Jacob, Ch. R. *ACS Omega* 4 (2019), pp. 7987–7993.

[174] Busca, G., Lietti, L., Ramis, G., and Berti, F. *Appl. Catal. B* 18 (1998), pp. 1–36.

[175] Koebel, M., Elsener, M., and Kleemann, M. *Catal. Today* 59 (2000), pp. 335–345.

[176] Brandenberger, S., Kröcher, O., Tissler, A., and Althoff, R. *Catal. Rev.* 50 (2008), pp. 492–531.

[177] Guan, B., Zhan, R., Lin, H., and Huang, Z. *Appl. Therm. Eng.* 66 (2014), pp. 395–414.

[178] Beale, A. M., Gao, F., Lezcano-Gonzalez, I., Peden, C. H. F., and Szanyi, J. *Chem. Soc. Rev.* 44 (2015), pp. 7371–7405.

[179] Xin, Y., Li, Q., and Zhang, Z. *ChemCatChem* 10 (2018), pp. 29–41.

[180] Schwidder, M., Kumar, M. S., Klementiev, K., Pohl, M. M., Brückner, A., and Grünert, W. *J. Catal.* 231 (2005), pp. 314–330.

[181] Grossale, A., Nova, I., and Tronconi, E. *Catal. Today* 136 (2008), pp. 18–27.

[182] Schmieg, S. J., Oh, S. H., Kim, C. H., Brown, D. B., Lee, J. H., Peden, C. H. F., and Kim, D. H. *Catal. Today* 184 (2012), pp. 252–261.

[183] Blakeman, P. G., Burkholder, E. M., Chen, H.-Y., Collier, J. E., Fedeyko, J. M., Jobson, H., and Rajaram, R. R. *Catal. Today* 231 (2014), pp. 56–63.

[184] Gao, F., Kollár, M., Kukkadapu, R. K., Washton, N. M., Wang, Y., Szanyi, J., and Peden, C. H. F. *Appl. Catal. B* 164 (2015), pp. 407–419.

[185] Gao, F., Walter, E. D., Karp, E. M., Luo, J., Tonkyn, R. G., Kwak, J. H., Szanyi, J., and Peden, C. H. F. *J. Catal.* 300 (2013), pp. 20–29.

[186] Bates, S., Verma, A., Parekh, A., Anggara, T., Yezerets, A., Schneider, W., Miller, J., Delgass, W., and Ribeiro, F. *J. Catal.* 312 (2014), pp. 87–97.

[187] Moreno-González, M., Hueso, B., Boronat, M., Blasco, T., and Corma, A. *J. Phys. Chem. Lett.* (2015), pp. 1011–1017.

[188] Li, Y., Deng, J., Song, W., Liu, J., Zhao, Z., Gao, M., Wei, Y., and Zhao, L. *J. Phys. Chem. C* 120 (2016), pp. 14669–14680.

[189] Gao, F., Zheng, Y., Kukkadapu, R. K., Wang, Y., Walter, E. D., Schwenzer, B., Szanyi, J., and Peden, C. H. F. *ACS Catal.* 6 (2016), pp. 2939–2954.

[190] Zhang, R., Anderst, E., Groden, K., and McEwen, J.-S. *Ind. Eng. Chem. Res.* 57 (2018), pp. 13396–13405.

[191] Zhang, R., McEwen, J.-S., Kollár, M., Gao, F., Wang, Y., Szanyi, J., and Peden, C. H. F. *ACS Catal.* 4 (2014), pp. 4093–4105.

[192] Zhang, R., Li, H., and McEwen, J.-S. *J. Phys. Chem. C* (2017).

[193] Kerkeni, B., Berthout, D., Berthomieu, D., Doronkin, D. E., Casapu, M., Grunwaldt, J.-D., and Chizallet, C. *J. Phys. Chem. C* 122 (2018), pp. 16741–16755.

[194] Chen, P., Khetan, A., Jabłońska, M., Simböck, J., Muhler, M., Palkovits, R., Pitsch, H., and Simon, U. *Appl. Catal. B* 237 (2018), pp. 263–272.

[195] Mao, Y., Wang, H.-F., and Hu, P. *Int. J. Quantum Chem.* 115 (2015), pp. 618–630.

[196] Paolucci, C., Di Iorio, J. R., Ribeiro, F. H., Gounder, R., and Schneider, W. F. In: *Advances in Catalysis*. Ed. by Song, C. Vol. 59. Academic Press, 2016, pp. 1–107.

[197] Jiang, T. and Lobo, R. F. In: *Structure and Reactivity of Metals in Zeolite Materials*. Ed. by Pérez Pariente, J. and Sánchez-Sánchez, M. SpringerLink, 2018, pp. 155–178.

[198] Janssens, T. V. W. et al. *ACS Catal.* 5 (2015), pp. 2832–2845.

[199] Mao, Y., Wang, Z., Wang, H.-F., and Hu, P. *ACS Catal.* 6 (2016), pp. 7882–7891.

[200] Brüggemann, T. C. and Keil, F. J. *J. Phys. Chem. C* 115 (2011), pp. 23854–23870.

[201] Gao, F., Mei, D., Wang, Y., Szanyi, J., and Peden, C. H. F. *J. Am. Chem. Soc.* 139 (2017), pp. 4935–4942.

[202] Metkar, P. S., Salazar, N., Muncrief, R., Balakotaiah, V., and Harold, M. P. *Appl. Catal. B* 104 (2011), pp. 110–126.

[203] Li, J. and Li, S. *J. Phys. Chem. C* 112 (2008), pp. 16938–16944.

[204] Grimme, S., Antony, J., Ehrlich, S., and Krieg, H. *J. Chem. Phys.* 132 (2010), p. 154104.

[205] Reiher, M., Salomon, O., and Hess, B. A. *Theor. Chem. Acc.* 107 (2001), pp. 48–55.

[206] Jacob, Ch. R. and Reiher, M. *Int. J. Quantum Chem.* 112 (2012), pp. 3661–3684.

[207] Swart, M. *Int. J. Quantum Chem.* 113 (2013), 2–7.

[208] Lomachenko, K. A., Borfecchia, E., Bordiga, S., Soldatov, A. V., Beato, P., and Lamberti, C. *J. Phys.: Conf. Ser.* 712 (2016), p. 012041.

Acknowledgments

In diesem letzten Teil meiner Arbeit möchte ich denjenigen danken, die mich schon vor und natürlich während dieses Abschnitts meines Lebens unterstützt haben.

Als erstes möchte ich meinen Eltern und meiner Schwester danken. Ihr wart zu jedem Zeitpunkt für mich da, ob mit persönlichem Rat oder finanzieller Ünterstützung, auf euch war immer Verlass. Auch wenn ich euch das Leben mit Sicherheit nicht immer einfach gemacht habe, ihr mir allerdings auch nicht ;-), Danke für Alles. Ohne Euch, hätte ich diesen Punkt sehr wahrscheinlich nicht erreichen können.

Ein ganz spezieller Dank richtet sich an meine wundervolle Frau Sonja. Nur durch deine Unterstützung konnte ich diesen Abschnitt meines Lebens erfolgreich abschließen. Du hast mich immer wieder motiviert und angetrieben, gerade in schwierigen Phasen warst du mein Rückhalt. Unser wundervolles Leben zusammen hat mir immer die nötigen Erholungspausen ermöglicht, um Energie zu tanken für anstehende Aufgaben.

Für den fachlichen Bereich, möchte ich in erster Linie meinem Mentor Christoph danken. Auch wenn wir uns vorher gar nicht kannten, hast du mir die Möglichkeit gegeben bei dir meine Promotion zu absolvieren. Für diese Chance bin ich dir sehr dankbar. Ich habe in dieser Zeit sehr viel von dir gelernt und du hast mich in meiner wissenschaftlichen Entwicklung immer gefördert. In besonderer Erinnerung wird mir immer die gewährte wissenschaftliche und auch private Freiheit bleiben, Vielen Dank, ich habe die Zeit sehr genossen.

Des Weiteren bin ich Jomo und Prof. Dr. Tamm sehr dankbar, die sich sofort bereit erklärt hatten meine Arbeit zu begutachten bzw. den Vorsitz der Promotionskommission zu übernehmen. Und Jomo denke bitte bei der Bewertung meiner Arbeit immer daran, nur durch meine überzeugende Leistung darfst du dich 4. NFF-Fußball-Cup Sieger nennen ;-).

Zum Abschluss möchte ich mich auch bei meinen Kollegen Mario, Simone, Andrew, Eule, Kostas, Micha, Anika, Felix, Wadtey, Don und Pieper für die super Atmosphäre auf der Arbeit bedanken. Besonderer Dank gilt hier Dr. Mario, ja das Dr. ist ganz wichtig ;-). Du musstest mich als längstes aushalten, aber ich glaub so schlimm war es gar nicht. Ich werde die fachlichen wie auch privaten, meist sehr interessanten Gespräche und Diskussionen mit Sicherheit sehr vermissen, du bist mir persönlich sehr ans Herz gewachsen. Des Weiteren hat deine meist konstruktive Kritik beim Korrekturlesen meiner Arbeit diese durchaus verbessert. Auch meinem Vorgänger Andrew möchte ich danken, der extra zweimal nach Braunschweig gekommen ist um mir die Grundlagen der theoretischen Röntgenspektroskopie zu erklären. Bei Eule und mir hingegen rückte der fachliche Aspekt manchmal (oft?) in den Hintergrund, aber man muss ja auch mal Spaß haben dürfen, und den hatten wir definitiv. Don und Pieper bin ich sehr dankbar für die Unterstützung bei Layout und dem nervigen Papierkram.

Vollständige Publikationsliste

- Günter, T., Carvalho, H. W. P., Doronkin, D. E., Sheppard, T., Glatzel, P., Atkins, A. J., **Rudolph, J.**, Jacob, Ch. R., Casapu, M., and Grunwaldt, J.-D., "Structural snapshots of the SCR reaction mechanism on Cu-SSZ-13", *Chem. Commun. 51*, pp. 9227-9230 (2015).
- Oung, S. W., **Rudolph, J.**, and Jacob, Ch. R., "Uncertainty quantification in theoretical spectroscopy: The structural sensitivity of X-ray emission spectra", *Int. J. Quantum Chem. 118*, e25458 (2018).
- **Rudolph, J.**, and Jacob, Ch. R., "Revisiting the Dependence of Cu K-Edge X-ray Absorption Spectra on Oxidation State and Coordination Environment", *Inorg. Chem. 57*, pp. 10591-10607 (2018).
- **Rudolph, J.**, and Jacob, Ch. R., "Computational insights into the mechanism of the selective catalytic reduction of NO_x: Fe- versus Cu-exchanged zeolite catalysts", *ACS Omega 4*, pp. 7987-7993 (2019).
- Burkhardt, L., **Rudolph, J.**, Carlsson, P.-A., Jacob, Ch. R. and Bauer, M., "Probing Structural Nitrosyl Isomers by High-Resolution Hard X-ray Spectroscopy: A Combined Experimental and Theoretical Study of the Hieber Anion", submitted (2019).